学位論文

Mathematical aspects of spin-momentum locking: generalization to magnonic systems and application of orbifold to topological material science

（スピン運動量ロッキングの数理：
マグノン系への一般化及び
オービフォールドのトポロジカル物質科学への応用 ）

平成29年12月　博士（理学）申請

東京大学大学院理学系研究科
物理学専攻

大熊 信之
Okuma, Nobuyuki

Abstract

The spin-momentum locking, in which electron spin depends on its momentum, has attracted much interest in recent condensed matter physics. In momentum space, this phenomenon is expressed as an interesting spin vector field. In particular, singular spin textures in momentum space have been extensively investigated in electron systems without spin rotational symmetry. In two dimensions, a spin vortex with the winding number $+1$ has been found in momentum space of the Rashba electron gas system and topological insulator surface state. In the presence of this spin structure, electric current induces spin polarization. This magnetoelectric effect is the so-called Rashba-Edelstein effect, and its efficient spin-charge conversion nature is useful in spintronics. In three dimensions, a spin monopole with the winding number ± 1 has been discussed in the context of the topological semimetals. In realistic materials, a spin texture in momentum space is closely related to the band topology. In this sense, the spin-momentum locking plays an important role not only in spintronics but also in topological material science.

Although the spin vortices and monopoles in momentum space have been extensively investigated, previous studies have focused on structures with the winding number ± 1. It is important to investigate various types of singular spin textures since they are expected to lead to new transport phenomena. Also in principle, the notion of the spin-momentum locking can be generalized to other quasiparticles that carry spin angular momentum. These two directions are main topics of this thesis.

In this thesis, we first introduce the basics of the spin-momentum locking and review two papers [1, 2] in Introduction. Then we move on to the following two topics. (1) Generalization of spin-momentum locking to magnonic systems. (2) Classification of the electron spin texture in three-dimensional momentum space under the space group symmetries by using the notion of the orbifold. The topic (1) is based on the paper [3].

In the topic (1), we present a theory of the magnon spin-momentum locking in the semiclassical regime. We define the magnon spin and give the conditions

for it to be independent of momentum. Avoiding such no-go conditions, we construct several examples of the magnon spin-momentum locking. We find that the magnon spin depends on its momentum even when the Hamiltonian has the z-axis spin rotational symmetry, which can be explained in the context of a singular band point or a symmetry breaking. We find a high-winding number spin vortex (winding number: -2) in momentum space, which has not been found in electron systems. We also find that topology of momentum space imposes constraints on the spin configurations by using the Poincaré-Hopf index theorem. This fact is the starting point of the topic (2).

In the topic (2), we investigate electron spin textures in momentum space in the presence of three-dimensional space group symmetries. Since space group symmetries affect both momentum and spin, both the symmetries and topology of momentum space impose constraints on the spin texture. To describe this situation, we introduce the notion of the orbifold, which is a simple generalization of the manifold. We define the momentum space orbifold for space group symmetries, and map the spin texture on momentum space to the (pseudo-)vector field on the momentum space orbifold. We explicitly derive the constraints on spin textures for 24 symmorphic space groups by investigating the topology of 24 momentum space orbifolds. The derived constraints are useful to find Weyl points and new spin monopoles in momentum space.

Contents

Chapter 1

Introduction

In this chapter, we introduce the notion of the spin-momentum locking, which attracts a lot of interests in recent condensed matter physics such as spintronics and topological physics. Since we generalize this notion in this thesis, we here give a flexible definition of the spin-momentum locking. To emphasize the importance of the spin-momentum locking, we describe details of the conventional spin-momentum locking in which there is a spin-vortex with the winding number +1. In particular, we discuss the various spin transport phenomena that occur in topological insulator surface states. At the end of the chapter, we explain the motivations and outline of this thesis. In the following, we set $\hbar = k_B = 1$.

1.1 Spin texture in momentum space

The spin-orbit interaction has played important roles in recent condensed matter physics. It combines the electron spin and its motion, and affects electron's transport phenomena. For instance, the spin-orbit interaction behaves as a kind of a spin-dependent magnetic field, and it leads to the celebrated intrinsic spin Hall effect [4]. After this discovery, theorists found that band inversions in the presence of the spin-orbit interaction play key roles in the emergence of the topological phases such as topological insulators [5, 6, 7]. Other recent topological concepts such as Weyl semimetals [8, 9, 10, 11] are also realized in materials with strong spin-orbit coupling.

In recent spintronics, the spin-momentum locking [5, 6, 12] induced by the spin-orbit coupling has been extensively investigated. In this phenomenon, the electron spin direction depends on the electron momentum. In momentum space, this can be expressed as the spin texture with singular structures such as vortices in two dimensions and monopoles in three dimensions. The presence of such

singular spin structures is a source of magnetoelectric effects discussed later.

In the following, we first define the spin-momentum locking. Then we show some typical examples of the materials in which the spin-momentum locking occurs.

1.1.1 Definition: spin-momentum locking

We first introduce the electron spin expectation value. Suppose that the electron system is well described by the one-particle band theory. The electron spin expectation value for (the periodic part of) the Bloch wave function $|\boldsymbol{k}, a\rangle$ is defined as

$$\boldsymbol{S}_{\boldsymbol{k},a} = \langle \boldsymbol{k}, a|\hat{\boldsymbol{S}}|\boldsymbol{k}, a\rangle, \tag{1.1}$$

where $\boldsymbol{k}$ is the crystal momentum, a is the band index, and $\hat{\boldsymbol{S}} = \hat{\boldsymbol{\sigma}}/2 \otimes \hat{1}$ with $\hat{\sigma}_i$ being the Pauli matrices in spin space and $\hat{1}$ being the identity matrix in orbit space. We here assume that there is no spin degeneracy for $|\boldsymbol{k}, a\rangle$ due to the spin-orbit or magnetic interactions. Although the termnology "spin-momentum locking" is conventionally used for the electron spin locked at a right angle to the momentum, we here give an extended definition of the spin-momentum locking as follows.

Spin-momenutm locking

If $\boldsymbol{S}_{\boldsymbol{k},a}$ is not a constant function of $\boldsymbol{k}$, the band a is spin-momentum locked. When we regard $\boldsymbol{S}_{\boldsymbol{k},a}$ as a vector field on momentum space, the conventional spin-momentum locking is described as a spin vortex with winding number $+1$ in this vector field.

1.1.2 Two-dimensional examples of spin-momentum locking

The earliest example of the spin-momentum locking is realized in a two-dimensional electron gas system with the Rashba-type spin-orbit interaction [12]. To understand the physics of the spin-momentum locking, it is convenient to consider the general two-band model with spin degrees of freedom:

$$\mathcal{H}_{\boldsymbol{k}} = E^{(0)}_{\boldsymbol{k}}\hat{1} + \boldsymbol{B}_{\boldsymbol{k}} \cdot \hat{\boldsymbol{\sigma}}, \tag{1.2}$$

where $\mathcal{H}_{\boldsymbol{k}}$ is the Bloch Hamiltonian, $\hat{1}$ and $\hat{\sigma}_i$ are the identity and Pauli matrices in spin space, $E^{(0)}_{\boldsymbol{k}}$ is the spin-independent dispersion, and $\boldsymbol{B}_{\boldsymbol{k}}$ characterizes the

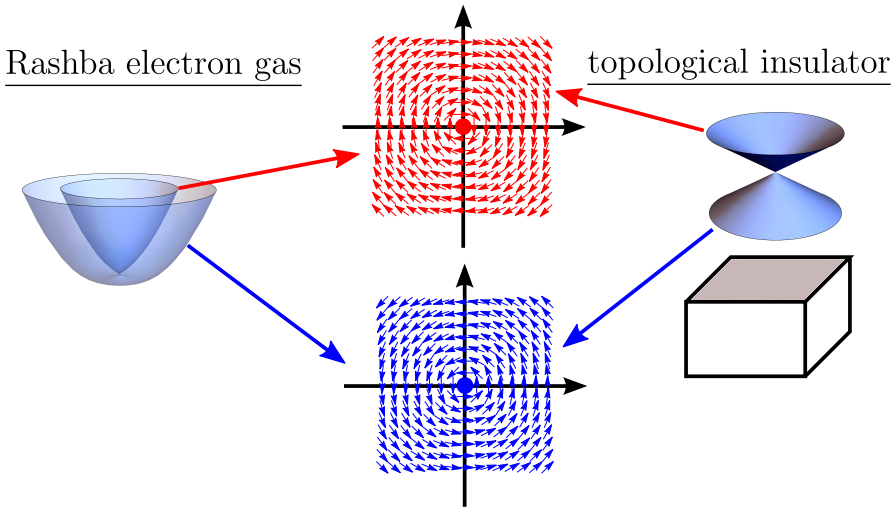

Figure 1.1: Schematic picture of spin-momentum locking in two-dimensional systems. There is a spin vortex with winding number +1 for each band.

spin-orbit and magnetic interactions. $\boldsymbol{k}$ is defined as two- and three-dimensional momentum in two- and three-dimensional systems, respectively. Let $|\boldsymbol{k}, \pm\rangle$ be two eigenstates with two eigenenergies

$$\xi_{\boldsymbol{k}}^{\pm} = E_{\boldsymbol{k}}^{(0)} \pm |\boldsymbol{B}_{\boldsymbol{k}}| \tag{1.3}$$

of the Hamiltonian (1.2). For convenience, we define the projection operator for the eigenstates:

$$\hat{P}_{\boldsymbol{k},\pm} = |\boldsymbol{k}, \pm\rangle\langle\boldsymbol{k}, \pm| = \frac{\hat{1} \pm \boldsymbol{d}_{\boldsymbol{k}} \cdot \hat{\boldsymbol{\sigma}}}{2}, \tag{1.4}$$

where $\boldsymbol{d}_{\boldsymbol{k}} \equiv \boldsymbol{B}_{\boldsymbol{k}}/|\boldsymbol{B}_{\boldsymbol{k}}|$ is the d-vector. Using this projection operator, the electron spin expectation value can be easily calculated as

$$\boldsymbol{S}_{\boldsymbol{k},\pm} = \mathrm{Tr}[\hat{\boldsymbol{S}}\hat{P}_{\boldsymbol{k},\pm}] = \pm\frac{\boldsymbol{d}_{\boldsymbol{k}}}{2}. \tag{1.5}$$

Thus, the d-vector determines the spin texture in momentum space.

We now consider a two-dimensional electron gas system with the Rashba-type spin-orbit interaction. The simplest model of this system is given by the

two-band Hamiltonian (1.2) with

$$\begin{aligned} E^{(0)}_{\boldsymbol{k}} &= \frac{k_x^2 + k_y^2}{2m^*}, \\ \boldsymbol{B}_{\boldsymbol{k}} &= \alpha_R(\boldsymbol{k} \times \hat{z}), \\ \boldsymbol{d}_{\boldsymbol{k}} &= (\hat{\boldsymbol{k}} \times \hat{z}), \end{aligned} \tag{1.6}$$

where m^* is the effective mass, α_R denotes the Rashba-type interaction, and $\hat{\boldsymbol{k}} \equiv \boldsymbol{k}/|\boldsymbol{k}|$. The spin vector field $\boldsymbol{S}_{\boldsymbol{k},\pm} = \pm\boldsymbol{d}_{\boldsymbol{k}}/2$ has a singular point at the origin of the momentum space. Around this singularity, there is one spin vortex with the winding number[1] $+1$ for each band.

Another example is a topological insulator surface state [5, 6]. In a three-dimensional topological insulator, the bulk is an insulator, while its surface is a metal described by a massless Dirac Hamiltonian. Since the typical examples such as Bi_2Se_3 are induced by the strong spin-orbit interactions, the surface states are also discussed in terms of the spin-momentum locking. Let us consider the effective 4×4 Hamiltonian of the bulk of the typical topological insulator [13]:

$$\mathcal{H}^{bulk}_{\boldsymbol{k}} = v \sum_{i=1,2,3} k_i \hat{\sigma}_i \otimes \hat{\tau}_x + \Delta_{\boldsymbol{k}} \hat{1} \otimes \hat{\tau}_z, \tag{1.7}$$

where $\hat{\tau}_i$ are the Pauli matrices in orbit space related to the parity, and $\Delta_{\boldsymbol{k}} = M - A|\boldsymbol{k}|^2$ is the mass term. The surface state Hamiltonian can be easily obtained by solving the eigenenrgy problem of the Hamiltonian (1.7) in real space. We set the boundary in the z direction. By replacing k_z with $-i\partial_z$ and solving the one-dimensional Schrödingier equation in the z direction, we obtain the surface state Hamiltonian localized on the boundary [13]:

$$\mathcal{H}^{surface}_{\boldsymbol{k}} = v(\boldsymbol{k} \times \hat{z}) \cdot \hat{\boldsymbol{\sigma}}. \tag{1.8}$$

Actually, this Hamiltonian is one of the simplest examples of the two-band Hamiltonian (1.2), whose parameters are

$$\begin{aligned} E^{(0)}_{\boldsymbol{k}} &= 0, \\ \boldsymbol{B}_{\boldsymbol{k}} &= v(\boldsymbol{k} \times \hat{z}), \\ \boldsymbol{d}_{\boldsymbol{k}} &= (\hat{\boldsymbol{k}} \times \hat{z}). \end{aligned} \tag{1.9}$$

Note that the d-vector of the surface state is the same as that of the two-dimensional electron gas with the Rashba-type spin-orbit interaction [Fig. 1.1].

[1] The definition of the winding number is given in Chap. 4. Do not confuse with the similar notion *chirality*.

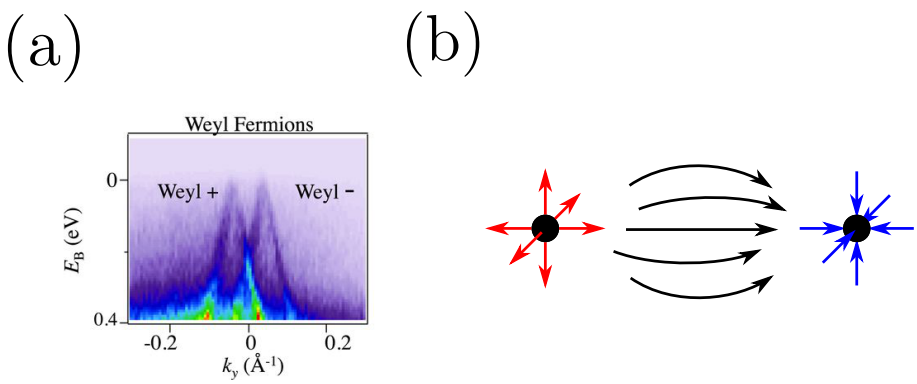

Figure 1.2: (a) Angle-resolved photoemission spectroscopy data of the Weyl semimetal TaAs from Ref. [11]. There are two Weyl points with opposite chirality. (b) Schematic picture of spin monopoles in three-dimensional momentum space.

Since $E^{(0)}_{\boldsymbol{k}} = 0$ in the low-energy region, the number of the Fermi surfaces of the surface state is one, while that of the Rashba electron gas is two. Another remarkable feature is that there is only one Dirac cone in the momentum space. This situation was thought to be impossible in condensed matter physics since the Nielsen-Ninomiya [14, 15] theorem states that the number of Dirac cones cannot be even in lattice systems. At first sight, the topological insulator surface state breaks this theorem. However, the surface state is not independent of the bulk and is not a self-standing two-dimensional lattice system.

In transport phenomena related to the spin-momentum locking, we often encounter the suppression of the signals due to the opposite contributions from two Fermi surfaces. In this sense, the topological insulator surface state is useful to get the giant signals.

1.1.3 Three-dimensional examples of spin-momentum locking

In three dimensions, a point-like singular structure in momentum space is called as the spin monopole. This spin structure is realized in the Weyl semimetals.

In three dimensions, there are two types of semimetals with linear-dispersions. One is called as the Dirac semimetal. The effective Hamiltonian is given by a

4×4 Dirac Hamiltonian

$$\mathcal{H}^D_{\boldsymbol{k}} = v \sum_{i=1,2,3} k_i \hat{\gamma}_i, \tag{1.10}$$

where $\hat{\gamma}_\mu$ are 4×4 gamma matrices satisfying $\{\hat{\gamma}_\mu, \hat{\gamma}_\nu\} = 2\delta_{\mu\nu}\hat{1}$. In realistic materials, gamma matrices contain spin Pauli matrices that describe the spin degeneracy. Since the Hamiltonian commutes with $\hat{\gamma}_0$, the Hamiltonian can be block-diagonalized with respect to the eigenvalues $\gamma_0 = \pm 1$. Two blocks are described by 2×2 Weyl Hamiltonians with the same dispersion and opposite chiralities. The spin texture in momentum space is ill-defined for the Dirac semimetals due to the spin degeneracy.

The other one is the Weyl semimetal. The Weyl semimetal can be induced by splitting the spin degeneracy in the Dirac semimetals [9]. This means that the Weyl semimetal has a pair of the linear dispersions around two different momenta, which are called the Weyl points. We describe the typical Weyl semimetal TaAs [11] in Fig. 1.2 (a). By redefining the momentum $\boldsymbol{k} \to \boldsymbol{k} - \boldsymbol{k}_\pm$, the typical effective Hamiltonians are given by the 2×2 Weyl Hamiltonians

$$\mathcal{H}^\pm_{\boldsymbol{k}} = \pm v \sum_{i=1,2,3} k_i \hat{\sigma}_i. \tag{1.11}$$

These Hamiltonians correspond to the Hamiltonian (1.2) with parameters

$$\begin{aligned} E^{(0)}_{\boldsymbol{k}} &= 0, \\ \boldsymbol{B}_{\boldsymbol{k}} &= v\boldsymbol{k}, \\ \boldsymbol{d}_{\boldsymbol{k}} &= \pm\hat{\boldsymbol{k}}. \end{aligned} \tag{1.12}$$

There are two singular points of the spin texture in three-dimensional momentum space, which correspond to the Weyl points. These Weyl points are characterized by the winding numbers[2] ± 1. The Weyl points are connected via *lines of magnetic force* each other [Fig. 1.2 (b)].

1.2 Spin-momentum locking: basic transport

We here describe the transport phenomena in a spin-momentum-locked material. As we saw, the topological insulator surface state is the typical and simplest example of the two-dimensional spin-momentum-locked materials. In this section,

[2]The three dimensional winding number is also called as the wrapping number. In this thesis, we use "the winding number" for general dimensions. The definition for general dimensions is given in Chap. 4.

we describe basic transport properties of the spin-momentum locking using the effective two-band Hamiltonian of the topological insulator surface state. We explain that the spin-momentum locking is a useful property both in spintronics and topological physics.

1.2.1 Rashba-Edelstein effect

We first discuss the basic electrical transport of the topological insulator surface state. In the presence of the spin-momentum-locked Fermi surface with the winding number +1, the Rashba-Edelstein effect [16], which is a kind of magnetoelectric effects, is induced by a DC electric field.

Let us remember the 2×2 effective Hamiltonian of a topological insulator surface state [see Eq. (1.8)]. The x-component electric current operator for this Hamiltonian is given by

$$\hat{j}_x = e\frac{\partial \mathcal{H}_{\boldsymbol{k}}}{\partial k_x} = -ve\hat{\sigma}_y, \tag{1.13}$$

where e is the elementary charge. Interestingly, the electric current operator is proportional to the spin operator and does not depend on the momentum for the lowest-order effective Hamiltonian. In the presence of the x-direction electric field E_x, we obtain

$$j_x = \langle \hat{j}_x \rangle_{neq} = -2ve\langle \hat{\sigma}_y/2 \rangle_{neq} = -2ve\delta S_y \propto E_x, \tag{1.14}$$

where $\langle \rangle_{neq}$ denotes the non-equilibrium expectation value in linear response theory, and δS_y is the y-component spin polarization. Since the topological insulator surface state is a metal, the spin polarization is induce by the electric field. This effect is called as the Rashba-Edelstein effect, which is originally discussed for a two-dimensional electron gas system with the Rashba-type spin-orbit interaction. In the original case, there are two spin-momentum-locked Fermi surfaces with different chiralities. Thus, most of the contributions are cancelled out each other, and the efficiency of the Rashba-Edelstein effect depends on the energy splitting of two bands. In this sense, the topological insulator is more efficient than the Rashba systems.

The Rashba-Edelstein effect is thought to be a souce of the efficient switching of the magnetization. Let us consider a coupling between the magnetization and the topological insulator surface state. For simplicity, we here consider the uniform magnetization whose direction is perpendicular to the topological insulator surface. In the presence of an electric field, the spin polarization induced by the Rashba-Edelstein effect behaves as a perpendicular magnetic field to the

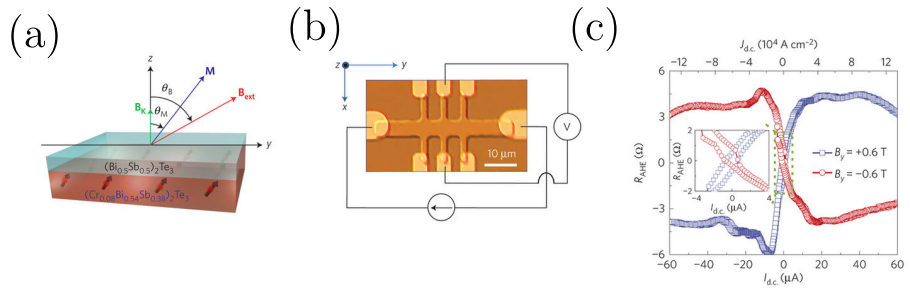

Figure 1.3: Figures from Ref. [19]. (a) Schematics of the bilayer heterostructure $(Bi_xSb_{1-x})_2Te_3/(Cr_yBi_zSb_{1-y-z})_2Te_3$. (b) Micrograph of the Hall bar device with schematic illustrations of the Hall measurement set-up. (c) Current dependence of the anomalous Hall effect for fixed in-plane magnetic fields.

magnetization. This means that a torque for the magnetization can be induced by the electric field, and the magnetization can be switched electrically. This torque is called the Rashba spin-orbit torque. A lot of experiments of detecting this torque have been performed [17, 18, 19]. In particular, a topological insulator/magnetically-doped topological insulator bilayer system is useful to show the existence of the spin-orbit torque. The details of an experiment for $(Bi_xSb_{1-x})_2Te_3/(Cr_yBi_zSb_{1-y-z})_2Te_3$ [19] are shown in Fig. 1.3. In this experiment, the spin-orbit torque in the topological insulator surface state acts on the in-plane magnetization, and the out-of-plane component of the magnetization is induced. The presence of the out-of-plane component leads to the anomalous Hall effect. Fig. 1.3 (c) shows that the electric current changes the direction of the magnetization, which results in the large anomalous Hall signal.

1.2.2 Qunatum anomalous Hall effect

In simple two-band electron systems, a spin texture in momentum space contains the information of topological properties of the systems. As an example, we here describe the Quantum anomalous Hall effect in two-band systems. We first consider this phenomenon for the general two-band models whose internal degrees of freedom are not limited to the spin. Then we move on to the recent realization of it in a magnetically-doped topological insulator.

Let us consider the insulator described by the Hamiltonian (1.2)[3]. By definition, there is a gap between two bands, and the chemical potential is in this gap. In the absence of impurities, the anomalous Hall conductivity at zero tem-

[3] $\hat{\sigma}$s are the Pauli matrices describing general internal degrees of freedom.

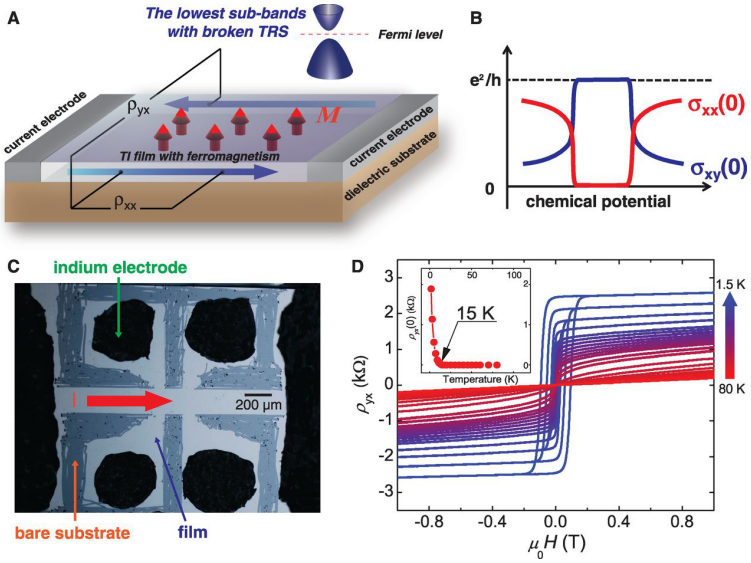

Figure 1.4: Figures from Ref. [20]. (A) Schematic picture of the quantum anomalous Hall measurement. (B) Schematic picture of the expected Hall conductivity. (C) An optical image of a Hall bar device made from $Cr_{0.15}(Bi_{0.1}Sb_{0.9})_{1.85}Te_3$ film. (D) Magnetic field dependence of Hall resistivity.

perature is given by [21]

$$\sigma_{xy} = -\frac{e^2}{2\pi}\mathcal{Q}, \tag{1.15}$$

where

$$\mathcal{Q} = \frac{1}{4\pi}\int_{BZ} d^2k \boldsymbol{d_k}\cdot(\partial_{k_x}\boldsymbol{d_k}\times\partial_{k_y}\boldsymbol{d_k}) \tag{1.16}$$

is the Pontryagin index. Here BZ denotes the Brilloin zone. Actually, this integral should be an integer that counts how many times the d-vector wraps around the sphere while we sweep the Brillouin zone. If this integer is nonzero, the system exhibits the Quantum anomalous Hall effect, and there are massless modes on the edge of the sample.

The nonzero-$\mathcal{Q}$-state can be realized in a magnetically-doped topological insulator. Since the Pauli matrices of the effective Hamiltonian for the surface state are defined in spin space, the gap can be induced by magnetic impurities. The effective two-band model of the doped topological insulator surface state is given by

$$\mathcal{H}_{\boldsymbol{k}} = v(\boldsymbol{k}\times\hat{z})\cdot\hat{\boldsymbol{\sigma}} + M\hat{\sigma}_z. \tag{1.17}$$

The behavior of the d-vector is as follows:

$$\begin{aligned} &\boldsymbol{d_k} \to (0,0,1) \text{ for } k \to 0, \\ &\boldsymbol{d_k} \to \hat{\boldsymbol{k}} \text{ for } k \to \infty. \end{aligned} \tag{1.18}$$

This spin texture is the so-called *meron* structure whose Pontryagin index[4] is $\mathcal{Q} = \mathrm{sgn}(M)/2$. This half-integer value is owing to the fact that the surface state is not a two-dimensional lattice system independent of the bulk. For each surface, there is one Dirac surface state, and it is characterized by $\mathcal{Q} = \mathrm{sgn}(M)/2$. Experimentally, we cannot extract the contribution from one surface. Thus, we obtain the quantized value ± 1. The details of the experiment [20] for $Cr_{0.15}(Bi_{0.1}Sb_{0.9})_{1.85}Te_3$ are shown in Fig. 1.4.

1.3 Topological insulator/ferromagnet bilayer

The spin-charge conversion is one of the main themes in spintronics. In conventional spin-charge conversion experiments, normal metals with the strong spin-orbit coupling such as platinum have been used because the spin Hall effect, in which the spin current is induced by an electric field, occurs in such materials. In the spin Hall effect, however, the spin polarization at the boundary is a secondary effect associated with the induced spin current. In this sense, more direct phenomenon is needed for the efficient spin-charge conversion.

In light of the situation, the spin-momentum-locked materials attract a lot of interests for its efficient spin-charge conversion property. As we saw, the electric current is directly converted to the spin polarization via the Rashba-Edelstein effect. In particular, the efficiency in the topological insulator surface state is expected to be better than other spin-momentum-locked materials because there is only one Fermi surface, which does not cause the suppression discussed above.

In the following, we review the spin-charge conversion in a topological insulator/ferromagnet heterostructure. We first explain several experiments performed in this heterostructures. Then we review microscopic theories that are expected to describe such experiments. In these theories, interactions between ferromagnetic magnons and spin-momentum-locked electrons play an important role in spin-charge conversion phenomena.

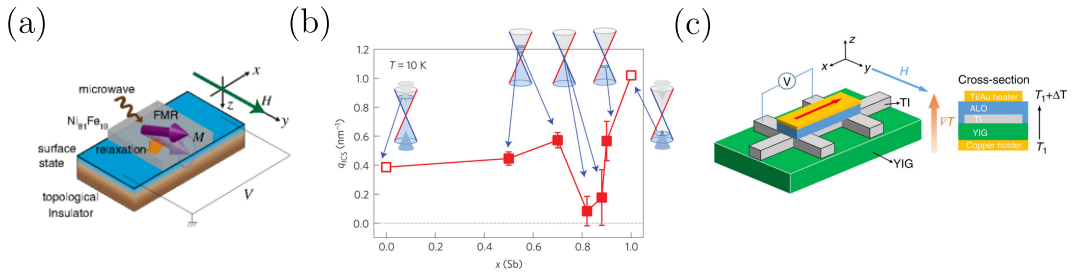

Figure 1.5: Figures of spin-charge conversion experiments in topological insulator/ferromagnet heterostructures. (a) Schematic picture of spin-pumping experiment from Ref. [22]. (b) Chemical potential dependence of charge-spin conversion efficiency from Ref. [23]. (c) Schematic picture of spin Seebeck measurement form Ref. [24].

1.3.1 Experiments

One of the typical experiments of the spin-charge conversion is the spin-pumping measurement. In this measurement, a ferromagnet is attached to a conductor. In the presence of microwave, the ferromagnetic resonance is induced in the ferromagnet, and spin current is injected into the attached conductor. This spin current is converted to charge current at the interface via the spin Hall effect or the spin-momentum locking, and a finite voltage is measured. Both of ferromagnetic metals and insulators are used as a spin current generator. The typical experimental setup [22] using a ferromagnetic metal $Ni_{81}Fe_{19}$ (permalloy) is shown in Fig. 1.5 (a). The magnetization is enforced in in-plane direction by applying the external magnetic field. The electric field induced by spin pumping is expected to be [22]

$$E_x = -\frac{4\pi}{e\tau k_F}\delta S_y, \tag{1.19}$$

where τ is the relaxation time of surface electrons, k_F is the Fermi energy of the surface state, and δS_y is the spin (density) accumulation induced by the spin pumping. Since the direction of the injected spin is proportional to the magnetization of the ferromagnet, the sign of induced electric field is changed under the sign change of the applied magnetic field. Using this property, we can extract the spin-momentum-locking contribution from the other contributions.

[4]Strictly speaking, it is not the Pontryagin index because the integration is not over the two-dimensional torus. This is the reason why this value is not quantized.

The above example is a spin-to-charge conversion experiment. A chage-to-spin conversion experiment has also been investigated in Ref. [23]. In this experiment, electric current induces the spin polarization in surface state, and it is injected into the attached ferromagnetic metal[5]. Fig. 1.5 (b) shows the chemical potential dependence of the charge-to-spin conversion efficiency. The chemical potential can be changed by changing the concentration of Sb in topological insulator $(Bi_{1-x}Sb_x)Te_3$. At the chemical potentials apart from the Dirac point, the charge-to-spin conversion efficiency is almost constant. Later we will compare this experimental data and a microscopic theory.

Another interesting experiment of spin-charge conversion is the spin Seebeck measurement that will be discussed in the next chapter. Spin current in ferromagnets is not only induced by the spin pumping but also by a thermal gradient. In the spin Seebeck measurement, spin current generated by a thermal gradient is converted to the voltage via the spin Hall effect or spin-momentum locking. In Ref. [24], a ferromagnetic insulator is used as the spin current generator. The efficiency of the spin Seebeck measurement in this heterostructure is much higher than that of the heterostructure using the spin Hall materials [24]. In the case of the ferromagnet, the spin current generation is understood in terms of ferromagnetic magnon excitations. The magnon spin current induced by the thermal gradient is injected into the attached topological insulator, and it is converted to the electric current. However, this phenomenological picture is not sufficient to explain some experimental data shown later. We will discuss this problem by comparing with a microscopic theory.

1.3.2 Microscopic theory of electrical transport

We here review Ref. [1]. This paper presents a microscopic theory of the charge-to-spin conversion in a topological insulator/ferromagnetic insulator heterostructure. In particular, the magnitude of the magnon spin current induced by electric field is evaluated. We first explain the microscopic theory in the Kubo formalism. Then we discuss the relation between this theory and the experiment [23].

In the following, we consider a model of the heterostructure in which a three-dimensional magnon gas is coupled with a two-dimensional massless Dirac electron system at the interface [Fig. 1.6]. A minimal Hamiltonian for the topological

[5]Strictly speaking, there is a copper layer between the topological insulator and ferromagnet.

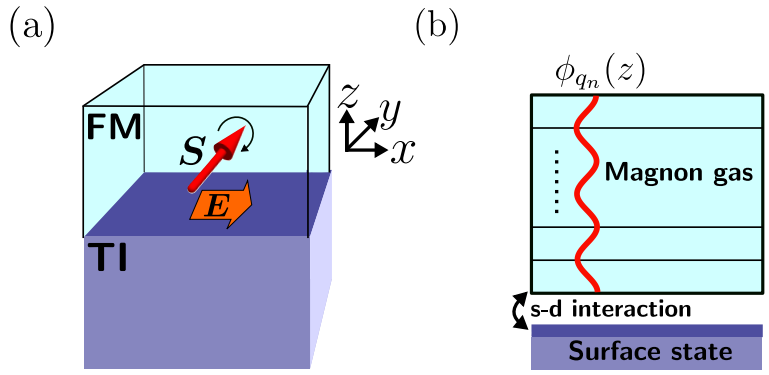

Figure 1.6: Schematic pictures of the topological insulator/ferromagnet heterostructures from Ref. [1]. (a) Setup. Spin is parallel to the interface. (b) Schematic picture of the model of the heterostructure. In z direction, we impose the Neumann boundary condition (1.23) for magnon wave functions.

surface state is given by

$$\begin{aligned} H_e &= \int \frac{d^2k}{(2\pi)^2} \psi_{\boldsymbol{k}}^\dagger \hat{\mathcal{H}}_e(\boldsymbol{k}) \psi_{\boldsymbol{k}}, \\ \hat{\mathcal{H}}_e(\boldsymbol{k}) &= -vk_x\hat{\sigma}_y + vk_y\hat{\sigma}_x - \mu\hat{1} \\ &= \sum_{\alpha=\pm} \xi_{\boldsymbol{k}}^\alpha |\boldsymbol{k},\alpha\rangle\langle\boldsymbol{k},\alpha|, \end{aligned} \tag{1.20}$$

where $(\psi, \psi^\dagger)$ are the two-component spinors of the surface-state electrons, $\boldsymbol{k} = (k_x, k_y)$ is the electron momentum, v is the Fermi velocity, $\mu > 0$ is the chemical potential, and $\hat{\sigma}_i$ are the Pauli matrices in spin space. The thermal Green's function of electrons is given by

$$\begin{aligned} \hat{\mathcal{G}}_{\boldsymbol{k}}(i\omega_n) &= \frac{1}{i\omega_n - \hat{\mathcal{H}}_e(\boldsymbol{k}) - \hat{\Sigma}_{imp}(i\omega_n, \boldsymbol{k})} \\ &\simeq \sum_{\alpha=\pm} |\boldsymbol{k},\alpha\rangle\langle\boldsymbol{k},\alpha| g_{\boldsymbol{k},\alpha}(i\omega_n), \end{aligned} \tag{1.21}$$

where $\omega_n = (2n+1)\pi T$, T is the temperature, $\hat{\Sigma}_{imp}$ is the impurity self-energy, and $g_{\boldsymbol{k},\alpha}(i\omega_n) = [i\omega_n - \xi_{\boldsymbol{k}}^\alpha + \mathrm{sgn}(\omega_n) i/2\tau]^{-1}$. We assume that the surface state is disordered by nonmagnetic impurities.

We consider the case where spins in the ferromagnet are parallel to the y direction, which is perpendicular to the electric field $\boldsymbol{E} = (E_x, 0, 0)$. The low-energy spin excitations of the ferromagnet are described by the magnon operators

$(a, a^\dagger)$, which are introduced by the spin-wave approximation: $S^y = S_0 - a^\dagger a$, $S^z + iS^x \simeq \sqrt{2S_0}a$, and $S^z - iS^x \simeq \sqrt{2S_0}a^\dagger$, where S^i and S_0 are the spin density operators and the magnitude of the spin density in the ferromagnet, respectively. In the following, we regard the ferromagnet as a three-dimensional magnon gas with a quadratic dispersion. Using magnon operators, we obtain a low-energy effective Hamiltonian for a three-dimensional isotropic ferromagnet:

$$H_m = \sum_{q_n} \int \frac{d^2q}{(2\pi)^2} \omega_{\boldsymbol{q},q_n} a^\dagger_{\boldsymbol{q},q_n} a_{\boldsymbol{q},q_n}, \tag{1.22}$$

where $\boldsymbol{q} = (q_x, q_y)$ is the two-dimensional momentum, $q_n = n\pi/La$ $(n = 0, 1, \ldots, L-1)$ is the z direction momentum, and $\omega_{\boldsymbol{q},q_n} = D(|\boldsymbol{q}|^2 + q_n^2)$ is the magnon dispersion with the stiffness D. We assume that the system has L sites with the lattice constant a in the z-direction We also assume that the magnon wave function in the z-direction is given by $\phi_{q_n}(z) = \sqrt{2/L}\cos q_n z$, which obeys the Neumann boundary condition [25]:

$$\partial_z \phi_{q_n}(z)|_{z=0} = \partial_z \phi_{q_n}(z)|_{z=La} = 0. \tag{1.23}$$

Note that this boundary condition is approximately valid in the case where the interaction between electrons and magnons at the interface is small. Using the above wave function, we obtain

$$\begin{aligned} a^{(\dagger)}_{\boldsymbol{q}}(z) &= \sum_{q_n} \phi_{q_n}(z) a^{(\dagger)}_{\boldsymbol{q},q_n}, \\ S^i_{\boldsymbol{q}}(z) &= \sum_{q_n} \phi_{q_n}(z) S^i_{\boldsymbol{q},q_n}, \end{aligned} \tag{1.24}$$

where $i = x, z$. Assuming that the dissipation of the magnon gas is negligible, the thermal Green's function of magnons is given by

$$\mathcal{D}_{\boldsymbol{q},q_n}(i\omega_m) = \frac{1}{i\omega_m - \omega_{\boldsymbol{q},q_n}}, \tag{1.25}$$

where $\omega_m = 2\pi m T$.

To include the interaction between the topological insulator and the ferro-

magnet, we consider the s-d Hamiltonian:

$$\begin{aligned} H_{sd} &= -\frac{J_{sd}a^2}{2}\int dxdy\psi^\dagger(x,y)\hat{\boldsymbol{\sigma}}\psi(x,y)\cdot\boldsymbol{S}(x,y,z=0), \\ &= -\frac{J_{sd}a^2}{2}\sum_{i=x,z}\int\frac{d^2kd^2k'}{(2\pi)^2(2\pi)^2}\psi^\dagger_{\boldsymbol{k}}\hat{\sigma}_i\psi_{\boldsymbol{k'}}S^i_{\boldsymbol{k'}-\boldsymbol{k}}(z=0) \\ &= -\frac{J_{sd}a^2}{2}\sqrt{\frac{2}{L}}\sum_{\substack{i=x,z,\\ q_n}}\int\frac{d^2kd^2k'}{(2\pi)^2(2\pi)^2}\psi^\dagger_{\boldsymbol{k}}\hat{\sigma}_i\psi_{\boldsymbol{k'}}S^i_{\boldsymbol{k'}-\boldsymbol{k},q_n}, \end{aligned} \tag{1.26}$$

where J_{sd} is the s-d exchange coupling. In the second line, we have ignored the y direction coupling, which only shifts the fermi surface position in momentum space, and introduce the Fourier transform. In the third line, we have used Eq. (1.24). Through this interaction, magnon spin and electron spin can be converted each other. Since the Fermi surface is spin-momentum locked, electron spin flip requires a large momentum shift on the Fermi surface. Thus, magnon spin is related with the electric field through the interactions between magnons and spin-momentum-locked electrons.

In the following, we consider the linear response theory of the above model in the presence of an electric field. We evaluate the expectation value of the magnon spin current induced by the electric field. The spin current operator at the interface is given by [26]

$$\begin{aligned} j_z^{S^y} &= \frac{1}{i}\left[\frac{S^y_{tot}}{V}, H_{sd}\right] = -\frac{1}{i}\left[\frac{s^y_{tot}}{V}, H_{sd}\right] \\ &= \epsilon_{yjk}\frac{J_{sd}a^2}{4V}\sqrt{\frac{2}{L}}\sum_{q_n}\int\frac{d^2kd^2k'}{(2\pi)^2(2\pi)^2}\psi^\dagger_{\boldsymbol{k}}\hat{\sigma}_k\psi_{\boldsymbol{k'}}S^j_{\boldsymbol{k'}-\boldsymbol{k},q_n}, \end{aligned} \tag{1.27}$$

where $S^y_{tot}=\int d^2xS^y$, $s^y_{tot}=\int d^2xs^y$ is the electron spin operator, and V is the two-dimensional volume of the interface. The expectation value of $j_z^{S^y}$ in the presence of the electric field $\boldsymbol{E}=(E_x,0,0)$ is given by the Kubo formula

$$\langle j_z^{S^y}\rangle = \left[\lim_{\omega\to 0}\frac{K^y(\omega+i0)-K^y(0)}{i\omega}\right]E_x, \tag{1.28}$$

where $K^y(\omega)$ is obtained from

$$K^y(i\omega_n) = \int_0^{1/T} d\tau e^{i\omega_n\tau}\langle \mathrm{T}_\tau j_z^{S^y}(\tau)j_x\rangle \tag{1.29}$$

by the analytic continuation $i\omega_n\to\omega+i0$. Here $j^x\equiv e\int d^2k/(2\pi)^2\psi^\dagger_{\boldsymbol{k}}\partial_{k_x}\hat{H}_e(\boldsymbol{k})\psi_{\boldsymbol{k}}$.

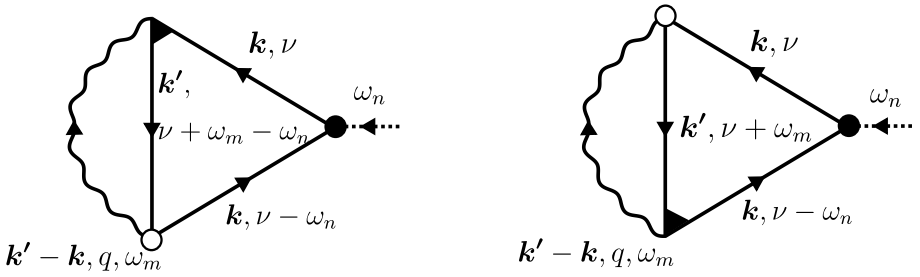

$$\blacktriangleright = -\frac{J_{sd}a^2}{4}(S_z\hat{\sigma}_x - S_x\hat{\sigma}_z), \bigcirc = -\frac{J_{sd}a^2}{2}(S_x\hat{\sigma}_x + S_z\hat{\sigma}_z), \bullet = -v\hat{\sigma}_y.$$

Figure 1.7: Diagrammatic expressions of the lowest-order contributions to $K^y(i\omega_n)$.

In the case of the conventional spin-orbit torque, lowest-order contributions to Eq. (1.28) are $\mathcal{O}(J_{sd})$:

$$\langle j_z^{S^y} \rangle \propto \epsilon_{yjk} \langle \psi^\dagger \hat{\sigma}_k \psi \rangle \langle S^j \rangle_{eq} + \mathcal{O}(J_{sd}^2), \tag{1.30}$$

where $\langle S^j \rangle_{eq}$ is the equilibrium expectation value of the FM spin, and $\langle\rangle$ denotes the non-equilibrium expectation value in the linear response regime without the effects of the magnet. In our case, on the other hand, $\mathcal{O}(J_{sd})$ contributions do not exist since $\langle S^x \rangle_{eq} = \langle S^z \rangle_{eq} = 0$. The lowest-order ($J_{sd}^2$) contributions to $K^y(i\omega_n)$ are expressed diagrammatically in Fig. 1.7. The solid and wavy lines denote the electron and magnon Green's functions, $\mathcal{G}$ and $\mathcal{D}$, respectively. After lengthy but straightforward calculations with some approximations, we obtain the following expression for induced magnon spin current:

$$\langle j_z^{S^y} \rangle = \frac{J_{sd}^2 a^5 S_0 (k_B T) \tau}{\hbar^2 v D} \frac{e k_F}{8\pi^2} E_x, \tag{1.31}$$

where we insert $\hbar$ and k_B for convenience. Note that the ratio of the spin current to the electric current does not depend on the chemical potential:

$$\frac{e\langle j_z^{S^y} \rangle}{\langle j_x \rangle} = \frac{J_{sd}^2 a^5 S_0 (k_B T)}{2\pi\hbar v^2 D}, \tag{1.32}$$

where we have used $\langle j_x \rangle = (e^2 \mu \tau / 4\pi\hbar) E_x$.

Finally, we discuss the relation between this theory and the experiment [23]. In this experiment, there is a copper layer between the topological insulator and the ferromagnet. In addition, the ferromagnet is not an insulator but a

metal. However, the basic mechanism might not be so far from the ferromagnetic insulator case since magnon descriptions can be applied to ferromagnetic metals at least to some extent. Equation (1.32) shows that the charge-to-spin conversion efficiency does not depend on the chemical potential of the surface state. This behavior has also been experimentally observed at the chemical potentials apart from the Dirac point [Fig. 1.5(b)]. In the experiment, the constant regime does not hold at the chemical potentials near the Dirac point. Equation (1.32) is not valid for such a region because we assume that the chemical potential is much larger than the impurity effect. We expect that an experiment in a topological insulator/ferromagnetic insulator heterostructure would be performed.

1.3.3 Microscopic theory of thermal transport

We here review Ref. [2]. This paper presents a theory for the spin Seebeck effect observed in a topological insulator/ferromagnetic insulator bilayer system. In particular, it evaluates the chemical potential dependence of the voltage on the topological insulator surface induced by a thermal gradient. The model in equilibrium is the same as the above theory. In this paper, however, the position-dependent distribution functions are introduced to describe the non-equilibrium state in the presence of a thermal gradient. We first explain a microscopic transport theory. Then we compare the numerical results with the experimental data.

To include both the position and momentum dependences, we treat this system in the semiclassical picture. We now consider the magnon Boltzmann equation in the presence of a thermal gradient:

$$\frac{\partial n_{\boldsymbol{q}}}{\partial t} + v_{q_z}\partial_z n_{\boldsymbol{q}} = \left.\frac{\partial n_{\boldsymbol{q}}}{\partial t}\right|_{scatt}, \tag{1.33}$$

where $n_{\boldsymbol{q}}$ is the position- and momentum-dependent magnon distribution function, $v_{q_z} = \partial_{q_z}\omega_{\boldsymbol{q}}$ is the magnon velocity, and the right-hand-side term is the scattering term. In the following, we adopt the relaxation-time approximation in which the scattering term is given by[6]

$$\left.\frac{\partial n_{\boldsymbol{q}}}{\partial t}\right|_{scatt} = -\frac{n_{\boldsymbol{q}} - n_{\boldsymbol{q}}^{(0)}(T(z))}{\tau_m}, \tag{1.34}$$

[6]Generally speaking, the determination of the magnon scattering term is not an easy task. There are a lot of different processes such as impurity and magnon-phonon scatterings. The approximation here assumes that the magnon distribution function relaxes into the local equilibrium with the local phonon temperature, which means that the total magnon number is not conserved.

where $n_{\boldsymbol{q}}^{(0)} = (\exp(\omega_{\boldsymbol{q}}/T(z)) - 1)^{-1}$ is the Bose distribution function with local temperature $T(z)$, and τ_m is a magnon relaxation time. For linear response to a temperature gradient, the Boltzmann equation becomes

$$v_{q_z}\left[\partial_z(\delta n_{\boldsymbol{q}}) + \partial_z T\frac{\partial n_{\boldsymbol{q}}^{(0)}}{\partial T}\right] = -\frac{\delta n_{\boldsymbol{q}}}{\tau_m}, \tag{1.35}$$

where $\delta n_{\boldsymbol{q}} \equiv n_{\boldsymbol{q}} - n_{\boldsymbol{q}}^{(0)}$ is the magnon distribution response. In the following, we solve Eq. (1.35) assuming specular reflection of magnons at the surface of the ferromagnetic insulator $z = 0$[7]. The solution for $q_z \geq 0$ is given by

$$\begin{aligned}
\delta n_{\boldsymbol{q}_\parallel, q_z}(z) &= -\tau_m |v_{q_z}| \partial_z T \frac{\partial n_{\boldsymbol{q}}^{(0)}}{\partial T}, \\
\delta n_{\boldsymbol{q}_\parallel, -q_z}(z) &= \tau_m |v_{q_z}| \partial_z T \frac{\partial n_{\boldsymbol{q}}^{(0)}}{\partial T}\left[1 - 2\exp\left(-\frac{|z|}{|v_{q_z}|\tau_m}\right)\right].
\end{aligned} \tag{1.36}$$

Note that

$$n_{\boldsymbol{q}_\parallel, q_z}(z = 0) = n_{\boldsymbol{q}_\parallel, -q_z}(z = 0). \tag{1.37}$$

Here we ignore the effect from the topological insulator. The validity of this approximation is discussed in Ref. [2].

Next, we consider the transport in the topological insulator surface state coupled with the magnon gas. We consider the linearized Boltzmann equation:

$$\frac{\partial f_{\boldsymbol{k}}}{\partial t} - e\boldsymbol{E}^{em} \cdot \boldsymbol{v}_{\boldsymbol{k}} \frac{\partial f_{\boldsymbol{k}}^{(0)}}{\partial \xi_{\boldsymbol{k}}} = \left.\frac{\partial f_{\boldsymbol{k}}}{\partial t}\right|_{imp} + \left.\frac{\partial f_{\boldsymbol{k}}}{\partial t}\right|_{em}, \tag{1.38}$$

where $\boldsymbol{E}^{em}$ is the induced electric field, $\boldsymbol{v}_{\boldsymbol{k}} = (v_x, v_y) = v(\cos\theta_{\boldsymbol{k}}, \sin\theta_{\boldsymbol{k}})$, $f_{\boldsymbol{k}}$ is the momentum-dependent electron distribution function, and $f_{\boldsymbol{k}}^{(0)} = (\exp(\xi_{\boldsymbol{k}}/T) + 1)^{-1}$ is the Fermi distribution function at temperature T. The terms on the right-hand side are the electron-impurity and electron-magnon-scattering collision terms, respectively. The electron-magnon-scattering term can be calculated by using the quantum Fokker-Planck equation [27], and is given to second order in the electron-magnon interaction by

[7] $z < 0$ and $z > 0$ regions correspond to the ferromagnetic insulator and topological insulator, respectively.

$$\left.\frac{\partial f_{\boldsymbol{k}}}{\partial t}\right|_{em} = 2\pi g^2 a^3 \int \frac{d^2 q_\parallel dq_z}{(2\pi)^3}$$
$$\Big[\ |\langle \boldsymbol{k}+\boldsymbol{q}_\parallel|\hat{\sigma}^-|\boldsymbol{k}\rangle|^2\ \delta(\omega_{\boldsymbol{q}}+\xi_{\boldsymbol{k}}-\xi_{\boldsymbol{k}+\boldsymbol{q}_\parallel})\left[(1-f_{\boldsymbol{k}})f_{\boldsymbol{k}+\boldsymbol{q}_\parallel}(1+n_{\boldsymbol{q}})-f_{\boldsymbol{k}}(1-f_{\boldsymbol{k}+\boldsymbol{q}_\parallel})n_{\boldsymbol{q}}\right]$$
$$+\ |\langle \boldsymbol{k}-\boldsymbol{q}_\parallel|\hat{\sigma}^+|\boldsymbol{k}\rangle|^2\delta(\omega_{\boldsymbol{q}}-\xi_{\boldsymbol{k}}+\xi_{\boldsymbol{k}-\boldsymbol{q}_\parallel})\left[(1-f_{\boldsymbol{k}})f_{\boldsymbol{k}-\boldsymbol{q}_\parallel}n_{\boldsymbol{q}}-f_{\boldsymbol{k}}(1-f_{\boldsymbol{k}-\boldsymbol{q}_\parallel})(1+n_{\boldsymbol{q}})\right]\Big], \tag{1.39}$$

where we have used $n_{\boldsymbol{q}}$ at $z=0$, and the $|\langle \boldsymbol{k'}|\hat{\sigma}^\pm|\boldsymbol{k}\rangle|^2$ factors account for the influence of spin-momentum locking in the Dirac cone on the electronic transition probabilities associated with magnon emission and absorption.

We are now in a position to derive an expression for the electric field induced by the electron-magnon interaction in the steady state. For simplicity, we use a relaxation-time approximation for the electron-impurity collision term in the steady-state electron Boltzmann equation:

$$-e\boldsymbol{E}^{em}\cdot\boldsymbol{v}_{\boldsymbol{k}}\frac{\partial f^{(0)}_{\boldsymbol{k}}}{\partial \xi_{\boldsymbol{k}}} = -\frac{\delta f_{\boldsymbol{k}}}{\tau_e} + \left.\frac{\partial f_{\boldsymbol{k}}}{\partial t}\right|_{em}, \tag{1.40}$$

where $\delta f_{\boldsymbol{k}} = f_{\boldsymbol{k}} - f^{(0)}_{\boldsymbol{k}}$, and τ_e is the relaxation time. Since the spin-Seebeck voltage is measured under open circuit conditions, it can be evaluated by finding the electric field strength at which the electric current vanishes:

$$\int \frac{d^2k}{(2\pi)^2}\boldsymbol{v}_{\boldsymbol{k}}\delta f_{\boldsymbol{k}} = 0. \tag{1.41}$$

Using Eqs. (1.40) and (1.41), we find that

$$E_i^{em} = \left[\int \frac{d^2k}{(2\pi)^2}\, v_i\, \left.\frac{\partial f_{\boldsymbol{k}}}{\partial t}\right|_{em}\right] \Big/ \left[-e\int \frac{d^2k}{(2\pi)^2} v_i^2 \frac{\partial f^{(0)}_{\boldsymbol{k}}}{\partial \xi_{\boldsymbol{k}}}\right]. \tag{1.42}$$

In deriving Eq. (1.42), we have appealed to isotropy in asserting that $\int d^2k v_x v_y = 0$. Note that E_i^{em} is independent of the electron-disorder scattering time τ_e.

In the following, we discuss the results of numerical calculation for realistic parameters [Fig. 1.8]. The chemical potential and electron density dependences of induced electric field are shown in Fig. 1.8 (b, c). Interestingly, the electric field is not a monotonic function of electron density. Naively, the electric field is expected to be enhanced due to the large density of states in which a lot of electrons can participate in the electron-magnon scattering. To understand this anomalous behavior, we plot the angle-dependent scattering amplitude in Fig.

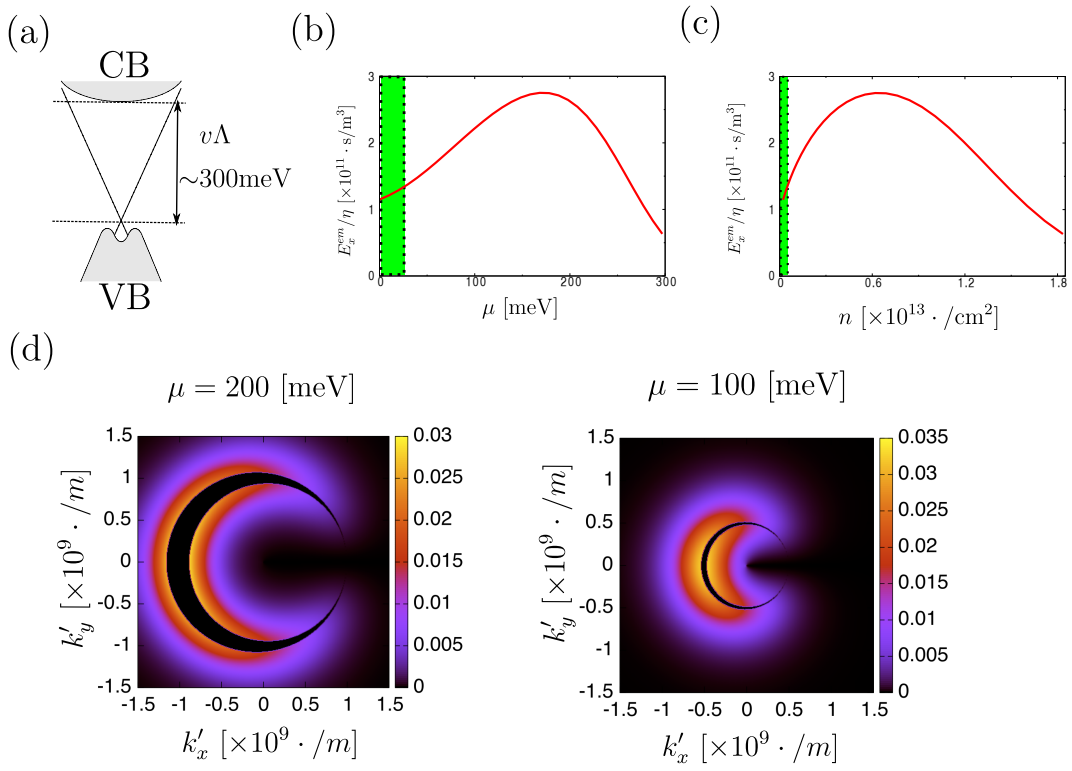

Figure 1.8: Figures from Ref. [2]. (a) Schematic illustration of the band structure of a Bi_2Te_3 film. The shaded regions labeled VB and CB are the bulk valence and conduction bands, respectively. The surface-state Dirac point is much closer to the valence band than to the conduction band. The thermally electric field at $T = 300$ K is plotted in (b) vs chemical potential and in (c) vs electron density. In the green region ($\mu \leq T$), the results are not accurate since we neglect the interband effect. (d) The electron-magnon scattering amplitude in arbitrary units for $\boldsymbol{k} = (k_F, 0)$ as a function of $\boldsymbol{k'}$ for chemical potential μ =100 and 200 meV relative to the Dirac point. The electron-magnon interaction vertex tends to be strongest for transitions between electronic states with opposite momentum.

1.8(d). At a high chemical potential ($\mu = 200$meV), electron-magnon scattering is forbidden in large portion of the momentum space, while it is not at a low chemical potential ($\mu = 100$meV). This is the reason why the induced electric field is suppressed at high electron density.

In experiment [24], the enhancement of spin Seebeck signal was observed near the Dirac point. The above theory explains the electric field enhancement at relatively small electron densities, although the simplified model does not achieve quantitative agreement.

1.3.4 Discussion

In this section, we have reviewed two papers about microscopic theories of the topological insulator/ferromagnetic insulator heterostructures. Although the methods used in these two studies are different, there are several common points. The most important point is that two phenomena cannot be understood in the simple Rashba-Edelstein picture. Phenomenologically, the Rashba-Edelstein effect is induced by the Fermi surface shift per unit time in momentum space. In the presence of the spin-momentum locking, the momentum shift $\boldsymbol{k} \to \boldsymbol{k} + \delta\boldsymbol{k}$ causes the spin change $\boldsymbol{S}_{\boldsymbol{k}} \to \boldsymbol{S}_{\boldsymbol{k}+\delta\boldsymbol{k}}$. On the other hand, the above two phenomena are induced by the electron-magnon interaction. The dominant process is the scattering between opposite side of the Fermi surface: $\boldsymbol{k} \propto (-1, 0) \to (1, 0)$. This scattering changes the sign of spin, and it causes the spin accumulation. This picture is completely different from the Rashba-Edelstein effect, which causes by the slight momentum shift. The above two theories indicate that results of experiments in spin-momentum-locked materials cannot always be interpreted in the Rashba-Edelstein regime.

1.4 Motivation of this thesis

A lot of studies about spin texture in momentum space have been done for the electron systems with the strong spin-orbit coupling. As we saw, the typical examples are the two-dimensional Rashba electron gas and a topological insulator phase induced by the strong spin-orbit coupling. In these materials, the spin vortex with winding number $+1$ appears in the momentum space, and the transport properties such as the Rashba-Edelstein effect have been extensively investigated. However, most of studies focus on the $+1$ spin vortex, and other spin structures have not been well investigated. In addition, the notion of the spin texture in momentum space is expected to be generalized to other quasiparticle systems. In this thesis, we treat the following two themes:

- Generalization of the spin-momentum locking to magnonic systems.
- Classification of the electron spin texture in three-dimensional momentum space under the space group symmetries by using the notion of orbifold.

First one is based on our paper [3].

In the first theme, we consider the magnon, which is a typical quasiparticle carrying the spin angular momentum. As we will see, magnons are useful quasiparticles especially in spintronics, and this generalization is important not only for theoretical interests but also for applications. We define the magnon spin and give some conditions for it to be independent of momentum. By avoiding such no-go conditions, we construct examples of magnon spin-momentum locking. Some of them are induced by a completely different mechanism from the electron case with large spin-orbit interaction. Also, we find that the magnon spin configuration is strongly restricted by the topology of the Brillouin zone, which is mathematically equivalent to the two-dimensional torus. This is the starting point of the second theme.

In the second theme, we classify the spin texture in momentum space under the space group symmetries. Since both spin and momentum are affected by the space group symmetries, the possible spin configuration is expected to be restricted by such symmetries. To include the space group symmetries, we introduce the momentum space orbifold. By considering the topology of the momentum space orbifolds for electron systems, we give the constraints for spin texture in momentum space for several space groups. Our purpose is to give a guiding principle to find Weyl points and high-winding-number spin monopoles in terms of the momentum space orbifold.

1.5 Structure of this thesis

In Chap. 2, we first briefly introduce the recent magnon physics. Then we construct the bosonic Bogoliubov-de-Gennes Hamiltonian for general spin Hamiltonian in the spin-wave approximation, and explain the eigenvalue problem by using the paraunitary matrices. Using the paraunitary matrices, we define the magnon spin, and give no-go conditions for magnon spin-momentum locking. We also introduce the notion of spin-momentum locking induced by the spontaneous symmetry breaking.

In Chap. 3, we construct examples of the magnon spin-momentum locking. We construct a one-dimensional example in a collinear antiferromagnet with the Dzyaloshinskii-Moriya interaction and two-dimensional examples in kagome lattice antiferromagnets whose ground states are 120° structures. In kagome

lattice examples, we find that there is a spin vortex characterized by the winding number -2, which has not been observed in electron systems. We also find that these are the first examples of the spin-momentum locking induced by the spontaneous symmetry breaking.

In Chap. 4, we introduce the Poincaré-Hopf index theorem, which relates the vector field on a manifold with the Euler characteristic of the manifold. By using this theorem, we derive the sum rule for winding numbers on the Brillouin zone and apply it to an example of the magnon spin-momentum locking. We also introduce the motivation of the following chapters.

In Chap. 5 and 6, we briefly review basics of the space group and orbifold. We define the basic terminologies for the later sections.

In Chap. 7, we introduce the momentum space orbifold. We first explain the behavior of crystal momentum and electron spin expectation value under the space group and time-reversal symmetry operations. Then we define the momentum space orbifolds for space groups and discuss the behaviors of spin as a pseudovector on the orbifold.

In Chap. 8, we consider 24 symmorphic space groups that consist of proper rotations. We construct the momentum space orbifold for each space group under the time-reversal symmetry. By combining the generalized Poincaré-Hopf index theorem, we derive the constraints for the spin texture in momentum space.

Chapter 2

Magnon spin-momentum locking: formalism

In this chapter, we generalize the concept of the spin-momentum locking to magnonic systems. We first give a brief introduction of the magnon physics. In particular, we focus on the spintronic and topological natures of magnons. Then we introduce the spin-wave approximation that describes the semiclassical behavior of magnons. After introducing the magnon Hamiltonian, we give the definition of magnon spin and conditions for it to be independent of momentum.

2.1 Magnon physics

The physics of magnons attracts a lot of interests in spintronics [28, 29, 30, 31] and topological physics [32, 33, 34, 35, 36, 37, 38, 39, 40, 41, 42, 43, 44]. Magnons are the quanta of spin wave excitations around the ordered magnetic ground state. Historically, magnons in a simple collinear Heisenberg ferromagnet and antiferromagnet have been well investigated [45, 46, 47]. There is a quadratic band without spin degeneracy in a simple ferromagnet, while there are two linear bands with spin degeneracy ($S = \pm 1$[1]) [Fig. 2.1]. This difference is reinterpreted in recent works about generalization of Nambu-Goldstone's theorem to the non-relativistic systems [48, 49]. In this sense, the physics of magnons has both well-established and developing aspects.

In addition to the well investigated magnons in simple collinear ferromagnets and antiferromagnets, we can also define magnons for non-collinear orders such as 120° structures in frustrated magnets and even for the incommensurate magnets such as the skyrmion lattice [50].

[1]The definition of spin of one-magnon states is given in Sec. 2.3.

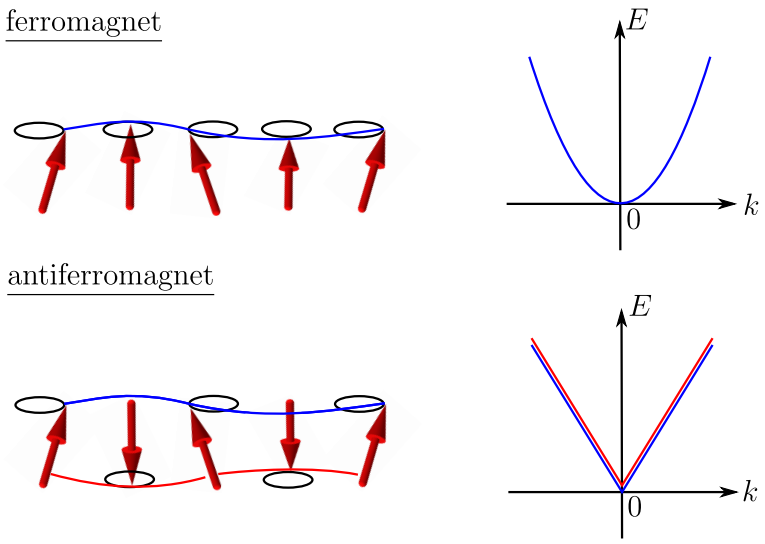

Figure 2.1: Schematic picture of magnon excitations in collinear ferromagnet and antiferromagnet. Typical dispersion relations are described in the right panel.

2.1.1 Magnons in spintronics

As a quasiparticle, a magnon has two outstanding features. First one is its low-dissipation nature. In magnets, the Gilbert damping is one of the main damping mechanisms of spin excitations. In the presence of this damping, magnon Green's function is given by [51]

$$\frac{1}{\omega - \xi_{\boldsymbol{k},a} + i\alpha\omega}, \tag{2.1}$$

where ω is the frequency, $\xi_{\boldsymbol{k},a}$ is a magnon dispersion, and α is the Gilbert damping coefficient. The damping term indicates that low energy magnons have small dissipation. If we consider magnetic insulators, the Gilbert damping coefficient α is quite small because there are no electron-magnon interactions. For instance, $\alpha \sim 10^{-4}$ for an insulating ferromagnet yttrium iron garnet (YIG). Thanks to this small Gilbert damping, the mean free path of magnons in YIG is about 10 μm even at room temperature [52].

Second one is that magnons carry spin angular momentum[2]. As an example, we here consider a simple Heisenberg ferromagnet. As we will describe in the

[2]There are exceptions such as magnons in triangular lattice Heisenberg antiferromagnet. Although they are also spin excitations, contributions for total spin angular momentum from three sub-lattices cancel each other.

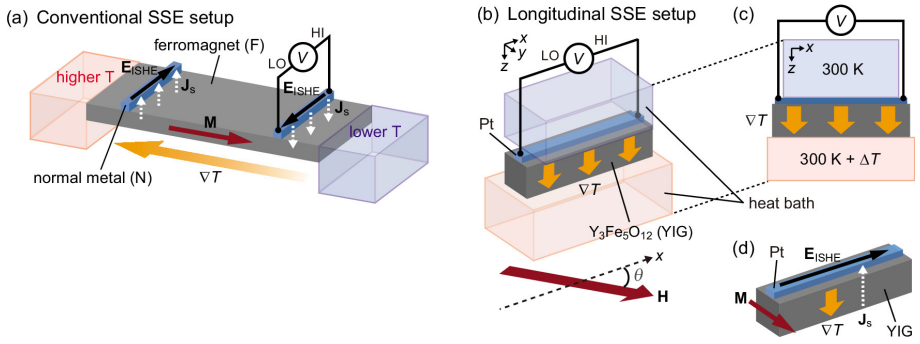

Figure 2.2: Schematic pictures of spin Seebeck effect from Ref. [29]. (a) The setup in early days. Longitudinal spin seebeck measurement is described in (b), (c), and (d).

next section, the magnons are described by bosonic excitations. In ferromagnets, the bosonic operators $(a, a^\dagger)$ describing magnons are proportional to the spin ladder operators (S^+, S^-). This means that creation of a magnon at some site corresponds to the reduction of the spin angular momentum by 1 at that site. Thus, the physical meaning of magnon current can be interpreted as the spin current.

These two features are useful in spintronics. In conventional spintronics, spin is carried only by electrons. As we discussed, the magnons in ferromagnets can also carry spin angular momentum. In particular, the dissipation of magnons in ferromagnetic insulators is far less than that of the electrons in conventional spintronic materials. Since magnons cannot be driven by an electric field, a thermal gradient is used in order to drive the magnons. This method is a simple analogue of the Seebeck effect in electron systems and called the spin Seebeck effect[3]. Experimentally, the magnon spin current induced by a thermal gradient is transformed into the voltage in metals attached to the ferromagnets by using the spin Hall effect. There are two types of experimental setups for measuring the spin Seebeck effect Fig. 2.2. In early days [53], the direction of flow of generated spin current is parallel to the spin Hall metal (Pt), and it was clearly inefficient. On the other hand, recent spin Seebeck measurements are performed in the so-called longitudinal setup in which spin current is perpendicularly injected into the spin Hall metal [29]. In the case of the antiferromagnetic magnon, the situation is completely changed [30]. Although antiferromagnetic magnons also have spin

[3]The spin Seebeck effect can also occur in ferromagnetic metals. In that case, carriers of spin current are electrons.

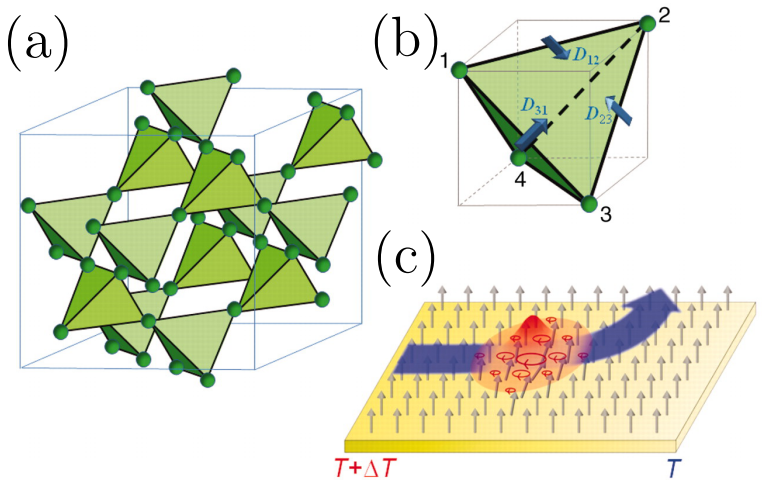

Figure 2.3: Figures from Ref. [34]. (a) The crystal structure of $Lu_2V_2O_7$. (b) Directions of Dzyaloshinskii-Moriya interactions. (c) Schematic picture of magnon Hall effect.

angular momentum, net magnon spin current is not induced due to the spin degeneracy of magnon bands. To observe the spin Seebeck effect in conventional antiferromagnets, we should apply the magnetic field to split the magnon spin degeneracy. Antiferromagntic spin Seebeck effect in the absence of the magnetic field is still an open question.

2.1.2 Topological aspects of magnonic systems

The magnonic systems have no internal degrees of freedom other than spin, while electron systems have atomic orbitals. However, this does not mean that magnon bands are not interesting. The existence of both chemical and magnetic sublattices allows magnonic systems to exhibit nontrivial band structures. In the field of magnonics [54], magnonic crystals, which are an artificial lattice consists of small magnets, allow physicists to design the magnon bands. In light of the situation, there appear a lot of analogue of topological band theories, which have been originally studied in electron systems.

One of the interesting issues is the magnon Hall effect [32, 33, 34, 35], which is an analogue of (anomalous) Hall effect. In simple ferromagnets and antiferromagnets discussed above, there is no interesting topological feature. If we consider some exotic factors such as noncollinear structures and Dzyaloshinskii-Moriya interactions, there can exist non-zero Berry curvature. The finite Berry

curvature affects the thermal transport of magnons as in the case of electron systems, and transverse magnon current is observed experimentally [34] [Fig. 2.3]. This phenomenon is called the magnon Hall effect. Similarly, there is a magnonic analogue of spin Hall effect called magnon spin Nernst effect [43, 44].

The topological band theory should be modified to apply to the magnonic systems. Non-interacting magnon Hamiltonians are described by bosonic Bogoliubov de-Gennes Hamiltonians, as we will see later. In general, the eigenenergy problem of the magnon systems is not equivalent to the diagonalization of bosonic Bogoliubov de-Gennes Hamiltonian matrix due to the boson commutation relations (see later sections). Shindou *et al*. formulated the calculations of Berry curvatures for general magnonic (bosonic) systems [36].

Although there are some differences from the electron systems, basic notions of topological insulators and semimetals have been generalized to magnonic systems. In topological magnon insulators [36, 37, 38, 39], there can exist topologically protected magnon edge modes. As well as the topological insulators, there are a lot of studies about the topological semimetals with linear dispersions called as Dirac (Weyl) semimetals and with nodal-line structure called as nodal-line semimetals. Magnonic analogues of such topological semimetals have also been investigated [40, 41, 42].

2.2 Spin-wave approximation

In general, it is difficult to obtain the energy spectrum of the given spin Hamiltonian because the system is essentially interacting. In ordered magnets with large spin, however, the simple spin-wave approximation can well describe the physics. In this section, we treat the general two-body spin Hamiltonians with commensurate ordered ground state(s) in the spin-wave approximation. We first introduce the Holstein-Primakoff bosons and construct the bosonic Bogoliubov-de-Gennes Hamiltonian. Then we explain the bosonic Bogoliubov transformation, which is essentially different from the diagonalization in the fermionic version.

2.2.1 Holstein-Primakoff boson

We consider a spin Hamiltonian defined on a lattice with an ordered classical ground state and treat the magnet in the semiclassical picture. In the limit of large spin, quantum spin fluctuations around the classical ground state can be treated as small perturbations. For convenience, we define the local rotating frame $\{\boldsymbol{M}_p^x, \boldsymbol{M}_p^y, \boldsymbol{M}_p^z\}$ in which $\boldsymbol{M}_p^z$ is in the direction of the classical spin at site p. Here $\boldsymbol{M}_p^i$ are unit vectors. The spin operator $\boldsymbol{S}_p$ can be expressed in terms

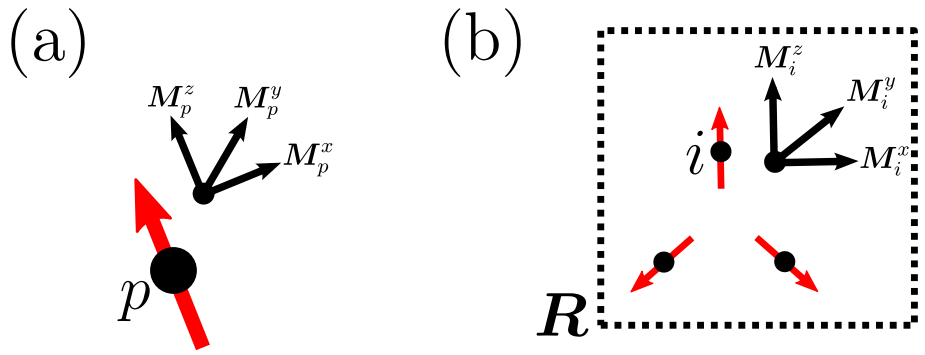

Figure 2.4: (a) Schematic picture of the local rotating frame at site p. (b) Schematic picture of magnetic unit cell. $\boldsymbol{R}$ and i denote the magnetic lattice vector and magnetic sublattice index, respectively.

of $\{\boldsymbol{M}_p^a\}$,

$$\boldsymbol{S}_p = \sum_a \tilde{S}_p^a \boldsymbol{M}_p^a, \tag{2.2}$$

where $\tilde{S}_p^a$ are a-component spin operators in the rotating frame [Fig. 2.4 (a)].

To treat the small quantum spin fluctuations, we introduce the Holstein-Primakoff transformation [47],

$$\begin{aligned} \tilde{S}_p^z &= S_0 - a_p^\dagger a_p, \\ \tilde{S}_p^+ &= (2S_0 - a_p^\dagger a_p)^{1/2} a_p, \\ \tilde{S}_p^- &= a_p^\dagger (2S_0 - a_p^\dagger a_p)^{1/2}, \end{aligned} \tag{2.3}$$

where $\tilde{S}_p^\pm = \tilde{S}_p^x \pm i\tilde{S}_p^y$, S_0 is the size of the spin, and $(a_p, a_p^\dagger)$ are the Holstein-Primakoff boson operators, which satisfy $[a_p, a_q^\dagger] = \delta_{p,q}$. The expressions (2.3) exactly satisfy the $SU(2)$ commutator algebra $[\tilde{S}_p^a, \tilde{S}_q^b] = i\delta_{p,q}\epsilon_{abc}\tilde{S}_p^c$. For sufficiently large S_0, it is convenient to introduce the spin-wave approximation,

$$\begin{aligned} \tilde{S}_p^z &\simeq S_0 - a_p^\dagger a_p, \\ \tilde{S}_p^\pm &\simeq \sqrt{2S_0} a_p^{(\dagger)}. \end{aligned} \tag{2.4}$$

Using this approximation, we can solve the spin-Hamiltonian since it is written as a quadratic form of bosonic operators. We can rewrite the spin operator as

$$\boldsymbol{S}_p \simeq \boldsymbol{M}_p^z (S_0 - a_p^\dagger a_p) + \boldsymbol{M}_p^x \sqrt{2S_0} \frac{a_p + a_p^\dagger}{2} + \boldsymbol{M}_p^y \sqrt{2S_0} \frac{a_p - a_p^\dagger}{2i}. \tag{2.5}$$

2.2.2 Bosonic Bogoliubov-de Gennes Hamiltonian

A general two-body spin interaction Hamiltonian is given by

$$H = \frac{1}{2}\sum_{\boldsymbol{R},\boldsymbol{R'}}\sum_{i,j=1}^{N}\sum_{a,b} J_{ij}^{ab}(\boldsymbol{R},\boldsymbol{R'})S_{\boldsymbol{R},i}^{a}S_{\boldsymbol{R'},j}^{b}, \tag{2.6}$$

where $\boldsymbol{S}_{\boldsymbol{R},i} = (S_{\boldsymbol{R},i}^{x}, S_{\boldsymbol{R},i}^{y}, S_{\boldsymbol{R},i}^{z})$ is the spin operator at each site, $\boldsymbol{R}, \boldsymbol{R'}$ denote the magnetic lattice vectors, i, j denote the magnetic-sublattice indices, and N is the number of sites in a magnetic unit cell. Suppose that the classical ground state of the Hamiltonian (2.6) is magnetically ordered, and $|\boldsymbol{S}_{\boldsymbol{R},i}|$ is sufficiently large enough to be treated in the semiclassical picture. To rewrite the spin Hamiltonian (2.6) in terms of spin excitations (magnons) around a classical ground state, we introduce the Holstein-Primakoff boson operators $(a, a^{\dagger})$ and the spin-wave approximation,

$$\boldsymbol{S}_{\boldsymbol{R},i} \simeq \boldsymbol{M}_{i}^{z}(S_0 - a_{\boldsymbol{R},i}^{\dagger}a_{\boldsymbol{R},i}) + \boldsymbol{M}_{i}^{x}\sqrt{2S_0}\frac{a_{\boldsymbol{R},i} + a_{\boldsymbol{R},i}^{\dagger}}{2} + \boldsymbol{M}_{i}^{y}\sqrt{2S_0}\frac{a_{\boldsymbol{R},i} - a_{\boldsymbol{R},i}^{\dagger}}{2i}, \tag{2.7}$$

where S_0 is the size of the spin that can depend on the site, and $\{\boldsymbol{M}_{i}^{a}\}$ is the set of the basis vectors of the rotating frame in which $\boldsymbol{M}_{i}^{z}$ is in the direction of the classical spin at the magnetic sublattice i [Fig. 2.4 (b)]. Substituting Eq. (2.7) into Eq. (2.6), we obtain

$$H = \frac{1}{2}\sum_{\boldsymbol{k}}(\boldsymbol{a}_{\boldsymbol{k}}^{\dagger}, \boldsymbol{a}_{-\boldsymbol{k}}) \cdot \hat{\mathcal{H}}_{\boldsymbol{k}} \cdot \begin{pmatrix} \boldsymbol{a}_{\boldsymbol{k}} \\ \boldsymbol{a}_{-\boldsymbol{k}}^{\dagger} \end{pmatrix}, \tag{2.8}$$

where $\boldsymbol{k}$ is the crystal momentum, $\boldsymbol{a}_{\boldsymbol{k}}^{\dagger} = (a_{\boldsymbol{k},1}^{\dagger}, \cdots, a_{\boldsymbol{k},N}^{\dagger})$, and $\hat{\mathcal{H}}_{\boldsymbol{k}}$ is a $2N \times 2N$ bosonic Bogoliubov-de Gennes (BdG) Hamiltonian. Note that we ignore magnon-magnon interactions in the spin-wave approximation.

2.2.3 Bosonic Bogoliubov transformation

In comparison with the fermionic BdG Hamiltonian, the bosonic BdG Hamiltonian cannot be solved by the diagonalization using unitary matrices. We first review the fermionic Bogoliubov transformation of the fermionic Hamiltonian

$$H_f = \frac{1}{2}\sum_{\boldsymbol{k}}(\boldsymbol{f}_{\boldsymbol{k}}^{\dagger}, \boldsymbol{f}_{-\boldsymbol{k}}) \cdot \hat{\mathcal{H}}_{\boldsymbol{k}}^{f} \cdot \begin{pmatrix} \boldsymbol{f}_{\boldsymbol{k}} \\ \boldsymbol{f}_{-\boldsymbol{k}}^{\dagger} \end{pmatrix}, \tag{2.9}$$

where $\boldsymbol{f}_{\boldsymbol{k}}^{\dagger} = (f_{\boldsymbol{k},1}^{\dagger}, \cdots, f_{\boldsymbol{k},N}^{\dagger})$ are the fermionic field operators, and $\hat{\mathcal{H}}_{\boldsymbol{k}}^{f}$ is a $2N \times 2N$ fermionic BdG Hamiltonian. Using a $2N \times 2N$ unitary matrix $\hat{U}_{\boldsymbol{k}}$, we can diagonalize the Hamiltonian (2.9):

$$\begin{aligned} H_f &= \frac{1}{2}\sum_{\boldsymbol{k}} (\boldsymbol{f}_{\boldsymbol{k}}^{\dagger}, \boldsymbol{f}_{-\boldsymbol{k}}) \cdot \hat{U}_{\boldsymbol{k}} \hat{U}_{\boldsymbol{k}}^{-1} \hat{\mathcal{H}}_{\boldsymbol{k}}^{f} \hat{U}_{\boldsymbol{k}} \hat{U}_{\boldsymbol{k}}^{-1} \cdot \begin{pmatrix} \boldsymbol{f}_{\boldsymbol{k}} \\ \boldsymbol{f}_{-\boldsymbol{k}}^{\dagger} \end{pmatrix} \\ &= \frac{1}{2}\sum_{\boldsymbol{k}} (\boldsymbol{f}_{\boldsymbol{k}}^{\dagger}, \boldsymbol{f}_{-\boldsymbol{k}}) \cdot \hat{U}_{\boldsymbol{k}} \begin{pmatrix} \hat{E}_{\boldsymbol{k}} & 0 \\ 0 & -\hat{E}_{-\boldsymbol{k}} \end{pmatrix} \hat{U}_{\boldsymbol{k}}^{-1} \cdot \begin{pmatrix} \boldsymbol{f}_{\boldsymbol{k}} \\ \boldsymbol{f}_{-\boldsymbol{k}}^{\dagger} \end{pmatrix} \\ &= \frac{1}{2}\sum_{\boldsymbol{k}} (\boldsymbol{g}_{\boldsymbol{k}}^{\dagger}, \boldsymbol{g}_{-\boldsymbol{k}}) \cdot \begin{pmatrix} \hat{E}_{\boldsymbol{k}} & 0 \\ 0 & -\hat{E}_{-\boldsymbol{k}} \end{pmatrix} \cdot \begin{pmatrix} \boldsymbol{g}_{\boldsymbol{k}} \\ \boldsymbol{g}_{-\boldsymbol{k}}^{\dagger} \end{pmatrix} \end{aligned} \tag{2.10}$$

where $\hat{E}_{\boldsymbol{k}} = \mathrm{diag}(E_{\boldsymbol{k},1}, \cdots, E_{\boldsymbol{k},\alpha}, \cdots, E_{\boldsymbol{k},N})$ and

$$g_{\boldsymbol{k},\alpha} = [\hat{U}_{\boldsymbol{k}}^{-1}]_{\alpha,i} f_{\boldsymbol{k},i} + [\hat{U}_{\boldsymbol{k}}^{-1}]_{\alpha,i+N} f_{-\boldsymbol{k},i}^{\dagger}. \tag{2.11}$$

It is important to note that $(g, g^{\dagger})$ satisfy the fermionic anticommutation relations:

$$\begin{aligned} \{g_{\boldsymbol{k},\alpha}, g_{\boldsymbol{k},\beta}^{\dagger}\} &= [\hat{U}_{\boldsymbol{k}}^{-1}]_{\alpha,i} [\hat{U}_{\boldsymbol{k}}]_{j,\beta} \{f_{\boldsymbol{k},i}, f_{\boldsymbol{k},j}^{\dagger}\} + [\hat{U}_{\boldsymbol{k}}^{-1}]_{\alpha,i+N} [\hat{U}_{\boldsymbol{k}}]_{j+N,\beta} \{f_{-\boldsymbol{k},i}^{\dagger}, f_{-\boldsymbol{k},j}\} \\ &= [\hat{U}_{\boldsymbol{k}}^{-1}]_{\alpha,i} [\hat{U}_{\boldsymbol{k}}]_{i,\beta} + [\hat{U}_{\boldsymbol{k}}^{-1}]_{\alpha,i+N} [\hat{U}_{\boldsymbol{k}}]_{i+N,\beta} = \delta_{\alpha\beta}, \\ \{g_{\boldsymbol{k},\alpha}, g_{\boldsymbol{k},\beta}\} &= \{g_{\boldsymbol{k},\alpha}^{\dagger}, g_{\boldsymbol{k},\beta}^{\dagger}\} = 0. \end{aligned} \tag{2.12}$$

Thus, $\{E_{\boldsymbol{k},\alpha}\}$ corresponds to the set of eigenvalues of the Hamiltonian (2.9).

Unfortunately, the above argument cannot be applied to the bosonic BdG Hamiltonian. Replacing $\{,\}$ with $[,]$ and f, g with a, b in the first equation of (2.12), we obtain

$$\begin{aligned} [b_{\boldsymbol{k},\alpha}, b_{\boldsymbol{k},\beta}^{\dagger}] &= [\hat{U}_{\boldsymbol{k}}^{-1}]_{\alpha,i} [\hat{U}_{\boldsymbol{k}}]_{j,\beta} [a_{\boldsymbol{k},i}, a_{\boldsymbol{k},j}^{\dagger}] + [\hat{U}_{\boldsymbol{k}}^{-1}]_{\alpha,i+N} [\hat{U}_{\boldsymbol{k}}]_{j+N,\beta} [a_{-\boldsymbol{k},i}^{\dagger}, a_{-\boldsymbol{k},j}] \\ &= [\hat{U}_{\boldsymbol{k}}^{-1}]_{\alpha,i} [\hat{U}_{\boldsymbol{k}}]_{i,\beta} - [\hat{U}_{\boldsymbol{k}}^{-1}]_{\alpha,i+N} [\hat{U}_{\boldsymbol{k}}]_{i+N,\beta} \neq \delta_{\alpha\beta}. \end{aligned} \tag{2.13}$$

The equation (2.13) means that the new operators $(b, b^{\dagger})$ do not satisfy the bosonic commutation relation, and the eigenvalues of the bosonic BdG Hamiltonian matrix do not correspond to the eigenvalues of the Hamiltonian (2.8).

Instead of a unitary matrix, we use a paraunitary matrix $\hat{Q}$, which satisfies

$$\hat{Q}^{\dagger} \hat{\Sigma}_3 \hat{Q} = \hat{Q} \hat{\Sigma}_3 \hat{Q}^{\dagger} = \hat{\Sigma}_3, \tag{2.14}$$

where $[\hat{\Sigma}_3]_{i,j} = \delta_{ij}\sigma_j$ with $\sigma_j = +1$ for $j = 1, \cdots, N$ and $\sigma_j = -1$ for $j = N+1, \cdots, 2N$. Using a paraunitary matrix $\hat{Q}_{\boldsymbol{k}}$, the bosonic Bogoliubov transformation is defined as

$$\hat{Q}_{\boldsymbol{k}}^{\dagger}\hat{\mathcal{H}}_{\boldsymbol{k}}\hat{Q}_{\boldsymbol{k}} = \begin{pmatrix} \hat{E}_{\boldsymbol{k}} & 0 \\ 0 & \hat{E}_{-\boldsymbol{k}} \end{pmatrix},$$
$$H = \sum_{\boldsymbol{k},\alpha} E_{\boldsymbol{k},\alpha} b_{\boldsymbol{k},\alpha}^{\dagger} b_{\boldsymbol{k},\alpha}, \tag{2.15}$$

where $\hat{Q}_{\boldsymbol{k}}, \hat{Q}_{\boldsymbol{k}}^{\dagger}$ are $2N \times 2N$ paraunitary matrices and $\hat{E}_{\boldsymbol{k}} = \mathrm{diag}(E_{\boldsymbol{k},1}, \cdots, E_{\boldsymbol{k},\alpha}, \cdots, E_{\boldsymbol{k},N})$. $(b, b^{\dagger})$ are the magnon field operators, which satisfy

$$b_{\boldsymbol{k},\alpha} = [\hat{Q}_{\boldsymbol{k}}^{-1}]_{\alpha,i} a_{\boldsymbol{k},i} + [\hat{Q}_{\boldsymbol{k}}^{-1}]_{\alpha,i+N} a_{-\boldsymbol{k},i}^{\dagger}$$
$$b_{\boldsymbol{k},\alpha}^{\dagger} = [\hat{Q}_{\boldsymbol{k}}^{-1}]_{i,\alpha}^{\dagger} a_{\boldsymbol{k},i}^{\dagger} + [\hat{Q}_{\boldsymbol{k}}^{-1}]_{i+N,\alpha}^{\dagger} a_{-\boldsymbol{k},i}, \tag{2.16}$$

or equivalently,

$$a_{\boldsymbol{k},i} = [\hat{Q}_{\boldsymbol{k}}]_{i,\alpha} b_{\boldsymbol{k},\alpha} + [\hat{Q}_{\boldsymbol{k}}]_{i,\alpha+N} b_{-\boldsymbol{k},\alpha}^{\dagger}$$
$$a_{\boldsymbol{k},i}^{\dagger} = [\hat{Q}_{\boldsymbol{k}}]_{\alpha,i}^{\dagger} b_{\boldsymbol{k},\alpha}^{\dagger} + [\hat{Q}_{\boldsymbol{k}}]_{\alpha+N,i}^{\dagger} b_{-\boldsymbol{k},\alpha}. \tag{2.17}$$

It is important to note that $(b, b^{\dagger})$ satisfy the bosonic commutation relations:

$$\begin{aligned}
[b_{\boldsymbol{k},\alpha}, b_{\boldsymbol{k},\beta}^{\dagger}] &= [\hat{Q}_{\boldsymbol{k}}^{-1}]_{\alpha,i} [\hat{Q}_{\boldsymbol{k}}^{-1}]_{j,\beta}^{\dagger} [a_{\boldsymbol{k},i}, a_{\boldsymbol{k},j}^{\dagger}] + [\hat{Q}_{\boldsymbol{k}}^{-1}]_{\alpha,i+N} [\hat{Q}_{\boldsymbol{k}}^{-1}]_{j+N,\beta}^{\dagger} [a_{-\boldsymbol{k},i}^{\dagger}, a_{-\boldsymbol{k},j}] \\
&= [\hat{Q}_{\boldsymbol{k}}^{-1}]_{\alpha,i} [\hat{Q}_{\boldsymbol{k}}^{-1}]_{i,\beta}^{\dagger} - [\hat{Q}_{\boldsymbol{k}}^{-1}]_{\alpha,i+N} [\hat{Q}_{\boldsymbol{k}}^{-1}]_{i+N,\beta}^{\dagger} \\
&= [\hat{Q}_{\boldsymbol{k}}^{-1} \hat{\Sigma}_3 (\hat{Q}_{\boldsymbol{k}}^{-1})^{\dagger}]_{\alpha,\beta} = [\hat{Q}_{\boldsymbol{k}}^{\dagger} \hat{\Sigma}_3 \hat{Q}_{\boldsymbol{k}}]_{\alpha,\beta}^{-1} = [\hat{\Sigma}_3]_{\alpha,\beta} = \delta_{\alpha\beta}, \\
[b_{\boldsymbol{k},\alpha}, b_{\boldsymbol{k},\beta}] &= [b_{\boldsymbol{k},\alpha}^{\dagger}, b_{\boldsymbol{k},\beta}^{\dagger}] = 0.
\end{aligned} \tag{2.18}$$

In the third line, we have used the paraunitarity relation (2.14).

In the presence of off-diagonal terms such as aa and $a^{\dagger}a^{\dagger}$, $\hat{Q}_{\boldsymbol{k}}^{\dagger} \neq \hat{Q}_{\boldsymbol{k}}^{-1}$, and the bosonic Bogoliubov transformation is not a diagonalization

$$\hat{P}^{-1} \hat{A} \hat{P} = \hat{D}, \tag{2.19}$$

where $\hat{A}$ is a matrix, $\hat{P}$ is a regular matrix, and $\hat{D}$ is a diagonal matrix.

2.3 Definition of magnon spin

In the following, we define the magnon spin using the expressions in the previous sections. The magnon spin is defined as the difference in total spin angular momentum between a one-magnon state and the ground state,

$$\boldsymbol{S}_{\boldsymbol{k},\alpha} \equiv \langle \boldsymbol{k}, \alpha | \boldsymbol{S}_{\mathrm{tot}} | \boldsymbol{k}, \alpha \rangle - \langle 0 | \boldsymbol{S}_{\mathrm{tot}} | 0 \rangle, \tag{2.20}$$

where $|0\rangle$ is the Fock vacuum of $(b, b^\dagger)$ [4], $|\boldsymbol{k}, \alpha\rangle \equiv b^\dagger_{\boldsymbol{k},\alpha}|0\rangle$, and

$$\boldsymbol{S}_{\rm tot} = \sum_{\boldsymbol{R}} \sum_{i} \boldsymbol{S}_{\boldsymbol{R},i} \tag{2.21}$$

is the total spin operator.

To derive the explicit form of the magnon spin, we rewrite the total spin operator in terms of $(b, b^\dagger)$:

$$\begin{aligned}
\boldsymbol{S}_{\rm tot} &= \sum_{\boldsymbol{R}} \sum_{i} \boldsymbol{S}_{\boldsymbol{R},i} \\
&\simeq \sum_{\boldsymbol{R}} \sum_{i} \boldsymbol{M}^z_i (S_0 - a^\dagger_{\boldsymbol{R},i} a_{\boldsymbol{R},i}) + (\text{first-order terms of } a, a^\dagger) \\
&= \sum_{\boldsymbol{k}} \sum_{i} (-\boldsymbol{M}^z_i) a^\dagger_{\boldsymbol{k},i} a_{\boldsymbol{k},i} + (\text{zeroth- and first-order terms of } a, a^\dagger) \\
&= \sum_{\boldsymbol{k},\alpha} \left[\sum_i (-\boldsymbol{M}^z_i) \left\{ |[\hat{Q}_{\boldsymbol{k}}]_{i,\alpha}|^2 + |[\hat{Q}_{-\boldsymbol{k}}]_{i,\alpha+N}|^2 \right\} \right] b^\dagger_{\boldsymbol{k},\alpha} b_{\boldsymbol{k},\alpha} + (\text{off-diagonal terms}) \\
&\quad + (\text{zeroth- and first-order terms of } b, b^\dagger).
\end{aligned} \tag{2.22}$$

In the second and fourth lines, we have used Eqs. (2.7) and (2.17), respectively. Substituting Eq. (2.22) into Eq. (2.20), we obtain[5]

$$\boldsymbol{S}_{\boldsymbol{k},\alpha} \simeq \sum_i (-\boldsymbol{M}^z_i) \left\{ |[\hat{Q}_{\boldsymbol{k}}]_{i,\alpha}|^2 + |[\hat{Q}_{-\boldsymbol{k}}]_{i,\alpha+N}|^2 \right\}. \tag{2.23}$$

The physical interpretation of the formula (2.23) is as follows. The Holstein-Primakoff creation operator $a^\dagger_{\boldsymbol{R},i}$ is physically equivalent to the spin lowering operator with respect to the classical spin direction $\boldsymbol{M}^z_i$ [see Eq. (2.4)]. In the presence of one Holstein-Primakoff boson at a sublattice i, the change of the total spin is $-\boldsymbol{M}^z_i$. Since a one-magnon state $|\boldsymbol{k}, \alpha\rangle$ is described as the superposition of Holstein-Primakoff one-boson states, the magnon spin can be interpreted as

$$\sum_i [-(\text{classical spin unit vector at } i) \times (\text{magnon weight function at } i)]. \tag{2.24}$$

(See Fig. 2.5). Note that the total weight does not have to be 1 due to the paraunitarity of $\hat{Q}$[6].

[4] $|0\rangle$ does not have to be the classical ground state, which corresponds to the Fock vacuum of $(a, a^\dagger)$. In this sense, $|0\rangle$ includes the quantum correction to the classical ground state.

[5] In the case of the simple Heisenberg ferromagnet with $\boldsymbol{M}^z_i = \hat{z}$ (no sublattice), $\boldsymbol{S}_{\boldsymbol{k},\alpha}$ becomes $-\hat{z}$, which is a constant function of $\boldsymbol{k}$.

[6] In simple cases such as the Heisenberg ferromagnet, $\hat{Q}$ becomes a unitary matrix. In that case, the total weight should be 1.

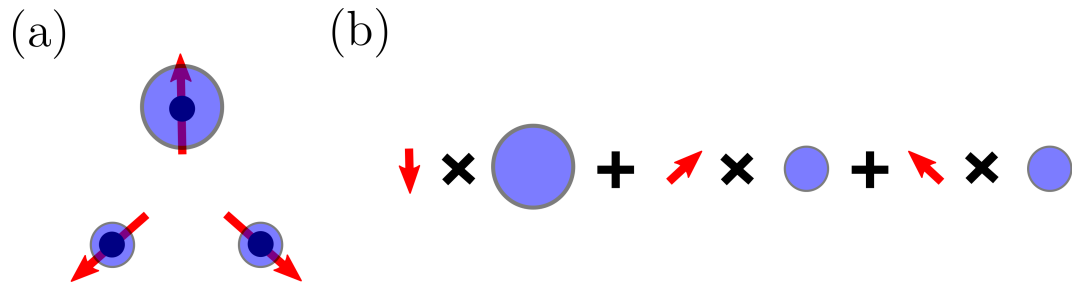

Figure 2.5: Schematic pictures of (a) magnon weight function in a unit cell and (b) magnon spin.

2.4 No-go conditions

In non-interacting electron systems, spin-momentum locking is forbidden for Hamiltonians with rotational symmetries. In $SO(3)$ rotational symmetric systems, we cannot define the spin-momentum locking due to the electron spin degeneracy. In $U(1)$ symmetric systems, all Bloch states in the Brillouin zone have the common quantized axis, and electron spin does not depend on momentum.

Usually, spin-momentum locking is discussed for the Hamiltonians without spin-rotational symmetries. Such discussions can also be applied to the magnon spin-momentum locking. However, there is an additional factor for magnonic systems. In the case of magnonic systems, the notion of spontaneous symmetry breaking, where symmetries of ground states are lower than those of the Hamiltonians, changes the story. If the magnon states break rotational symmetries **completely**, the magnon spin can depend on the momentum.

In this section, we prove that the magnon spin-momentum locking does not occur in collinear magnets (except for a *trivial* spin-momentum locking discussed in 2.4.3). In the next section and Chap. 3, we discuss and investigate the magnon spin-momentum locking in noncollinear and noncoplanar antiferromagnets, where rotational symmetries are completely broken in the ground and one-magnon states.

2.4.1 $SO(3) \to U(1)$ symmetry breaking case

We here prove that there is no magnon spin-momentum locking in the presence of a symmetry breaking $SO(3) \to U(1)$. To prove it, we first prove that all one-magnon states are eigenstates of $S^z_{\rm tot}$, where $S^z_{\rm tot}$ is the unbroken generator

[7], or equivalently,

$$S^z_{\rm tot}|0\rangle \propto |0\rangle, \tag{2.25}$$

By using Eq. (2.25) and $[H, S^z_{\rm tot}] = 0$, we obtain the following bosonic representation of $S^z_{\rm tot}$ up to the second order of $(b, b^\dagger)$[8]:

$$S^z_{\rm tot} = (Const.) + \sum_{\boldsymbol{k},\alpha} S^z_{\boldsymbol{k},\alpha} b^\dagger_{\boldsymbol{k},\alpha} b_{\boldsymbol{k},\alpha}, \tag{2.26}$$

where $S^z_{\boldsymbol{k},\alpha}$ is the same one as Eq. (2.23). Thus, a one-magnon state $|\boldsymbol{k},\alpha\rangle$ are eigenstates of the unbroken generator $S^z_{\rm tot}$:

$$\begin{aligned} S^z_{\rm tot}|\boldsymbol{k},\alpha\rangle &= \left[(Const.) + \sum_{\boldsymbol{k'},\beta} S^z_{\boldsymbol{k'},\beta} b^\dagger_{\boldsymbol{k'},\beta} b_{\boldsymbol{k'},\beta}\right] b^\dagger_{\boldsymbol{k},\alpha}|0\rangle \\ &\propto b^\dagger_{\boldsymbol{k},\alpha}|0\rangle. \end{aligned} \tag{2.27}$$

It is important to note that all one-magnon states have the common quantized axis (z axis). Using the notation $|\boldsymbol{k}, M\rangle$ that is an eigenstate of $S^z_{\rm tot}$ with an eigenvalue M instead of $|\boldsymbol{k},\alpha\rangle$, we obtain

$$\begin{aligned} &\langle \boldsymbol{k}, M|S^z_{\rm tot}|\boldsymbol{k}, M\rangle = M, \\ &\langle \boldsymbol{k}, M|S^{x(,y)}_{\rm tot}|\boldsymbol{k}, M\rangle = \pm 1/i\langle \boldsymbol{k}, M|[S^{y(,x)}_{\rm tot}, S^z_{\rm tot}]|\boldsymbol{k}, M\rangle = 0, \end{aligned} \tag{2.28}$$

where we have used $[S^a_{\rm tot}, S^b_{\rm tot}] = i\epsilon_{abc} S^c_{\rm tot}$. Equation (2.28) shows that

$$\boldsymbol{S}_{\boldsymbol{k},M} = \langle \boldsymbol{k}, M|S^z_{\rm tot}|\boldsymbol{k}, M\rangle - \langle 0|S^z_{\rm tot}|0\rangle = (0, 0, M) - \boldsymbol{M}_0, \tag{2.29}$$

where $\boldsymbol{M}_0$ is the quantized magnetization of the ground state, takes quantized values. Because quantized spin components cannot be changed under a small momentum change $\boldsymbol{k} \to \boldsymbol{k} + \delta\boldsymbol{k}$, the magnon spin $\boldsymbol{S}_{\boldsymbol{k},\alpha}$ is a constant function of $\boldsymbol{k}$.

[7] The statement "the fact that $|0\rangle$ is an eigenstate of $S^z_{\rm tot}$ means that excited states are also eigenstates of it" does not always hold. Since the Hamiltonian itself has $SO(3)$ symmetry, general eigenstates of the Hamiltonian can take general quantized axes. We should check that the statement holds for one-magnon states.

[8] In order to satisfy Eq. (2.25), $S^z_{\rm tot}$ cannot contain $b^\dagger, b^\dagger b^\dagger$ terms. Since $S^z_{\rm tot}$ is a Hermitian operator, b, bb terms cannot also be included. For one-magnon states $|\boldsymbol{k},\alpha\rangle$ and $|\boldsymbol{k},\beta\rangle$, the following relation holds:

$$0 = \langle \boldsymbol{k},\alpha|[H, S^z_{\rm tot}]|\boldsymbol{k},\beta\rangle = (E_{\boldsymbol{k},\alpha} - E_{\boldsymbol{k},\beta})\langle \boldsymbol{k},\alpha|S^z_{\rm tot}|\boldsymbol{k},\beta\rangle.$$

For the systems without degeneracy ($E_{\boldsymbol{k},\alpha} \neq E_{\boldsymbol{k},\beta}$), this equation means that the matrix element $\langle \boldsymbol{k},\alpha|S^z_{\rm tot}|\boldsymbol{k},\beta\rangle$ should be diagonal. Even in the presence of the degeneracy, we can always choose the basis to diagonalize $\langle \boldsymbol{k},\alpha|S^z_{\rm tot}|\boldsymbol{k},\beta\rangle$ by a proper unitary transformation.

2.4.2 $U(1) \to U(1)$ case

Next, we consider the Hamiltonians with the $U(1)$-rotational symmetry around the z axis such as XY models. When there is no symmetry breaking, $S^z_{\rm tot}$ is given by Eq. (2.26). Thus, $|\boldsymbol{k}, \alpha\rangle$ is an eigenstate of $S^z_{\rm tot}$, and we cannot expect the magnon spin-momentum locking.

2.4.3 *Trivial* spin-momentum locking

As we have shown, all one-magnon states have the common quantized axis for collinear magnets with $U(1)$ symmetric ground states. In the above discussions, we implicitly assume that magnon spin is a smooth function of momentum. However, when we cannot avoid a singularity such as a band crossing point in a one-dimensional system in the adiabatic deformation $\boldsymbol{k} \to \boldsymbol{k'}$, $S^a_{\boldsymbol{k},\alpha}$ can be changed across the singular region. Suppose that two magnon bands with $S^z_{\boldsymbol{k},\alpha} = \pm 1$ in a one-dimensional system have a crossing point at $k = k_0$. If the upper- (lower-)band magnon spin is $+1$ (-1) at $k = k_0 - \delta k$, the upper-(lower-)band magnon spin is -1 $(+1)$ at $k = k_0 + \delta k$. In the following, we regard such a case as *trivial* spin-momentum locking because the magnon spin depends on momentum if we focus only on the upper- (lower-)band. We construct an example of *trivial* spin-momentum locking in Chap. 3.

2.5 Spin-momentum locking induced by symmetry breaking

In the previous section, we show that spin-momentum locking does not occur for $SO(3) \to U(1)$ and $U(1) \to U(1)$ cases except for *trivial* spin-momentum locking. In such systems, there is one unbroken rotational axis, and magnon spin is a good quantum number of the magnon bands. Such systems correspond to collinear magnets such as ferromagnets, ferrimagnets, and usual antiferromagnets.

To realize the spin-momentum locking for spin rotational symmetric Hamiltonians, we should consider the ground state without any spin rotational symmetry, i.e., the noncollinear and noncoplanar structures. This can be understood by considering the spontaneous symmetry breaking: $SO(3) \to \{e\}$ or $U(1) \to \{e\}$, where e is the identity element. Since there is no unbroken generator, we can expect the magnon spin.

Note that noncollinearity and noncoplanarity are just necessary conditions. Consider the antiferromagnetic Heisenberg model defined on a triangular lattice.

Table 2.1: Relation between symmetries and the possibility of magnon spin-momentum locking.

Hamiltonian	Ground state	Spin-momentum locking
No symmetry	Noncollinear or Noncoplanar	Possible
$SO(3)$ symmetry	Collinear ($U(1)$ symmetry)	Only *trivial* case
$U(1)$ symmetry	Collinear ($U(1)$ symmetry)	Only *trivial* case
$SO(3)$ symmetry	Noncollinear or Noncoplanar	Possible
$U(1)$ symmetry	Noncollinear or Noncoplanar	Possible

One of the classical ground states is the 120° structure. For this case, the system can be described by a bosonic Hamiltonian without sublattice degrees of freedom. In our formalism, this corresponds to the fact that spins on different magnetic sublattices contribute to $\boldsymbol{S}_{\boldsymbol{k},\alpha}$ with the equal weight. Thus, we obtain

$$\boldsymbol{S}_{\boldsymbol{k},\alpha} \propto -\sum_i \boldsymbol{M}_i^z = 0, \tag{2.30}$$

where we have used $\sum_i \boldsymbol{M}_i^z = 0$ for the 120° structure.

2.6 Discussion and Summary

In this chapter, we have discussed the properties of the magnon spin-momentum locking for general magnets in the context of the spin-wave theory. We have ignored the effect of magnon-magnon interactions by considering $S_0 \gg 1$ limit. It would be an interesting future work to include such interactions for $S_0 \sim 1$ systems such as nonperturbative damping discussed in Ref. [55].

Another remaining issue is giving the sufficient conditions for the magnon spin-momentum locking. Unfortunately, what we did in this chapter is just giving no-go conditions. As we have shown, the magnon spin-momentum locking does not occur in the Heisenberg antiferromagnet on the triangular lattice, which is one of the most typical examples of noncollinear magnets. Since giving the sufficient conditions is useful for exploring candidates of the magnon spin-momentum locking, it would be another interesting future work.

In summary, we formulated the magnon spin-momentum locking. We defined the magnon spin for general spin Hamiltonians with ordered classical ground states in the semiclassical level. By considering the bosonic representation of the total spin operator, we gave no-go conditions for magnon spin to be independent of momentum. By avoiding such conditions, we discussed the possibility for magnon spin-momentum locking for given symmetries. We found that there are

several types of magnon spin-momentum locking [Table. 2.1]. It is important to note that the magnon spin-momentum locking can occur even for the Hamiltonians with spin rotational symmetries. The spontaneous symmetry breaking is a new factor of the spin-momentum locking.

Chapter 3

Magnon spin-momentum locking: examples

In this chapter, we explicitly construct examples of the magnon spin-momentum locking. We first explain the technical details of the magnon eigenenergy problem and the definition of the winding number around the vortex. Then we construct the one- and two-dimensional examples of *trivial* and *nontrivial* spin-momentum lockings, respectively. We also discuss a candidate material and possibilities of experimental detections.

3.1 Method and definition

In the previous chapter, we have introduced the bosonic Bogoliubov-de Gennes (BdG) Hamiltonian and Bogouliubov transformation. We here give an explicit procedure to obtain the Hamiltonian, magnon eigenvalues, and a paraunitary matrix $\hat{Q}$ for general two-body spin Hamiltonian.

3.1.1 Magnon Hamiltonian

In the following, we derive the explicit form of the bosonic BdG Hamiltonian based on the methods in Ref. [56]. Again, the bosonic BdG Hamiltonian for the general two-body spin Hamiltonian is given by

$$H = \frac{1}{2} \sum_{\boldsymbol{R},\boldsymbol{R'}} \sum_{i,j=1}^{N} \sum_{a,b} J_{ij}^{ab}(\boldsymbol{R},\boldsymbol{R'}) S_{\boldsymbol{R},i}^{a} S_{\boldsymbol{R'},j}^{b}, \tag{3.1}$$

where notations are the same as those in Chap. 2. For convenience, we rewrite Eq. (3.1) in terms of the local rotating frame

$$\boldsymbol{M}_i^a = R(\theta_i, \phi_i)\hat{a}, \tag{3.2}$$

where $\hat{a} = \hat{x}, \hat{y}, \hat{z}$ are the usual Cartesian unit vectors, and $R(\theta_i, \phi_i)$ is the rotation matrix defined at a magnetic sublattice i. The explicit form of $R(\theta, \phi)$ is given by

$$\begin{aligned} R(\theta,\phi) &= R_2 R_1, \\ R_1 &= \begin{pmatrix} \cos\phi & -\sin\phi & 0 \\ \sin\phi & \cos\phi & 0 \\ 0 & 0 & 1 \end{pmatrix}, \\ R_2 &= \begin{pmatrix} \cos\theta\cos^2\phi + \sin^2\phi & \cos\phi\sin\phi(\cos\theta - 1) & \sin\theta\cos\phi \\ \cos\phi\sin\phi(\cos\theta - 1) & \cos\theta\sin^2\phi + \cos^2\phi & \sin\theta\sin\phi \\ -\sin\theta\cos\phi & -\sin\theta\sin\phi & \cos\theta \end{pmatrix}. \end{aligned} \tag{3.3}$$

Substituting Eq. (3.2) into Eq. (3.1), we obtain the spin Hamiltonian in terms of the rotating-frame spin operators:

$$H = \frac{1}{2}\sum_{\boldsymbol{R},\boldsymbol{R'}}\sum_{i,j=1}^{N}\sum_{l,m}\mathcal{J}_{ij}^{lm}(\boldsymbol{R},\boldsymbol{R'})\tilde{S}_{\boldsymbol{R},i}^{l}\tilde{S}_{\boldsymbol{R'},j}^{m}, \tag{3.4}$$

where

$$\mathcal{J}_{ij}^{lm}(\boldsymbol{R},\boldsymbol{R'}) = \sum_{a,b} J_{ij}^{ab}(\boldsymbol{R},\boldsymbol{R'})[\boldsymbol{M}_i^l \cdot \hat{a}][\boldsymbol{M}_j^m \cdot \hat{b}]. \tag{3.5}$$

Using the periodicity of the magnetic lattice, we Fourier transform the spin operators:

$$\tilde{S}_{\boldsymbol{R},i}^{l} = \frac{1}{\sqrt{L^3}}\sum_{\boldsymbol{k}}\tilde{S}_{\boldsymbol{k},i}^{l}\exp[i\boldsymbol{k}\cdot(\boldsymbol{R}+\boldsymbol{r}_i)], \tag{3.6}$$

where $\boldsymbol{r}_i$ is the relative position of the sublattice i at a magnetic unit cell, and L is the size of the system. Using this notation and $\mathcal{J}_{ij}^{lm}(\boldsymbol{R},\boldsymbol{R'}) = \mathcal{J}_{ij}^{lm}(\boldsymbol{R'}-\boldsymbol{R})$, we obtain

$$H = \frac{1}{2}\sum_{\boldsymbol{k}}\sum_{i,j=1}^{N}\sum_{l,m}\tilde{S}_{\boldsymbol{k},i}^{l}\mathcal{J}_{ij}^{lm}(\boldsymbol{k})\tilde{S}_{-\boldsymbol{k},j}^{m}, \tag{3.7}$$

where

$$\mathcal{J}_{ij}^{lm}(\boldsymbol{k}) = \sum_{\boldsymbol{R}'-\boldsymbol{R}} \mathcal{J}_{ij}^{lm}(\boldsymbol{R}'-\boldsymbol{R}) \exp[-i\boldsymbol{k}\cdot(\boldsymbol{R}'-\boldsymbol{R}+\boldsymbol{r}_j-\boldsymbol{r}_i)]. \tag{3.8}$$

Now we introduce the Holstein-Primakoff transformation in the spin-wave aprroximation

$$\begin{aligned}
\tilde{S}_{\boldsymbol{k},i}^{x} &= \sqrt{\frac{S_0}{2}}[a_{\boldsymbol{k},i}^{\dagger} + a_{-\boldsymbol{k},i}] + \mathcal{O}\left(\frac{1}{S_0^2}\right), \\
\tilde{S}_{\boldsymbol{k},i}^{y} &= \sqrt{\frac{S_0}{2}}[a_{\boldsymbol{k},i}^{\dagger} - a_{-\boldsymbol{k},i}] + \mathcal{O}\left(\frac{1}{S_0^2}\right), \\
\tilde{S}_{\boldsymbol{k},i}^{z} &= \sqrt{L^3} S_0 \delta_{\boldsymbol{k},0} \exp[-i\boldsymbol{k}\cdot\boldsymbol{r}_\alpha] - \frac{1}{\sqrt{L^3}} \sum_{\boldsymbol{k}'} a_{\boldsymbol{k}',i}^{\dagger} a_{\boldsymbol{k}'-\boldsymbol{k},i},
\end{aligned} \tag{3.9}$$

where the Holstein-Primakoff bosons satisfy $[a_{\boldsymbol{k},i}, a_{\boldsymbol{k}',j}^{\dagger}] = \delta_{ij}\delta_{\boldsymbol{k}\boldsymbol{k}'}$. Substituting Eqs. (3.9) into Eq. (3.7), we obtain

$$H = H_0 + H_1 + H_2, \tag{3.10}$$

where

$$\begin{aligned}
H_0 &= \frac{1}{2} L^3 S_0(S_0+1) \sum_{i,j} \mathcal{J}_{ij}^{zz}(\boldsymbol{k}=0), \\
H_1 &= S_0 \frac{L^3 S_0}{2} \sum_{i,j} [F_{i,j} a_{\boldsymbol{k}=0,i}^{\dagger} + F_{i,j}^{*} a_{\boldsymbol{k}=0,i}], \\
H_2 &= \frac{1}{2} S_0 \sum_{i,j} \sum_{\boldsymbol{k}} [A_{i,j}(\boldsymbol{k}) a_{\boldsymbol{k},i}^{\dagger} a_{\boldsymbol{k},j} + B_{i,j}(\boldsymbol{k}) a_{\boldsymbol{k},i}^{\dagger} a_{-\boldsymbol{k},j}^{\dagger}, \\
&\quad + B_{i,j}^{*}(-\boldsymbol{k}) a_{-\boldsymbol{k},i} a_{\boldsymbol{k},j} + A_{i,j}^{*}(-\boldsymbol{k}) a_{-\boldsymbol{k},i} a_{-\boldsymbol{k},j}^{\dagger}]
\end{aligned} \tag{3.11}$$

and

$$\begin{aligned}
F_{ij} &= \mathcal{J}_{ij}^{xz}(\boldsymbol{k}=0) + i\mathcal{J}_{ij}^{yz}(\boldsymbol{k}=0), \\
A_{ij}(\boldsymbol{k}) &= \frac{1}{2}[\mathcal{J}_{ij}^{xx}(\boldsymbol{k}) + \mathcal{J}_{ij}^{yy}(\boldsymbol{k}) - i(\mathcal{J}_{xy}^{xy}(\boldsymbol{k}) - \mathcal{J}_{ij}^{yx}(\boldsymbol{k}))] - \sum_{k} \mathcal{J}_{ik}^{zz}(\boldsymbol{k}=0)\delta_{ij}, \\
B_{ij}(\boldsymbol{k}) &= \frac{1}{2}[\mathcal{J}_{ij}^{xx}(\boldsymbol{k}) - \mathcal{J}_{ij}^{yy}(\boldsymbol{k}) + i(\mathcal{J}_{xy}^{xy}(\boldsymbol{k}) + \mathcal{J}_{ij}^{yx}(\boldsymbol{k}))].
\end{aligned} \tag{3.12}$$

Note that H_1 vanishes for the appropriate choice of the classical ground state since the presence of H_1 leads to an instability of the ground state in equilibrium. H_0 describes the constant energy shift, while H_2 corresponds to the bosonic BdG Hamiltonian discussed in Chap. 2.

3.1.2 Magnon eigenenergy problem

In Chap. 2, we have introduced the bosonic BdG Hamiltonian. As we have shown, we cannot use the diagonalization to obtain eigenvalues of the system with off-diagonal terms such as aa or $a^\dagger a^\dagger$. Instead of the usual diagonalization method, we perform the bosonic Bogoliubov transformation with paraunitary matrices $\hat{Q}, \hat{Q}^\dagger$.

In the following, we describe a procedure to obtain such paraunitary matrices. The general form of the bosonic BdG Hamiltonian is given by

$$\hat{\mathcal{H}}_{\boldsymbol{k}} = \begin{pmatrix} \hat{A}_{\boldsymbol{k}} & \hat{B}_{\boldsymbol{k}} \\ \hat{B}^*_{-\boldsymbol{k}} & \hat{A}^*_{-\boldsymbol{k}} \end{pmatrix}, \tag{3.13}$$

where $\hat{A}$ is a $N \times N$ Hermitian matrix and $\hat{B}$ a $N \times N$ matrix.

In addition, we should impose another condition for the Hamiltonian (3.13). Since it describes the excited states, the eigenenergies should be positive[1]. This condition is equivalent to the positive definiteness of the Hamiltonian (3.13).

Proof. Suppose that we obtain the paraunitary matrices $\hat{Q}, \hat{Q}^\dagger$ satisfying

$$\hat{Q}^\dagger_{\boldsymbol{k}} \hat{\mathcal{H}}_{\boldsymbol{k}} \hat{Q}_{\boldsymbol{k}} = \begin{pmatrix} \hat{E}_{\boldsymbol{k}} & 0 \\ 0 & \hat{E}_{-\boldsymbol{k}} \end{pmatrix}, \tag{3.14}$$

where $\hat{E}_{\boldsymbol{k}} = \mathrm{diag}(E_{\boldsymbol{k},1}, \cdots, E_{\boldsymbol{k},\alpha}, \cdots, E_{\boldsymbol{k},N})$. According to the Sylvester's law of inertia, the numbers of positive and negative elements of the diagonal matrix

$$\hat{D} = \hat{S}^\dagger \hat{H} \hat{S}, \tag{3.15}$$

where $\hat{S}$ is a regular matrix and $\hat{H}$ a Hermitian matrix, does not depend on the choice of $\hat{S}$. Suppose that the right-hand side of Eq. (3.14) is a diagonal matrix whose elements are positive, or equivalently, the magnon eigenenergies are positive. Using the the Sylvester's law of interia, all elements of the diagonal matrix

$$\hat{D}_{\boldsymbol{k}} = \hat{U}^\dagger_{\boldsymbol{k}} \hat{\mathcal{H}}_{\boldsymbol{k}} \hat{U}_{\boldsymbol{k}} = \hat{U}^{-1}_{\boldsymbol{k}} \hat{\mathcal{H}}_{\boldsymbol{k}} \hat{U}_{\boldsymbol{k}}, \tag{3.16}$$

where $\hat{U}$ is a unitary matrix, are positive. Because Eq. (3.16) is the definition of the diagonalization, the positiveness of the magnon energies is equivalent to the positive definiteness of $\hat{\mathcal{H}}_{\boldsymbol{k}}$. □

[1]Strictly speaking, the eigenenergies of the Nambu-Goldstone modes are zero in the thermodynamic limit. We here consider the systems without zero modes or $\boldsymbol{k} \neq 0$ case

In the following, we assume that $\hat{\mathcal{H}}_{\boldsymbol{k}}$ is positive definite and describe the method used in Ref. [36, 57]. The orthogonality condition in which the magnon operators $(b, b^\dagger)$ satisfy the commutation relation, is given by

$$\hat{Q}_{\boldsymbol{k}}^\dagger \hat{\Sigma}_3 \hat{Q}_{\boldsymbol{k}} = \hat{Q}_{\boldsymbol{k}} \hat{\Sigma}_3 \hat{Q}_{\boldsymbol{k}}^\dagger = \hat{\Sigma}_3, \tag{3.17}$$

where $[\hat{\Sigma}_3]_{i,j} = \delta_{ij}\sigma_j$ with $\sigma_j = +1$ for $j = 1, \cdots, N$ and $\sigma_j = -1$ for $j = N+1, \cdots, 2N$. All we have to do is determine $\hat{Q}, \hat{Q}^\dagger$ satisfying Eqs. (3.14) and (3.17). We here explain the method using the Cholesky decomposition.

For positive definite Hermitian matrix $\hat{\mathcal{H}}_{\boldsymbol{k}}$, we can perform the Cholesky decomposition

$$\hat{\mathcal{H}}_{\boldsymbol{k}} = \hat{K}_{\boldsymbol{k}}^\dagger \hat{K}_{\boldsymbol{k}}, \tag{3.18}$$

where $\hat{K}_{\boldsymbol{k}}$ is an upper triangle matrix. Using $\hat{K}_{\boldsymbol{k}}$ and $\hat{K}_{\boldsymbol{k}}^\dagger$, we define a unitary matrix

$$\hat{U}_{\boldsymbol{k}} \equiv \hat{K}_{\boldsymbol{k}} \hat{Q}_{\boldsymbol{k}} \begin{pmatrix} \hat{E}_{\boldsymbol{k}}^{-\frac{1}{2}} & 0 \\ 0 & \hat{E}_{-\boldsymbol{k}}^{-\frac{1}{2}} \end{pmatrix} \tag{3.19}$$

and the dual Hamiltonian

$$\hat{\mathcal{H}}'_{\boldsymbol{k}} \equiv \hat{K}_{\boldsymbol{k}} \hat{\Sigma}_3 \hat{K}_{\boldsymbol{k}}^\dagger, \tag{3.20}$$

which is a Hermitian matrix. Here the unitarity of $\hat{U}_{\boldsymbol{k}}$ can be checked as follows:

$$\begin{aligned}
\hat{U}_{\boldsymbol{k}}^\dagger \hat{U}_{\boldsymbol{k}} &= \begin{pmatrix} \hat{E}_{\boldsymbol{k}}^{-\frac{1}{2}} & 0 \\ 0 & \hat{E}_{-\boldsymbol{k}}^{-\frac{1}{2}} \end{pmatrix} \hat{Q}_{\boldsymbol{k}}^\dagger \hat{K}_{\boldsymbol{k}}^\dagger \hat{K}_{\boldsymbol{k}} \hat{Q}_{\boldsymbol{k}} \begin{pmatrix} \hat{E}_{\boldsymbol{k}}^{-\frac{1}{2}} & 0 \\ 0 & \hat{E}_{-\boldsymbol{k}}^{-\frac{1}{2}} \end{pmatrix} \\
&= \begin{pmatrix} \hat{E}_{\boldsymbol{k}}^{-\frac{1}{2}} & 0 \\ 0 & \hat{E}_{-\boldsymbol{k}}^{-\frac{1}{2}} \end{pmatrix} \hat{Q}_{\boldsymbol{k}}^\dagger \hat{\mathcal{H}}_{\boldsymbol{k}} \hat{Q}_{\boldsymbol{k}} \begin{pmatrix} \hat{E}_{\boldsymbol{k}}^{-\frac{1}{2}} & 0 \\ 0 & \hat{E}_{-\boldsymbol{k}}^{-\frac{1}{2}} \end{pmatrix} \\
&= \begin{pmatrix} \hat{E}_{\boldsymbol{k}}^{-\frac{1}{2}} & 0 \\ 0 & \hat{E}_{-\boldsymbol{k}}^{-\frac{1}{2}} \end{pmatrix} \begin{pmatrix} \hat{E}_{\boldsymbol{k}} & 0 \\ 0 & \hat{E}_{-\boldsymbol{k}} \end{pmatrix} \begin{pmatrix} \hat{E}_{\boldsymbol{k}}^{-\frac{1}{2}} & 0 \\ 0 & \hat{E}_{-\boldsymbol{k}}^{-\frac{1}{2}} \end{pmatrix} \\
&= \hat{1}.
\end{aligned} \tag{3.21}$$

Actually, this unitary matrix diagonalizes the Hermitian matrix (3.20):

$$\begin{aligned}
\hat{U}_{\boldsymbol{k}}^{\dagger}\hat{\mathcal{H}'}_{\boldsymbol{k}}\hat{U}_{\boldsymbol{k}} &= \begin{pmatrix} \hat{E}_{\boldsymbol{k}}^{-\frac{1}{2}} & 0 \\ 0 & \hat{E}_{-\boldsymbol{k}}^{-\frac{1}{2}} \end{pmatrix} \hat{Q}_{\boldsymbol{k}}^{\dagger}\hat{K}_{\boldsymbol{k}}^{\dagger}\hat{K}_{\boldsymbol{k}}\hat{\Sigma}_3\hat{K}_{\boldsymbol{k}}^{\dagger}\hat{K}_{\boldsymbol{k}}\hat{Q}_{\boldsymbol{k}} \begin{pmatrix} \hat{E}_{\boldsymbol{k}}^{-\frac{1}{2}} & 0 \\ 0 & \hat{E}_{-\boldsymbol{k}}^{-\frac{1}{2}} \end{pmatrix} \\
&= \begin{pmatrix} \hat{E}_{\boldsymbol{k}}^{-\frac{1}{2}} & 0 \\ 0 & \hat{E}_{-\boldsymbol{k}}^{-\frac{1}{2}} \end{pmatrix} \hat{Q}_{\boldsymbol{k}}^{\dagger}\hat{K}_{\boldsymbol{k}}^{\dagger}\hat{K}_{\boldsymbol{k}}\hat{Q}_{\boldsymbol{k}}\hat{Q}_{\boldsymbol{k}}^{-1}\hat{\Sigma}_3(\hat{Q}_{\boldsymbol{k}}^{\dagger})^{-1}\hat{Q}_{\boldsymbol{k}}^{\dagger}\hat{K}_{\boldsymbol{k}}^{\dagger}\hat{K}_{\boldsymbol{k}}\hat{Q}_{\boldsymbol{k}} \begin{pmatrix} \hat{E}_{\boldsymbol{k}}^{-\frac{1}{2}} & 0 \\ 0 & \hat{E}_{-\boldsymbol{k}}^{-\frac{1}{2}} \end{pmatrix} \\
&= \begin{pmatrix} \hat{E}_{\boldsymbol{k}}^{-\frac{1}{2}} & 0 \\ 0 & \hat{E}_{-\boldsymbol{k}}^{-\frac{1}{2}} \end{pmatrix} \hat{Q}_{\boldsymbol{k}}^{\dagger}\hat{\mathcal{H}}_{\boldsymbol{k}}\hat{Q}_{\boldsymbol{k}}\hat{Q}_{\boldsymbol{k}}^{-1}\hat{\Sigma}_3(\hat{Q}_{\boldsymbol{k}}^{\dagger})^{-1}\hat{Q}_{\boldsymbol{k}}^{\dagger}\hat{\mathcal{H}}_{\boldsymbol{k}}\hat{Q}_{\boldsymbol{k}} \begin{pmatrix} \hat{E}_{\boldsymbol{k}}^{-\frac{1}{2}} & 0 \\ 0 & \hat{E}_{-\boldsymbol{k}}^{-\frac{1}{2}} \end{pmatrix} \\
&= \begin{pmatrix} \hat{E}_{\boldsymbol{k}}^{-\frac{1}{2}} & 0 \\ 0 & \hat{E}_{-\boldsymbol{k}}^{-\frac{1}{2}} \end{pmatrix} \begin{pmatrix} \hat{E}_{\boldsymbol{k}} & 0 \\ 0 & \hat{E}_{-\boldsymbol{k}} \end{pmatrix} \begin{pmatrix} 1 & 0 \\ 0 & -1 \end{pmatrix} \begin{pmatrix} \hat{E}_{\boldsymbol{k}} & 0 \\ 0 & \hat{E}_{-\boldsymbol{k}} \end{pmatrix} \begin{pmatrix} \hat{E}_{\boldsymbol{k}}^{-\frac{1}{2}} & 0 \\ 0 & \hat{E}_{-\boldsymbol{k}}^{-\frac{1}{2}} \end{pmatrix} \\
&= \begin{pmatrix} \hat{E}_{\boldsymbol{k}} & 0 \\ 0 & -\hat{E}_{-\boldsymbol{k}} \end{pmatrix}. \qquad (3.22)
\end{aligned}$$

Thus, we can obtain the magnon eigenvalues by diagonalizing the Hermitian matrix (3.20). After determining $\hat{E}_{\boldsymbol{k}}$ and $\hat{E}_{-\boldsymbol{k}}$ by the diagonalization, we can determine the paraunitary matrices as

$$\hat{Q}_{\boldsymbol{k}} \equiv \hat{K}_{\boldsymbol{k}}^{-1}\hat{U}_{\boldsymbol{k}} \begin{pmatrix} \hat{E}_{\boldsymbol{k}}^{\frac{1}{2}} & 0 \\ 0 & \hat{E}_{-\boldsymbol{k}}^{\frac{1}{2}} \end{pmatrix}. \qquad (3.23)$$

We summarize the procedure to obtain the magnon eigenenergies and paraunitary matrix $\hat{Q}_{\boldsymbol{k}}$ from a general two-body spin Hamiltonian in Fig. 3.1

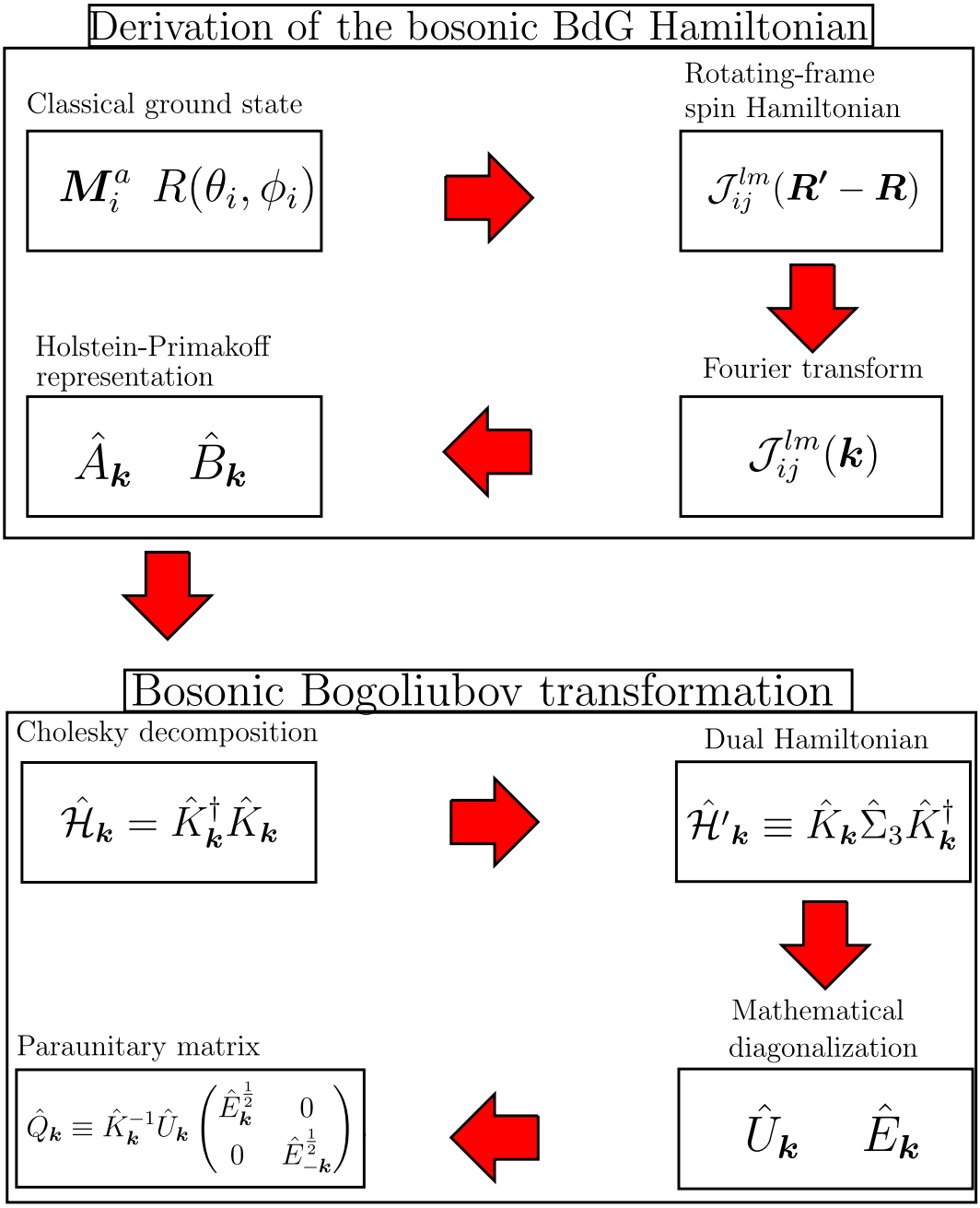

Figure 3.1: Procedure to obtain the magnon eigenenergies and paraunitary matrix $\hat{Q}_{\boldsymbol{k}}$.

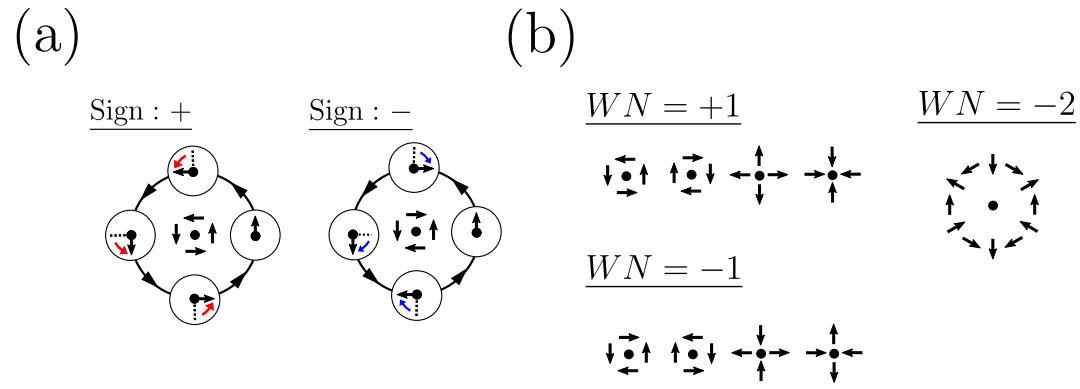

Figure 3.2: Schematic pictures of (a) the definition of the sign of winding numbers and (b) examples for some winding numbers.

3.1.3 Winding number in two dimensions

In the two-dimensional examples constructed in the following chapters, there are various spin vortices. Although it is not a mathematically rigorous definition, we would like to give the intuitive meaning of the winding number around a vortex-like structure[2] [Fig. 3.2 (a)]. Let $\boldsymbol{v}(\boldsymbol{x})$ be a vector field with an isolated zero $\boldsymbol{x}_0$. The winding number is the total number of counterclockwise turns experienced by $\boldsymbol{v}(\boldsymbol{x})$ after completing the counterclockwise motion along the closed curve γ around $\boldsymbol{x}_0$. The positive winding number means the counterclockwise turns of $\boldsymbol{v}(\boldsymbol{x})$ and conversely, negative winding number means the clockwise turns. The winding number can be calculated by the formula

$$Q = 1/(2\pi) \oint_\gamma ds(\boldsymbol{n} \times \partial_s \boldsymbol{n})_z, \tag{3.24}$$

where $\boldsymbol{n} = \boldsymbol{v}_\parallel/|\boldsymbol{v}_\parallel|$, and $\boldsymbol{v}_\parallel$ is the in-plane projection of $\boldsymbol{v}$. Some examples of spin vortices with various winding numbers are drawn in Fig. 3.2 (b). It is important to note that the notion of winding number in two dimensions is different from the chirality. Let us look at the first and second examples with winding number $+1$ in Fig. 3.2 (b). The first one is a left-handed vortex, while the second one is a right handed vortex. In this sense, the chirality and winding number are different notions.

[2]Strictly speaking, the definition here is for the degree of map in mathematics. Although it is not the winding number in mathematics, it is sometimes mentioned as the winding number in theoretical physics.

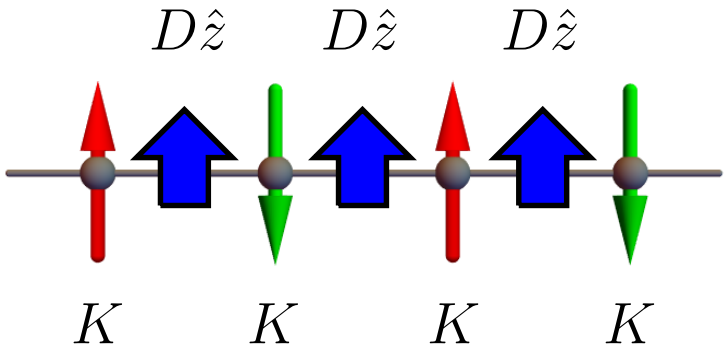

Figure 3.3: Schematic picture of one-dimensional antiferromagnet described by the Hamiltonian (3.25).

3.2 *Trivial* magnon spin-momentum locking

We here construct a model of the *trivial* magnon spin-momentum locking, which occurs in magnets with $U(1)$ symmetric ground states, discussed in Chap. 2.

3.2.1 Model

We consider an antiferromagnetic Hamiltonian, which has been studied in the context of the spin wave field effect transistor [31]

$$H^{1D} = \sum_{\langle i,j \rangle} [J\boldsymbol{S}_i \cdot \boldsymbol{S}_j + D\hat{z} \cdot (\boldsymbol{S}_i \times \boldsymbol{S}_j)] + K \sum_i S_{i,z}^2, \tag{3.25}$$

where $J > 0$ is the nearest-neighbor exchange coupling, D is the strength of the Dzyaloshinskii-Moriya (DM) interaction, and $K < 0$ is the easy-axis anisotropy. Although the DM interaction and the anisotropy breaks the $SO(3)$ symmetry, they preserve the $U(1)$ symmetry around the z axis.

3.2.2 Magnon dispersion

For sufficiently small D, the classical ground state is the Néel state with two sublattices, A with up spin and B with down spin [Fig. 3.3]. Thus, both of the symmetries of the spin Hamiltonian and classical ground states are described by $U(1)$. Using the Holstein-Primakoff transformation around the Néel state,

$$\begin{aligned} S_{R,A}^{\pm} &= \sqrt{2S_0}a_{R,A}^{(\dagger)}, S_{R,A}^z = S_0 - a_{R,A}^\dagger a_{R,A}, \\ S_{R,B}^{\mp} &= \sqrt{2S_0}a_{R,B}^{(\dagger)}, S_{R,B}^z = a_{R,B}^\dagger a_{R,B} - S_0, \end{aligned} \tag{3.26}$$

we can rewrite Eq. (3.25) in terms of magnons as

$$H^{1D} = \frac{1}{2}\sum_k \Psi_k^\dagger \begin{pmatrix} X(k) & 0 & 0 & Y_-(k) \\ 0 & X(k) & Y_+(k) & 0 \\ 0 & Y_+(k) & X(k) & 0 \\ Y_-(k) & 0 & 0 & X(k) \end{pmatrix} \Psi_k, \tag{3.27}$$

where k is the one-dimensional momentum, $\Psi_k^\dagger = (a_{k,A}^\dagger, a_{k,B}^\dagger, a_{-k,A}, a_{-k,B})$, $X(k) = 2S(J-K)$, and $Y_\pm(k) = -2S(J\cos k \pm D\sin k)$.

For usual magnets with complicated terms, we use the numerical Bogoliubov transformation. However, the forms of analytical expressions in this system are relatively simple. We here give the explicit forms of $\hat{K}$, $\hat{K}^{-1}$, $\hat{\mathcal{H}}'$, and $\hat{U}$. The upper triangle matrix $\hat{K}_{\boldsymbol{k}}$ in the Cholesky decomposition is given by

$$\hat{K} = \sqrt{\frac{1}{X}} \begin{pmatrix} X & 0 & 0 & Y_- \\ 0 & X & Y_+ & 0 \\ 0 & 0 & \sqrt{X^2 - Y_+^2} & 0 \\ 0 & 0 & 0 & \sqrt{X^2 - Y_-^2} \end{pmatrix}, \tag{3.28}$$

and its inverse is

$$\hat{K}^{-1} = \sqrt{\frac{1}{X}} \begin{pmatrix} 1 & 0 & 0 & -Y_-/\sqrt{X^2 - Y_-^2} \\ 0 & 1 & -Y_+/\sqrt{X^2 - Y_+^2} & 0 \\ 0 & 0 & X/\sqrt{X^2 - Y_+^2} & 0 \\ 0 & 0 & 0 & X/\sqrt{X^2 - Y_-^2} \end{pmatrix}, \tag{3.29}$$

where we omit (k) for simplicity. Using Eq. (3.28), we obtain the dual Hamiltonian

$$\hat{\mathcal{H}}' = \frac{1}{X} \begin{pmatrix} X^2 - Y_-^2 & 0 & 0 & -Y_-\sqrt{X^2 - Y_-^2} \\ 0 & X^2 - Y_+^2 & -Y_+\sqrt{X^2 - Y_+^2} & 0 \\ 0 & -Y_+\sqrt{X^2 - Y_+^2} & -(X^2 - Y_+^2) & 0 \\ -Y_-\sqrt{X^2 - Y_-^2} & 0 & 0 & -(X^2 - Y_-^2) \end{pmatrix}. \tag{3.30}$$

This Hamiltonian can be diagonalized by a unitary matrix

$$\hat{U} = \begin{pmatrix} 0 & -\frac{(\sqrt{X^2 - Y_-^2} + X)}{Y_-} & -\frac{(\sqrt{X^2 - Y_-^2} - X)}{Y_-} & 0 \\ -\frac{(\sqrt{X^2 - Y_+^2} + X)}{Y_+} & 0 & 0 & -\frac{(\sqrt{X^2 - Y_+^2} - X)}{Y_+} \\ 1 & 0 & 0 & 1 \\ 0 & 1 & 1 & 0 \end{pmatrix}, \tag{3.31}$$

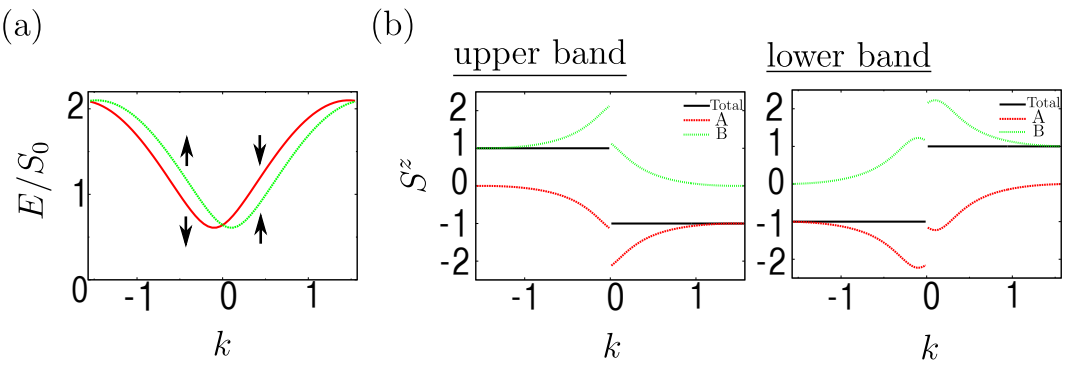

Figure 3.4: (a) Magnon band dispersions for $J = 1, D = 0.1$, and $K = -0.05$. (b) The contributions from the A and B sublattices to the z-component spin in the upper and lower bands are plotted for the momentum k. The total S^z is quantized, and its sign is changed across the band crossing points.

and the magnon eigenvalues are given by

$$E_{k,\pm} = \sqrt{X^2(k) - Y_{\pm}^2(k)}. \tag{3.32}$$

Note that Eq. (3.32) for $K = D = 0$ reproduces the magnon dispersion of the one-dimensional Heisenberg antiferromagnet [47]

$$E_{\boldsymbol{k}}^{AF} = 2JS|\sin k|, \tag{3.33}$$

which describes degenerated linear dispersions with two massless Nambu-Goldstone modes.

We plot magnon dispersions in Fig. 3.4 (a). The band structure has two splitted bands with two crossing points at $k = 0, \pi$. Since no spontaneous symmetry breaking occurs in this model, the massless Nambu-Goldstone modes do not appear.

3.2.3 Magnon weight and quantized magnon spin

Next, we discuss the magnon spin-momentum locking. The information of the magnon weight function is included in the paraunitary matrix

$$\hat{Q}_{\boldsymbol{k}} \equiv \hat{K}_{\boldsymbol{k}}^{-1}\hat{U}_{\boldsymbol{k}}\begin{pmatrix}\hat{E}_{\boldsymbol{k}}^{\frac{1}{2}} & 0\\ 0 & \hat{E}_{-\boldsymbol{k}}^{\frac{1}{2}}\end{pmatrix}$$
$$= \begin{pmatrix} 0 & -\frac{\sqrt{X}(\sqrt{X^2-Y_-^2}+X)}{Y_-(X^2-Y_-^2)^{1/4}} & \frac{\sqrt{X}(\sqrt{X^2-Y_-^2}-X)}{Y_-(X^2-Y_-^2)^{1/4}} & 0\\ -\frac{\sqrt{X}(\sqrt{X^2-Y_+^2}+X)}{Y_+(X^2-Y_+^2)^{1/4}} & 0 & 0 & \frac{\sqrt{X}(\sqrt{X^2-Y_+^2}-X)}{Y_+(X^2-Y_+^2)^{1/4}}\\ \frac{\sqrt{X}}{(X^2-Y_+^2)^{1/4}} & 0 & 0 & \frac{\sqrt{X}}{(X^2-Y_+^2)^{1/4}}\\ 0 & \frac{\sqrt{X}}{(X^2-Y_-^2)^{1/4}} & \frac{\sqrt{X}}{(X^2-Y_-^2)^{1/4}} & 0\end{pmatrix}, \tag{3.34}$$

where we have used $Y_+(k) = Y_-(-k)$. Using Eq. (3.34), we plot the magnon weight function and z-component magnon spin in Fig. 3.4 (b).

As shown in Chap. 2, the absence of the $U(1)$ symmetry breaking ensures that $|\boldsymbol{k},\alpha\rangle$ is an eigenstate of $S^z_{\rm tot}$. Thus, the z-component magnon spin $S^z_{\boldsymbol{k},\alpha}$ is quantized, while the contribution from each sublattice does not have to be. The fact that each contribution can be over 1 comes from the quantum nature of the antiferromagnetic magnon[3]. In the upper and lower bands, the sign of $S^z_{\boldsymbol{k},\alpha}$ is changed across the band crossing points. Clearly, this momentum-dependence of the magnon spin is an example of the *trivial* spin-momentum locking.

3.3 Magnon spin texture in momentum space

To explore noncollinear spin structures in momentum space such as a spin vortex in the topological insulator surface state, we should consider classical ground states with noncollinear spin structures in real space. As we have shown, however, the Heisenberg antiferromagnet on the triangular lattice, which is one of the simplest examples of the non-collinear antiferromagnet, is not an example of the magnon spin-momentum locking. In the following, we construct examples of the nontrivial magnon spin-momentum locking realized in the kagome lattice antiferromagnet. We will discuss the relationship between the model and a related material.

[3]In usual context, this is known as the quantum correction to the classical antiferromagnetic ground state. See Ref. [46].

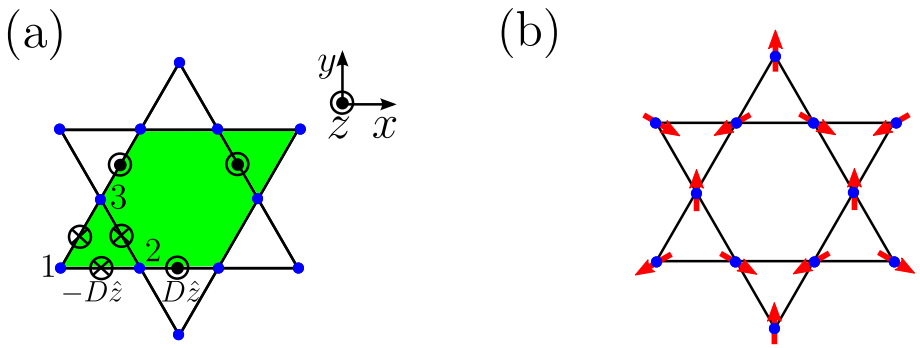

Figure 3.5: (a) Kagome lattice antiferromagnet with the Dzyaloshinskii-Moriya interaction denoted by $\pm D\hat{z}$. The magnetic unit cell, shown by the green region, is the same as the unit cell. (b) 120° structure on kagome lattice.

As an example of a noncollinear structure, we consider the 120° structure in kagome lattice antiferromagnets. The kagome lattice and magnetic order have the common periodicity with three sublattices. We analyze the following Hamiltonian:

$$H^{2D} = \sum_{\langle i,j \rangle} \left[\sum_a J^a S_i^a S_j^a + \boldsymbol{D}_{ij} \cdot (\boldsymbol{S}_i \times \boldsymbol{S}_j) \right], \tag{3.35}$$

where J^a are the nearest-neighbor exchange couplings, and $\boldsymbol{D}_{ij} = \pm D\hat{z}$ is the DM vector defined in Fig. 3.5 (a).

We consider the two interesting limits: (a) $J^x = J^y = J^z = J > 0$, $D > 0$ and (b) $J^x = J^y = J > 0$, $J^z = D = 0$, both of which have classical ground states with the 120° structure[4] and preserve the $U(1)$ symmetry around the z axis. We here choose the ground state shown in Fig. 3.5 (b). We set the sublattice positions

$$\boldsymbol{r}_1 = (0,0)\,, \boldsymbol{r}_2 = (1,0)\,, \boldsymbol{r}_3 = \left(\frac{1}{2}, \frac{\sqrt{3}}{2}\right), \tag{3.36}$$

[4]Strictly speaking, there is another ground state, $\sqrt{3} \times \sqrt{3}$ structure, for the case (b). In the presence of small but finite DM interaction, which exists in realistic materials, we do not have to consider this degeneracy.

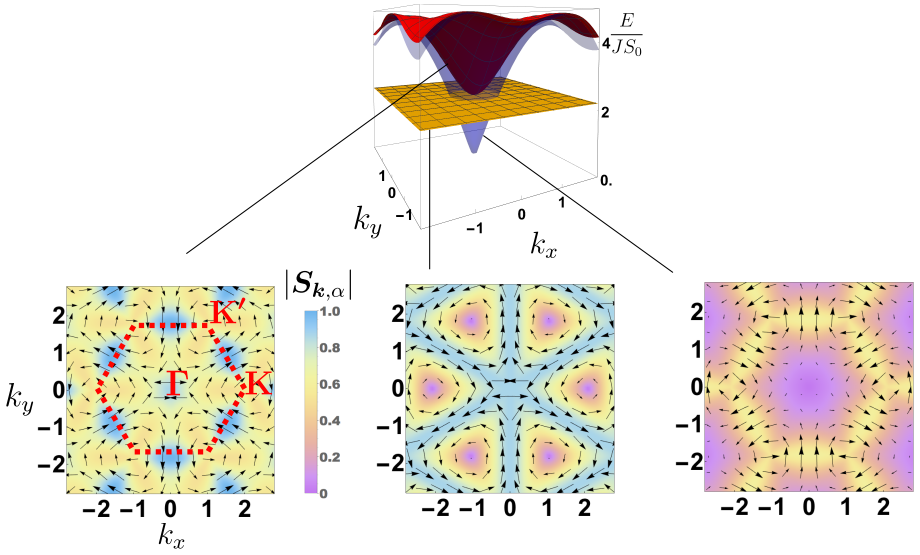

Figure 3.6: Magnon band dispersions and magnon spin in kagome lattice antiferromagnets described by Eq. (3.35) with $J^x = J^y = J^z = 1, D = 0.1$.

and the local rotating frame

$$M_1^x = (0,0,-1)\,, M_1^y = \left(\frac{1}{2}, -\frac{\sqrt{3}}{2}, 0\right), M_1^z = \left(-\frac{\sqrt{3}}{2}, -\frac{1}{2}, 0\right),$$
$$M_2^x = (0,0,-1)\,, M_2^y = \left(\frac{1}{2}, \frac{\sqrt{3}}{2}, 0\right), M_2^z = \left(\frac{\sqrt{3}}{2}, -\frac{1}{2}, 0\right),$$
$$M_3^x = (0,0,-1)\,, M_3^y = (-1,0,0)\,, M_3^z = (0,1,0)\,. \tag{3.37}$$

3.3.1 Isotropic Heisenberg antiferromagnet with the DM interaction

The case (a) corresponds to the isotropic Heisenberg antiferromagnet with the staggered out-of-plane DM interaction. By mapping Eq. (3.35) to the magnon Hamiltonian and performing the numerical Bogoliubov transformation, we plot the magnon band dispersions and magnon spin for case (a) in Fig. 3.6. The band structure for the case (a) has the finite-energy flat band, which is reminiscence of the zero energy flat band in the classical spin liquid phase of the isotropic Heisenberg model. There is one massless Nambu-Goldstone mode associated with the symmetry breaking $U(1) \to \{e\}$, and we can observe noncollinear spin

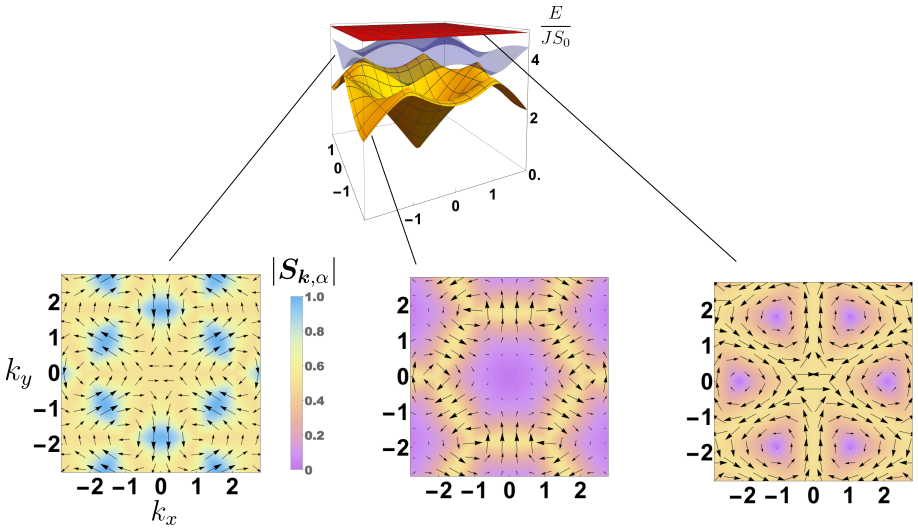

Figure 3.7: Magnon band dispersions and magnon spin in kagome lattice antiferromagnets described by Eq. (3.35) with $J^x = J^y = 1, J^z = D = 0$.

structure in momentum space, as shown in Fig. 3.6.

The norm of magnon spin is no longer quantized due to the absence of any spin rotational symmetries. The most striking feature is that spin textures in the highest and flat bands have spin vortices with the winding number $Q = -2$ defined in a closed curve around a Γ point, while the original spin-momentum locking in electron systems is characterized by $Q = +1$. Although the vector plot can depend on the choice of the ground state, all plots for $U(1)$-degenerated ground states can be identified up to overall rotation in spin space, which preserves the winding number of the vortexlike spin structures.

3.3.2 Antiferromagnetic XY model

The case (b) corresponds to the antiferromagnetic XY model. The band structure for the case (b) also has the finite-energy flat band and one massless Nambu-Goldstone mode for the same reasons. In addition, there are two Dirac points with a finite energy in the K and K' points, as shown in Fig. 3.7. For each Dirac cone, a spin vortex characterized by $Q = +1$ is realized, which is a magnonic analogue of the topological insulator surface state. Note that the magnon spin-momentum locking does not require the DM interaction. In magnonic systems, interesting physics can occur even in the absence of the DM interaction. For instance, Owerre showed that the topological thermal Hall effect occurs in such

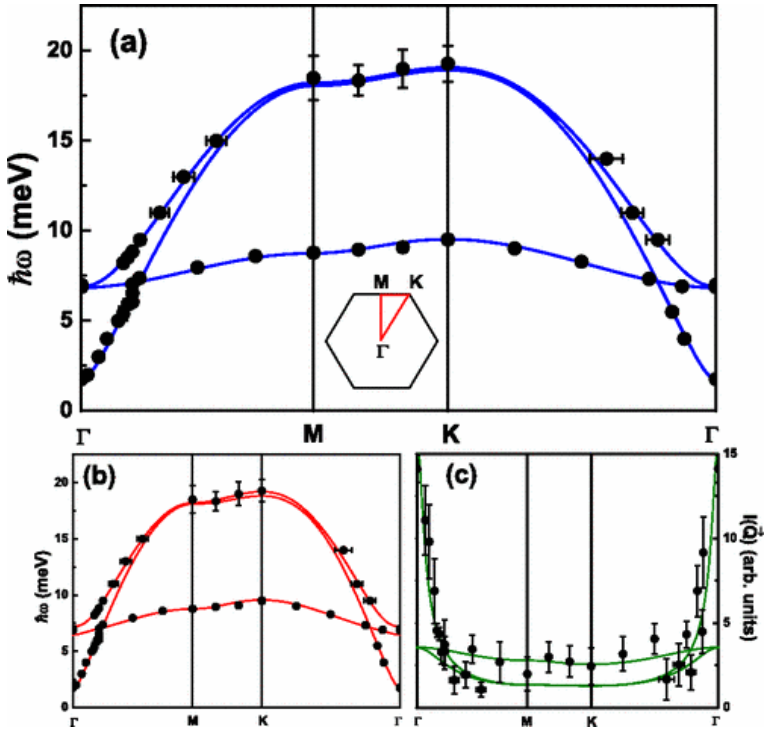

Figure 3.8: Spin wave dispersion along the high symmetry directions in the two-dimensional Brillouin zone from Ref. [60]. Solid lines in (a) and (b) denote the dispersions calculated for the DM and crystal field models, respectively. (c) Momentum-dependence of the spin wave intensity. Solid line corresponds to the DM model calculation.

a situation [58].

3.4 Experimental detection

We here discuss possibilities of experimental detections of the magnon spin-momentum locking.

3.4.1 Candidate material

The effective spin Hamiltonian of a kagome antiferromagnet $KFe_3(OH)_6(SO_4)_2$ is thought to be described by a model similar to Eq. (3.35) for the case (a) [59, 60]. The ground state of this material is the 120° structure with small canting in out-of-plane direction. In this material, the $S = 5/2$ Fe^{3+} ions form a kagome

lattice antiferromagnet. This relatively large spin would enable us to treat this spin system in the semiclassical spin-wave approximation.

A spin wave dispersion obtained by inelastic neutron scattering [60] is shown in Fig. 3.8. In Ref. [60], two models are used to fit the dispersion, i.e., the DM and crystal field models, and the authors concluded that the former model would be more appropriate[5]. In the following, we assume the DM model.

The dispersion seems to be very similar as Fig. 3.6. However, the DM model in Ref. [60] has additional terms to Eq. (3.35) to describe the small difference from our simple model. First, it has second-nearest neighbor exchange coupling terms to describe the distortion of the "flat band". Second, it has in-plane DM interactions to describe the small canting of the ground state. In this case, the Hamiltonian itself breaks the U(1) spin-rotational symmetry in the z direction, and the massless Nambu-Goldstone mode is slightly lifted.

In this material, the magnon spin has the finite z component. However, this component is much smaller than in-plane components. This is because of the small canting angle of the ground state ($\sim 1^\circ$). Thus, the magnitude of the in-plane components of magnon spin is not so changed from our simple model. In addition, the vortex-like spin texture in momentum space would be expected to be topologically stable. Thus, the similar spin texture would be realized in this material even in the presence of additional terms. Note that the simple picture of spin-momentum locking induced by spontaneous symmetry breaking does not hold in this material.

3.4.2 Spin Seebeck effect for spin vortex with $Q = -2$

Since magnon spin cannot be driven by the electric field, we should investigate other transports such as light and thermal responses. As shown in Sec. 2.1, magnon spin can be detected by the spin Seebeck measurement. In usual collinear antiferromagnet without an external magnetic field, however, the spin Seebeck effect does not occur due to the degeneracy between the up and down bands. In the case of the magnon spin-momentum locking with $Q = -2$, on the other hand, we can expect the finite spin Seebeck effect due to the absence of such degeneracies. In the following, we discuss it.

To capture the essence of the spin vortex, we approximate the magnon spin as

$$\boldsymbol{S}_{\boldsymbol{k}} = (\sin 2\theta_{\boldsymbol{k}}, \cos 2\theta_{\boldsymbol{k}}, 0), \tag{3.38}$$

[5]For instance, the energy splitting around 7 meV [Fig.3.8 (b)] in crystal field model is too large to fit the experimental data.

where $\theta_{\boldsymbol{k}}$ is the polar angle of the momentum $\boldsymbol{k}$. Suppose that a thermal gradient is applied in the x direction. The linearized Boltzmann equation for steady-state magnons in the bulk is given by

$$v_{k_x}\partial_x T\frac{\partial n_{\boldsymbol{k}}^{(0)}}{\partial T} = -\frac{\delta n_{\boldsymbol{k}}}{\tau_m}, \tag{3.39}$$

where the notations are the same as in Chap. 1. We here ignore the inter-band effect such as the Berry curvature contributions because we focus on the non-topological longitudinal transport. In this approximation, the y-component magnon spin current flowing in x direction is given by

$$j_x^{Sy} = \int \frac{d^2k}{(2\pi)^2} S_{\boldsymbol{k}}^y v_{k_x}\delta n_{\boldsymbol{k}}. \tag{3.40}$$

Using the approximation $v_{k_x} \propto \cos\theta_{\boldsymbol{k}}$ and the above equations, we obtain finite spin current:

$$j_x^{Sy} \propto \int d\theta_{\boldsymbol{k}} \cos 2\theta_{\boldsymbol{k}} \cos^2\theta_{\boldsymbol{k}} \neq 0. \tag{3.41}$$

From this symmetry argument, we can expect the finite spin Seebeck voltage in an experiment. By replacing 2θ with $n\theta$ in Eq. (3.41), we can discuss general winding numbers. Interestingly, spin current can be large only for $|Q| = 0, 2$ cases since periodicity of $v_{k_x}\delta n_{\boldsymbol{k}} \propto \cos^2\theta_{\boldsymbol{k}}$ is π. In other words, we can indirectly check the presence of the spin vortex with the winding number $Q = -2$ in the framework of the spin Seebeck effect. Since the considered model does not have the four-fold rotation, the transport phenomenon in the y direction is different from that in the x direction[6]. This property enables us to distinguish our case from the conventional spin Seebeck effect with $Q = 0$.

In realistic magnets, there are other thermal effects in addition to the spin Seebeck effect. In particular, the electron contributions cannot be ignored in magnetic metals. Thus, magnetic insulators such as $KFe_3(OH)_6(SO_4)_2$ discussed above would be good candidates. In the case of $KFe_3(OH)_6(SO_4)_2$, the magnon bands with $Q = -2$ are in the high-energy region. In order to obtain a large signal, an experiment should be performed at high temperature.

[6]If we apply a thermal gradient in the y direction, we obtain a finite spin Seebeck signal corresponding to $j_y^{S_y}$. Magnon spin carried by the net magnon current is parallel to the current direction.

3.4.3 Neutron scattering

In the case of electron systems, the angle-resolved photoemission spectroscopy (ARPES) [12] enables us to detect the momentum-dependent electron spin. So far, there is no counterpart for the magnonic systems. One possibility is the inelastic neutron scattering measurement, which is a typical probe for determining the magnon dispersion. In this framework, the total magnetic cross-section is closely related to the imaginary part of the generalized susceptibility defined by [61, 62]

$$\begin{aligned}\Im[\chi^{dd'}_{\alpha\beta}(\boldsymbol{Q},E)] =& 4\pi\mu_B^2 f_d^*(\boldsymbol{Q}) f_{d'}(\boldsymbol{Q})(1-\exp\left[-E/(k_BT)\right]) \\ & \sum_l \exp(i\boldsymbol{Q}\cdot\boldsymbol{R}_l)\exp(i\boldsymbol{Q}\cdot(\boldsymbol{r}_{d'}-\boldsymbol{r}_d)) \\ & \int_{-\infty}^{\infty}\frac{dt}{2\pi\hbar}\exp(-iEt/\hbar)\langle\mu_{0d\alpha}(0)\mu_{ld'\beta}(t)\rangle, \end{aligned} \tag{3.42}$$

where d, d' denote the sublattice, α, β denote the component of the spin angular momentum, $(\boldsymbol{Q}, E)$ are the scattering momentum and energy, f is the magnetic form factor, $\boldsymbol{R}_l$ is the primitive lattice vector, $\boldsymbol{r}_d$ is the relative coordinate in a sublattice, and μ is the magnetic moment defined on one atom. Usually, the inelastic measurement is performed in order to determine the magnon dispersion by investigating the poles of Eq. (3.42). To determine the magnon spin, we should also analyze the magnitude of the cross-section. If we can distinguish the contributions from sublattices, it is in principle possible to obtain the spin texture in momentum space in this framework. One difficulty is that the cross-section is given by the summation over the spin indices for usual unpolarized neutrons. Thus, the polarized neutron scattering would be appropriate for the magnon spin-momentum locking measurement. Establishing the magnonic analogue of the ARPES is an important future work.

3.5 Summary

We presented a theory of the magnon spin-momentum locking. We gave conditions for magnon spin to be independent of momentum and constructed examples of spin-momentum locking by avoiding such conditions. We find the first example of spin-momentum locking induced by spontaneous symmetry breaking. We also discuss the possibilities for detecting the magnon spin-momentum locking experimentally. A kagome lattice antiferromagnet $KFe_3(OH)_6(SO_4)_2$ is described by a similar model as the model we used in the main part, and we can expect that almost the same magnon spin texture is realized in this material. The spin

vortex with $Q = -2$ realized in our model, which has not been observed in realistic electron models, is expected to be observed by using the spin Seebeck measurement. We found that $|Q| = 0, 2$ are important for the finite spin current generation The neutron scattering is one possibility for the direct observation of the magnon spin-momentum locking. We expect that magnonic analogue of the angle-resolved photoemission spectroscopy would be established in the framework of the inelastic neutron scattering.

Chapter 4

Spin texture and topology

In this chapter, we discuss spin textures in momentum space in terms of topology. We introduce some related notions and techniques in mathematics, which are also useful in the later chapters. Using the Poincaré-Hopf index theorem, we derive the sum rule for the winding numbers in momentum space. The simple relation between spin textures and topology motivates the mathematical classification of spin textures in the presence of additional factors. In the following chapters, we focus on the space group symmetry operation as s new factor, which acts on real space position, momentum, and spin carried by quasiparticles. In the last section, we set the problems that we address in the later chapters.

4.1 The Poincaré-Hopf index theorem

In mathematics, there are a lot of surprising theorems that relate local quantities of a space with global (or topological) properties of it. The most famous and fundamental one is the Gauss-Bonnet theorem [63, 64], which relates the curvature of a manifold with the Euler characteristic, a typical topological invariant of the manifold. Another interesting and important example is the Atiyah-Singer index theorem [64], which attracts much interest of theoretical physicists since it is closely related to the gauge theory and recent topological material science [65].

In this section, we explain the Poincaré-Hopf index theorem [63], which relates the winding number of a vector field of a manifold with the Euler characteristic of it. We here give both the mathematical definition and rough explanation (most of readers would prefer it!) for each concept.

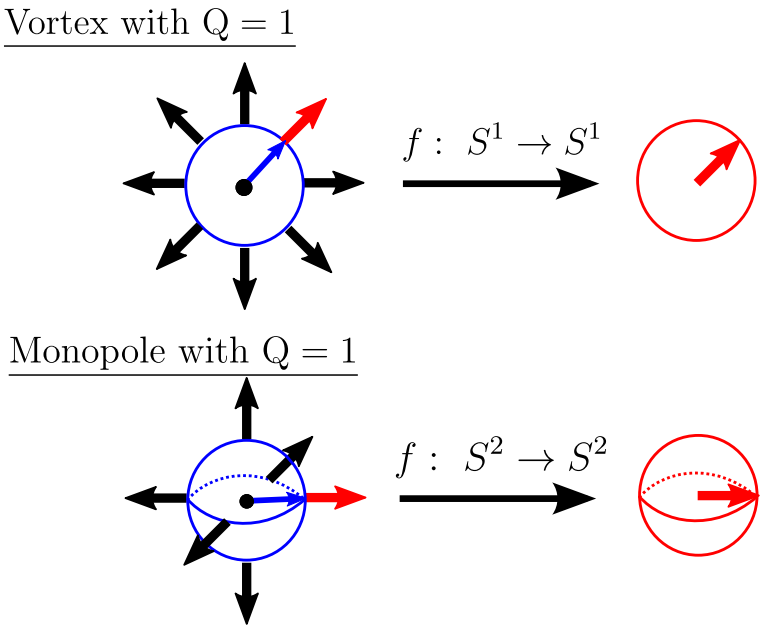

Figure 4.1: Schematics of the map $f : S^{d-1} \to S^{d-1}$ for $d = 2, 3$.

4.1.1 Winding number for any dimensions

We here generalize the winding number for any dimensions. For a vector field $\boldsymbol{v}$ on a d-dimensional space, the winding number around a singular point of the vector field is given by the degree of the map $f : S^{d-1} \to S^{d-1}$ from the sphere around the singular point to the sphere given by $\boldsymbol{v}/|\boldsymbol{v}|$ [Fig. 4.1].

In terms of differential forms, the degree of mapping is given in the simple expression [66]. Let ω be the volume form of the target sphere. By definition, ω is a closed $(d-1)$-form whose integral is 1:

$$\begin{aligned} d\omega &= 0, \\ \int_{S^{d-1}} \omega &= 1. \end{aligned} \tag{4.1}$$

Using this ω, we obtain the simple expression of the winding number

$$Q = deg f \equiv \frac{\int_{S^{d-1}} f^*\omega}{\int_{S^{d-1}} \omega} = \int_{S^{d-1}} f^*\omega, \tag{4.2}$$

where f^* is the pull-back of ω by f.

For convenience, we give the explicit form of the winding number around a singular point for two and three dimensions, which are particularly important

in condensed matter physics. In two dimensions, an isolated singular point of a vector field is called a vortex, as discussed in the previous chapters. The winding number of the vortex is given by

$$Q_{\text{vortex}} = \frac{1}{2\pi} \oint_{S^1} ds(\boldsymbol{n} \times \partial_s \boldsymbol{n})_z, \tag{4.3}$$

where $\boldsymbol{n} = \boldsymbol{v}/|\boldsymbol{v}|$. In three dimensions, an isolated singular point of a vector field is called a monopole. The winding number of the monopole is given by

$$Q_{\text{monopole}} = \int_{S^2} dx^2 \epsilon_{ij} \boldsymbol{n} \cdot (\partial_i \boldsymbol{n} \times \partial_j \boldsymbol{n}), \tag{4.4}$$

where ϵ_{ij} is the completely antisymmetric tensor.

4.1.2 The Euler characteristic of topological space

Roughly speaking, topology is a field of mathematics that deals with the invariant properties of space under a continuous deformation. One of the most important concepts in this field is the topological invariant, which is a global quantity calculated from the information of the whole space. We here explain the oldest topological invariant, the Euler characteristic. We first give the mathematically rigorous definition and then how we can calculate it intuitively.

In terms of the homology group, the Euler characteristic is defined as follows. Let X be a topological space and $H_i(X)$ $(i = 0, 1, 2, \cdots)$ homology groups. Then the Euler characteristic of X is given by

$$\chi(X) = \sum_{i=0}^{\infty} (-1)^i b_i, \tag{4.5}$$

where b_i is the Betti number, which is a rank of $H_i(X)$ as an Abelian group. Since the Betti number is a topological invariant, the Euler characteristic is also a topological invariant.

Because the above definition is too mathematical, we here give a more intuitive description. We first review the celebrated Euler's polyhedron formula, in which the Euler characteristic appears. Let P be a convex polyhedron. Then the Euler's polyhedron formula is given by

$$2 = V - E + F, \tag{4.6}$$

where V, E, and F are the numbers of the vertex, edge, and face of P, respectively [Fig. 4.2(a)]. Actually, the left-hand side of this equation is equal to the Euler

characteristic of P. Convex polyhedrons are homeomorphic with the two-sphere, and the Euler characteristic of P is equal to that of the two-sphere since the Euler characteristic is invariant under the homeomorphic transformation.

The above discussion about the Euler's polyhedron formula tells us that the Euler characteristic of a topological space X might be computed by considering some *polyhedron* P that is homeomorphic with X. To compute the Euler characteristic in this context, we introduce the cell decomposition of space. We here give a rough description and some examples rather than the mathematical definition.

Cell decomposition

The cell decomposition of n-dimensional space is the procedure to decompose the space into the union of i-dimensional cells e_i $(i = 0, 1, \cdots, n)$ satisfying below.

- For $i = 1, \cdots, n$, the boundary of e_i, ∂e_i, is composed of a union of e_j $(j < i)$.
- $e_i \setminus \partial e_i$ do not have intersections each other.

In the case of two-dimensional space, e_0, e_1, and e_2 correspond to the vertex, edge, and face, respectively.

For example, the cell decompositions of the two-dimensional torus $\mathbb{T}^2$ and two-sphere S^2 are given in Fig. 4.2(b). For later convenience, we also draw the nets of these spaces. The lines with same arrows are identified.

Once we get the cell decomposition of the space, we can easily compute the Euler characteristic as follows:

$$\chi(X) = \sum_i (-1)^{i-1} \nu_i, \tag{4.7}$$

where ν_i is the number of i-dimensional cells contained in the cell decomposition of the space. For example, the Euler characteristics of the two-dimensional torus $\mathbb{T}^2$ and two-sphere S^2 are calculated by using the cell decompositions in Fig. 4.2(b) as follows:

$$\begin{aligned} \chi(\mathbb{T}^2) &= 1 - 2 + 1 = 0, \\ \chi(S^2) &= 3 - 2 + 1 = 2. \end{aligned} \tag{4.8}$$

It is known that the Euler characteristic of the space does not depend on the choice of its cell decomposition. Instead of the proof, we here note that convex polyhedrons discussed above correspond to the different cell decompositions of

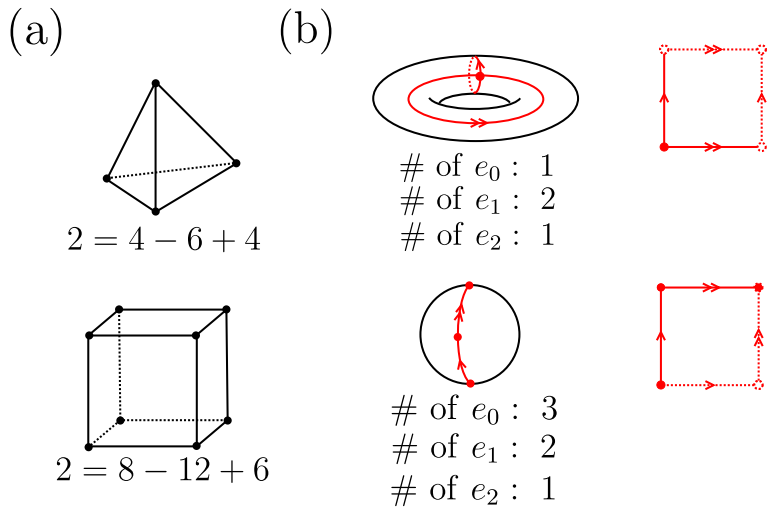

Figure 4.2: (a) Examples of the Euler's polyhedron formula. (b) The cell decompositions of the two-dimensional torus and two-sphere.

the two-sphere. Thus, the celebrated Euler's polyhedron formula is an example of this invariant property.

4.1.3 Statement and proof

Using the notions defined above, we here describe the Poincaré-Hopf index theorem with a rough proof.

The Poincaré-Hopf index theorem

Let M be a compact differentiable manifold and $\boldsymbol{v}$ a vector field on M. Suppose that i are the isolated zero points of $\boldsymbol{v}$, and there are no non-isolated zeros. If M has boundaries, we also assume that $\boldsymbol{v}$ be pointing in the outward normal direction along the boundary.
Then the Poincaré-Hopf index theorem states that

$$\chi(M) = \sum_i Q_i, \tag{4.9}$$

where $\chi(M)$ is the Euler characteristic of M, and Q_i are the winding numbers around i.

Proof. If we assume that the sum of the winding numbers around zeros does not

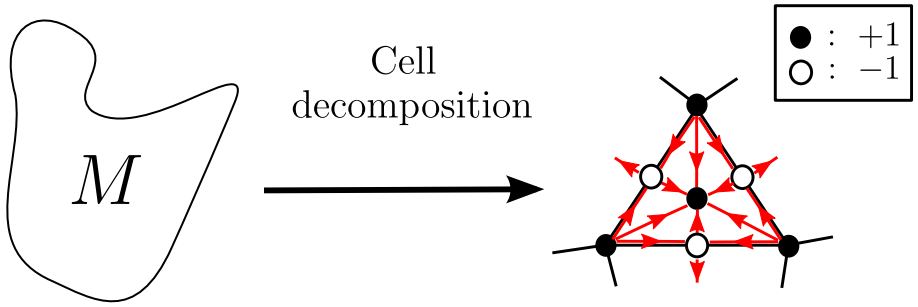

Figure 4.3: Specific vector field on the cell decomposition of the manifold M. Zeros with winding numbers $Q = (-1)^{n-1}$ are located on the centers of n-dimensional cells.

depend on a choice of a vector field on M, we can easily and intuitively prove the Poincaré-Hopf index theorem. For convenience, we again introduce a cell decomposition C_M of the manifold M. We here consider a vector field on the cell decomposition, instead of the manifold itself. Using the above assumption, we consider the specific vector field that has isolated zeros on the centers of all cells. We can always assign $Q = (-1)^{n-1}$ for the zero on the center of each n-dimensional cell, as shown in Fig.4.3. In such a vector field, we obtain

$$\begin{aligned} \chi(C_M) &\equiv (\#\text{ of vertices}) - (\#\text{ of edges}) + (\#\text{ of faces}) \cdots \\ &= \sum_i Q_i \end{aligned} \tag{4.10}$$

because the number of n-dimensional cells are equal to that of the centers of them. □

The statements in some textbooks require the orientability of the manifold, though this theorem can also be applied to compact unoriented manifolds [67]. Also, there are several generalizations of the Poincaré-Hopf index theorem. For instance, we will use the Poincaré-Hopf index theorem for the space with singular points in Chap. 8.

4.2 Application to the magnon spin-momentum locking

In Chap. 3, we plot magnon spin textures in momentum space. Since z-component spin is zero, the spin texture is interpreted as a vector field on a

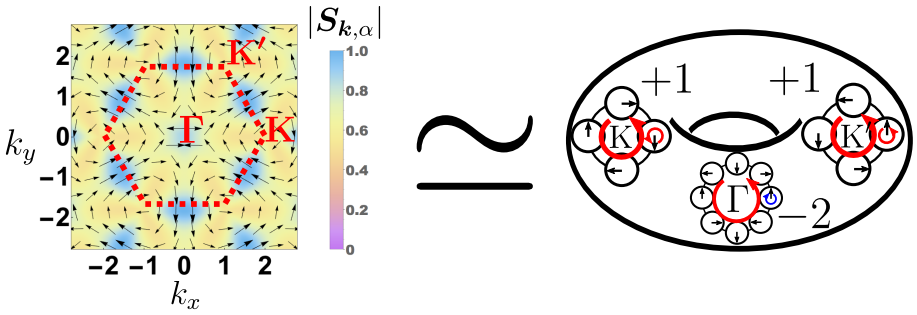

Figure 4.4: Magnon spin texture in momentum space as a vector field on two-dimensional torus.

two-dimensional space. In condensed matter, the momentum space, or more precisely the Brillouin zone, is mathematically equivalent to the torus. Thus, we can interpret the plots as vector fileds on the two-dimensional torus $\mathbb{T}^2$, and the Poincaré-Hopf index theorem can be applied to the plots.

As an example, we consider the highest band of the case (a) [Fig. 4.4]. Γ, K, and K' are the zeros of the spin texture with $Q = -2, +1, +1$, respectively. The Poincaré-Hopf index theorem holds in this plot:

$$0 = \chi(\mathrm{BZ}^2) = \chi(\mathbb{T}^2) = \sum_{i=\Gamma,K,K'} Q_i = -2 + 1 + 1, \tag{4.11}$$

where BZ^2 denotes the Brillouin zone for two dimensions. We here use $\chi(\mathbb{T}^2) = 0$. Interestingly, the sum of the winding numbers of spin textures over the Brillouin zone should be equal to zero.

The above sum rule can be also applied to spin textures defined on the three-dimensional Brillouin zone since $\chi(\mathbb{T}^3) = 0$. In the case of three dimensions, we do not have to assume that z-component of spin is zero. In the following, we summarize the sum rule.

Sum rule for the spin texture in momentum space

two dimensions
Suppose that z-component spin is zero. If the spin texture does not have non-isolated zeros such as a nodal line, then the sum of the winding numbers of spin vortices over the Brillouin zone is equal to zero.
three dimensions
If the spin texture does not have non-isolated zeros such as a nodal line and a spin-degenerated plane, then the sum of the winding numbers of spin monopole structures over the Brillouin zone is equal to zero.

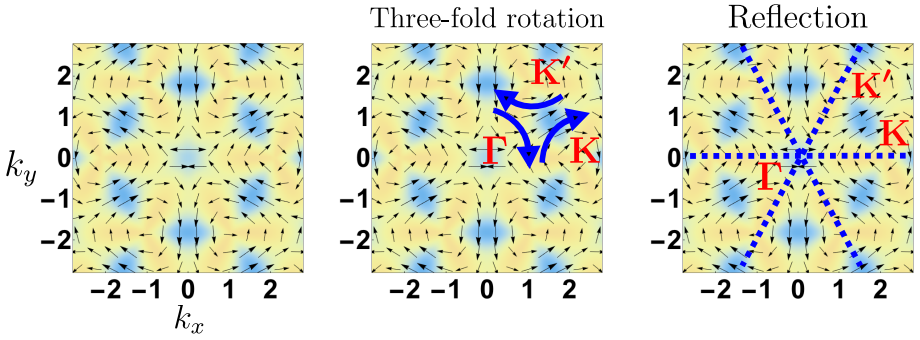

Figure 4.5: Symmetries of magnon spin texture in momentum space.

4.3 Spin texture under space group symmetries

As discussed above, a spin configuration in momentum space is restricted by the topology of the torus (Brillouin zone). This idea is the starting point of the later chapters.

In solid state physics, momentum space is equivalent to the torus, as mentioned above. This fact comes from the discrete translational symmetry of the crystal. Since the total spin operator commutes with the discrete translation operator[1], the $\boldsymbol{k}$-dependent spin is a single-valued function over the torus. In other words, the translation invariance restricts the spin configuration in momentum space. Proceeding further, a natural question arises. HOW ABOUT OTHER SYMMETRIES?

Look at Fig. 4.5. This plot is beautiful, isn't it? The reason why this picture is beautiful is that it has a lot of symmetries. In addition to the translation invariance, there are three-fold rotational symmetries around the Γ, K, K' points. By considering that spin is a pseudovector[2], this picture also has the reflection symmetries with the mirror lines along Γ-K and Γ-K' lines. Since these space group symmetry operations act both on spin and coordinate, spin textures in momentum space should be restricted by such symmetries. Thus, we can expect stronger conditions for spin textures than the sum rule discussed above.

[1] In the case of ordered state, we define the discrete translation compatible with the periodicity of the order.

[2] For the reflection operation, the behavior of spin is different from that of the coordinate. See the later chapters for details.

4.4 Motivation of the later chapters

In this section, we explain the motivation of the later chapters. Motivated from the Poincaré-Hopf index theorem for the Brillouin zone and symmetry considerations for spin textures, we classify singular spin structures under the space group symmetries. For convenience, we will introduce the notion of the orbifold, which is a simple generalization of the manifold. We will first review the space group and basics of orbifold. Then we define the momentum space orbifold under the space group symmetries. Using the notion of the momentum space orbifold, we derive constraints on spin textures in momentum space under some space group symmetries. The derived constraints for a given material enable us to find interesting spin textures such as the Weyl points and higher-winding-number spin monopoles.

As mentioned above, we do not have to assume that the z component of spin is zero for three-dimensional systems. In the following chapters, we mainly discuss the three-dimensional systems. In addition, we also switch the subject from magnon spin-momentum locking to the usual electron spin-momentum locking. This is because the value of magnon spin often takes zero for the whole Brillouin zone. Note that we can still apply the discussions in the later chapters for the magnonic systems by considering the difference from electron systems carefully.

Chapter 5

Relevant knowledge of space group

The space groups are discrete groups that describe the symmetric properties of crystals. Symmetry operations in space groups preserve the structure of crystals. Thanks to the translational invariance of crystals, there are additional restrictions that are absent in the case of one molecule. In the presence of the translational invariance, the number of point groups is reduced to 32. Roughly speaking, these crystallographic point groups describe macroscopic properties of materials[1]. When we are interested in the band structure, the lattice structure is also an important factor. The combination of point group symmetries and lattice structures plays an important role in the later chapters.

In this section, we first explain the notions in the space group theory based on Ref. [68, 69]. Then we briefly review the relationship between space groups and topological condensed matter physics.

5.1 Translation group and Bravais lattice

By definition, there are three discrete translation symmetries in a three-dimensional crystal. Any translation symmetry operations are generated by three primitive vectors $\boldsymbol{t}_1, \boldsymbol{t}_2, \boldsymbol{t}_3$:

$$\boldsymbol{t_n} = n_1\boldsymbol{t}_1 + n_2\boldsymbol{t}_2 + n_3\boldsymbol{t}_3, \tag{5.1}$$

where n_i are integers. Although the real materials are finite and have boundaries, we often ignore effects of them. To get rid of the boundary effects mathematically,

[1]Although this statement is often remarked in traditional textbooks about space groups, some macroscopic properties such as the anomalous Hall conductance depend on the details of band structures, which cannot be determined without the information of lattice.

we here impose the periodic boundary conditions in three directions with the period N. Under the periodic boundary conditions, the set $\{\boldsymbol{t_n}\}$ forms a group. This is called the translation group, which is the most fundamental building block of the space group. Under the translation operations defined in Eq. (5.1), the properties of crystals such as the crystal structure should be invariant.

In addition to the translation group, we here introduce the notion of the Bravais lattice. The Bravais lattice is constructed by applying the translation $\boldsymbol{t_n}$ to one point. The generated points form a lattice structure, which reflects the translation invariance. The types of the Bravais lattices depend on the symmetries that are in the given materials (see Sec. 5.4).

5.2 Symmetry operations in space group

In addition to the translation symmetry, there are several types of symmetries that preserve crystal structures. These symmetries are generally interpreted as the combination of a discrete rotation in the orthogonal group in three dimensions $O(3)$ and a discrete translation, which does not have to be a primitive translation. For convenience, we introduce the following notation:

$$\boldsymbol{r}' = \alpha\boldsymbol{r} + \boldsymbol{b} \equiv \{\alpha|\boldsymbol{b}\}\boldsymbol{r}, \tag{5.2}$$

where α is a $O(3)$ rotation matrix and $\boldsymbol{b}$ is a translation vector. In this notation, a premitive translation is expressed as

$$\{\epsilon|\boldsymbol{t_n}\}, \tag{5.3}$$

where ϵ is the identity matrix. Again, $\boldsymbol{b}$ is not always an element of $\{\boldsymbol{t}_n\}$. Note that such nonprimitive translations can be achieved only for $\alpha \neq \epsilon$.

In the following, we introduce all symmetry operations allowed in crystals [Fig. 5.2]. We first consider the cases with $\boldsymbol{b} \in \{\boldsymbol{t_n}\}$. The operations with $\det\alpha = 1$ are called as rotations, which belong to the rotation group in three dimensions $SO(3)$. For the cases with $\det\alpha = -1$, there are three types of operations: reflection, inversion, and rotoreflection. The former and latter operations are also called as proper and improper rotations, respectively. After explaining operations with primitive translations, we consider the cases with $\boldsymbol{b} \notin \{\boldsymbol{t_n}\}$.

5.2.1 Rotation

We here consider (proper) rotational symmetries for crystals in addition to the translation symmetry. However, the types of rotational symmetries are limited because they should be compatible with the translation symmetry. The number of such symmetries is only four, i.e., $n = 2, 3, 4, 6$-fold rotational symmetries.

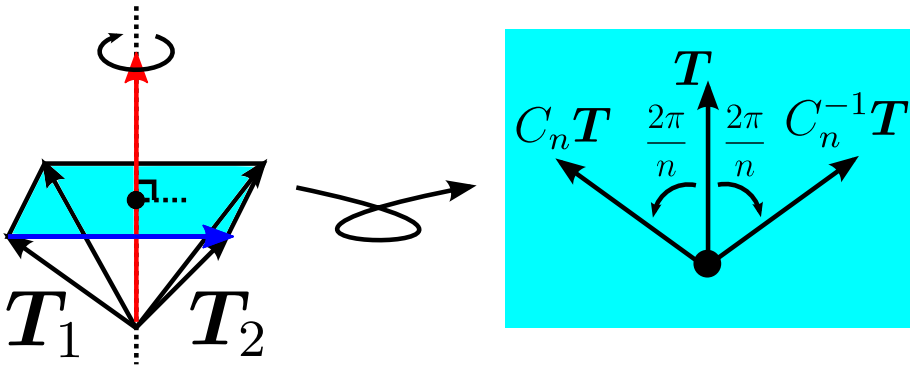

Figure 5.1: Left panel: schematic picture of $n = 2, 3, 4, 6$-fold rotations. The red and blue arrows denote $\sum_i \boldsymbol{T}_i$ and $\boldsymbol{T}_2 - \boldsymbol{T}_1$, respectively. Right panel: Bravais lattices on the blue plane in the left panel.

Proof. Let $\boldsymbol{T}_1$ be a Bravais lattice vector. By applying the n-fold rotation C_n iteratively, we obtain n Bravais lattice vectors $\boldsymbol{T}_i$ $(i = 1, 2, \cdots, n)$ with the same length. Then, the sum

$$\sum_{i=1}^{n} \boldsymbol{T}_i \tag{5.4}$$

is also a Bravais lattice vector, which should be parallel to the rotation axis [Fig.5.1]. The differences

$$\boldsymbol{T}_i - \boldsymbol{T}_{i-1} \ (\boldsymbol{T}_0 \equiv \boldsymbol{T}_n) \tag{5.5}$$

are also Bravais lattice vectors, which should be perpendicular to the rotation axis. Let $\boldsymbol{T}$ be the smallest Bravais lattice vector that is perpendicular to the rotation axis. By applying the n-fold rotations, we obtain two Bravais vectors $C_n\boldsymbol{T}$ and $C_n^{-1}\boldsymbol{T}$. The sum of them

$$C_n\boldsymbol{T} + C_n^{-1}\boldsymbol{T} = 2\cos\left(\frac{2\pi}{n}\right)\boldsymbol{T} \tag{5.6}$$

should be also a Bravais vector. Because this vector is proportional to $\boldsymbol{T}$, which is the smallest Bravais lattice vector perpendicular to the rotation axis, we obtain the following condition for n:

$$2\cos\left(\frac{2\pi}{n}\right) = (\text{integer}). \tag{5.7}$$

The integers satisfying this equation are n =2,3,4, and 6. □

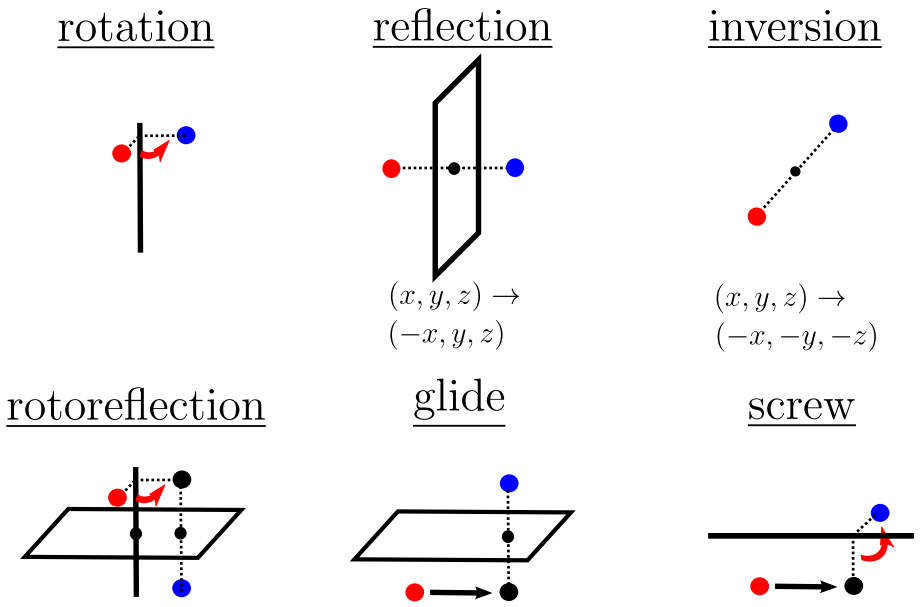

Figure 5.2: Schematic pictures of symmetry operations in space groups. Planes and solid lines denote the reflection planes and rotation axes, respectively. Under the symmetry operations, red points are moved to blue points.

5.2.2 Reflection, inversion, and rotoreflection

In three dimensions, symmetry operations with sign flips of one and three components, whose determinants are -1, are called reflection and inversion, respectively. These are not elements of $SO(3)$, which are also called as improper rotations. We can also construct other improper rotations by combining proper and improper rotations. These operations are called as the rotoreflection. The number of types of the rotoreflections is the same as that of the proper rotation, i.e., $n = 2, 3, 4, 6$-fold rotoreflections. Note that the $n = 2$ case is nothing but the inversion. If we discuss the point groups of rotoreflections, we focus only on the $n = 4, 6$-fold rotoreflections because the $n = 3$ case is equivalent to another point group, as shown later.

5.2.3 Glide and screw

The above operations can be written as the pure $O(3)$ rotations. In addition to such operations, we can also construct symmetry operations by combining pure $O(3)$ rotations discussed above and nonprimitive lattice translations, which do not belong to $\{\boldsymbol{t_n}\}$. The combinations of proper rotations and nonprimitive

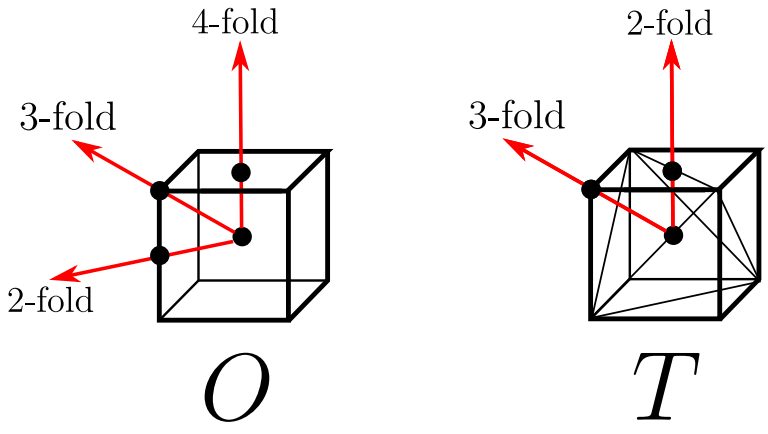

Figure 5.3: Point groups O and T.

lattice translations are called as the glide operations. The combinations of the reflection and nonprimitive lattice translations are called as the screw operations.

5.3 Crystallographic point group

By gathering the pure $O(3)$ rotations discussed above, we can construct the crystallographic point groups. The number of types of the crystallographic point groups is limited to 32 because the number of the rotations is limited as shown above. We here list all of them explicitly.

$\underline{C_n}$
The groups generated by $n = 1, 2, 3, 4, 6$-fold rotations and the identity operation.
$\underline{C_I}$
The groups generated by the inversion and the identity operation.
$\underline{C_{nv}}$
The groups generated by $n = 2, 3, 4, 6$-fold rotations, reflections, and the identity operation. There are n reflection (mirror) planes parallel to the rotation axis with π/n period.
$\underline{C_{nh}}$
The groups generated by $n = 1, 2, 3, 4, 6$-fold rotations, a reflection, and the identity operation. There is a reflection (mirror) plane perpendicular to the rotation axis.
$\underline{S_n}$

The groups generated by $n = 4, 6$-fold rotoreflections and the identity operation. Because the groups generated by $n = 2, 3$-fold rotoreflections are equivalent to C_I and C_{3h}, we only use this notation for $n = 4, 6$.

$\underline{D_n}$
The groups generated by $n = 2, 3, 4, 6$-fold rotations and 2-fold rotations perpendicular to the n-fold rotation axis. There are n 2-fold rotations with π/n period.
$\underline{D_{nd}}$
The groups generated by combining the group D_n $(n = 2, 3)$ and n reflection planes between two 2-fold rotation axes.
$\underline{D_{nh}}$
The groups generated by combining the group D_n $(n = 2, 3, 4, 6)$ and the reflection plane perpendicular to the n-fold rotation axis.
$\underline{O, O_h}$
The group O is generated by rotations that preserve the octahedron symmetry [Fig.5.3]. The group O_h can be obtained by adding the inversion operation to the group O.
$\underline{T, T_h}$
The group T is generated by rotations that preserve the tetrahedron symmetry [Fig.5.3]. The group T_h can be obtained by adding the inversion operation to the group T.

5.4 Types of the Bravais lattices

As mentioned above, the periodic property of the system can be determined by giving the translation group $\{\boldsymbol{t_n}\}$, or equivalently, the Bravais lattice. The Bravais lattices are characterized by the lattice systems and the centering types. By considering the number and orders of the rotation axes, the lattice systems are classified into 7 types: cubic (O_h), tetragonal (D_{4h}), orthorhombic (D_{2h}), hexagonal (D_{6h}), rhombohedral (D_{3d}), monoclinic (C_{2h}), and triclinic (C_I). There are 5 centering types: primitive (P), base-centered (C, or sometimes A, B), body-centered (I), face-centered (F), and rhombohedral (R). By considering the compatibility between rotational symmetries and centering types, we obtain 14 types of the Bravais lattices [Fig. 5.4].

The crystal structures of materials can be obtained by adding a unit structure to each Bravais lattice point. If we just put an atom on each Bravais lattice point, then the crystal structure has the same symmetry as the Bravais lattice. Generally speaking, the symmetries of crystal structures for complicated unit structures are lower than those of the Bravais lattices.

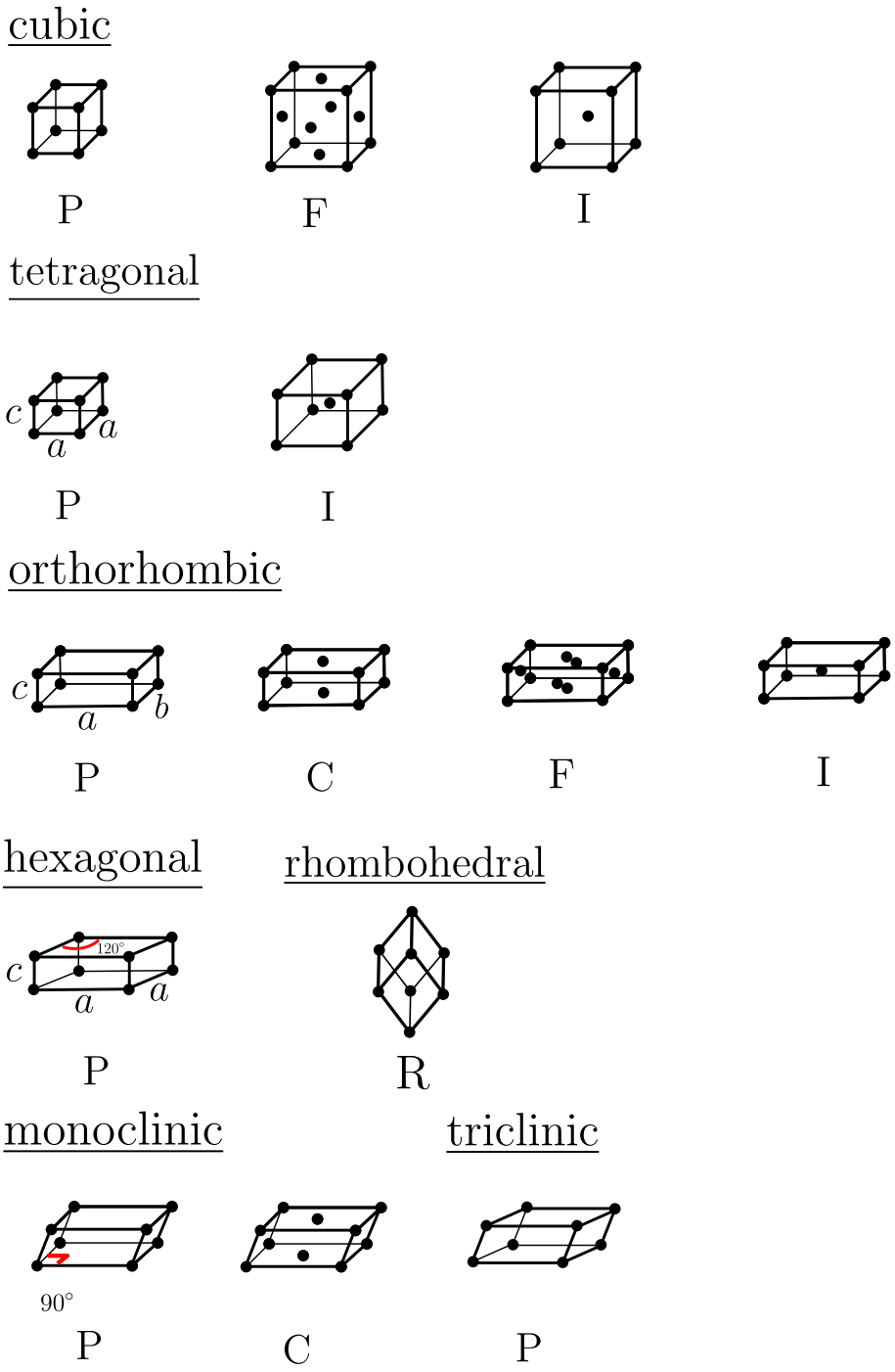

Figure 5.4: 14 types of the Bravais lattices. P, C, F, I, R denote primitive, base-centered, face-centered, body-centered, and rhombohedral, respectively.

5.5 Definition of space groups

We are now in a position to define the space group. In the above sections, we have introduced the symmetry operations that preserve the crystal structures. The set of such operations forms a group G, which is the so-called space group. There are 17 and 230 types of space groups in two and three dimensions, respectively. In the following, we mainly discuss three-dimensional crystals. For a given crystal structure, we can assign one of them. Since crystals should have the translation invariance by definition, the translation group T should be a subgroup of each space group. Actually, T should be also an invariant subgroup of each space group. Thus, G/T has a group structure.

The 230 space groups are classified into two categorys: symmorphic (73 types) and nonsymmorphic (157 types) space groups. In symmorphic space groups, the translation parts $\boldsymbol{b}$ of all elements can be set to be primitive lattice vectors by choosing an appropriate origin. In addition, the quotient group G/T can be chosen as the crystallographic point group, or equivalently, the symmorphic space group can be expressed as the **semidirect** product of the point group and the translation group. In other words, we can determine one symmorphic space group by giving the type of the Bravais lattice and crystallographic point group[2]. In nonsymmorphic space groups, the translation parts $\boldsymbol{b}$ of all elements cannot be set to be primitive lattice vectors simultaneously by choosing an appropriate origin. By definition, a nonsymmorphic space group contains at least one of nonsymmorphic operations (glides and screws).

5.6 Reciprocal lattice and Brillouin zone

In solid-state physics, we often consider a function $U(\boldsymbol{r})$ with the same periodicity as the Bravais lattice:

$$U(\boldsymbol{r}) = U(\boldsymbol{r} - \boldsymbol{t_n}). \tag{5.8}$$

It is convenient to express $U(\boldsymbol{r})$ in terms of the reciprocal lattice vectors $\boldsymbol{K_m}$:

$$U(\boldsymbol{r}) = \sum_{\boldsymbol{K_m}} U_{\boldsymbol{K_m}} \exp(i\boldsymbol{K_m} \cdot \boldsymbol{r}) \tag{5.9}$$

[2]In some cases, we should also consider the relative angle between the Bravais lattice and crystallographic point group.

where

$$\boldsymbol{K_m} = m_1\boldsymbol{K}_1 + m_2\boldsymbol{K}_2 + m_3\boldsymbol{K}_3 \ (m_i \in \mathbb{Z}),$$
$$\boldsymbol{K_1} = 2\pi\frac{\boldsymbol{t}_2 \times \boldsymbol{t}_3}{\boldsymbol{t}_1 \cdot (\boldsymbol{t}_2 \times \boldsymbol{t}_3)}, \boldsymbol{K_2} = 2\pi\frac{\boldsymbol{t}_3 \times \boldsymbol{t}_1}{\boldsymbol{t}_1 \cdot (\boldsymbol{t}_2 \times \boldsymbol{t}_3)}, \boldsymbol{K_3} = 2\pi\frac{\boldsymbol{t}_1 \times \boldsymbol{t}_2}{\boldsymbol{t}_1 \cdot (\boldsymbol{t}_2 \times \boldsymbol{t}_3)}. \quad (5.10)$$

These expressions can be derived by the periodicity condition for $U(\boldsymbol{r})$:

$$\exp(i\boldsymbol{K_m} \cdot \boldsymbol{t_n}) = 1. \quad (5.11)$$

The set $\{\boldsymbol{K_m}\}$ forms a lattice structure and is called as the reciprocal lattice. It is interesting to note that the centering types of the reciprocal lattices can be different from the Bravais lattice. The centering types of the reciprocal lattices for the face-centered and body-centered Bravais lattices are body-centered and face-centered, respectively, while those for the primitive and base-centered lattices are not changed.

A unit cell of the reciprocal space is also an important notion. Although there are a lot of choices, we usually choose it as the Brillouin zone because this respects the symmetry of the Bravais lattices. The Brillouin zone is defined as the region surrounded by the perpendicular bisector planes between the origin and reciprocal lattice points next to the origin.

The types of the Brillouin zones are determined by specifying not the space groups but the Bravais lattices. 14 types of the Brillouin zones are drawn in Figs. 5.5, 5.6, 5.7.

5.7 Momentum space in solid-state physics

Under the continuous translation symmetry, momentum is a good quantum number and plays a central role in physics. Although this symmetry is broken in crystals, they still have the discrete translation symmetry. By considering this discrete symmetry, we can define the similar notion as the momentum: the crystal momentum. In this section, we define the crystal momentum in terms of the representation theory.

Because discrete translations generated by $\boldsymbol{t}_i$ commute each other, translation group T can be written as the direct product

$$T = T_1 \times T_2 \times T_3, \quad (5.12)$$

where T_i is the group whose elements are $\{\epsilon|n_i\boldsymbol{t}_i\}$. Under the periodic boundary condition imposed above, T_i are the cyclic groups of order N. The irreducible

cubic

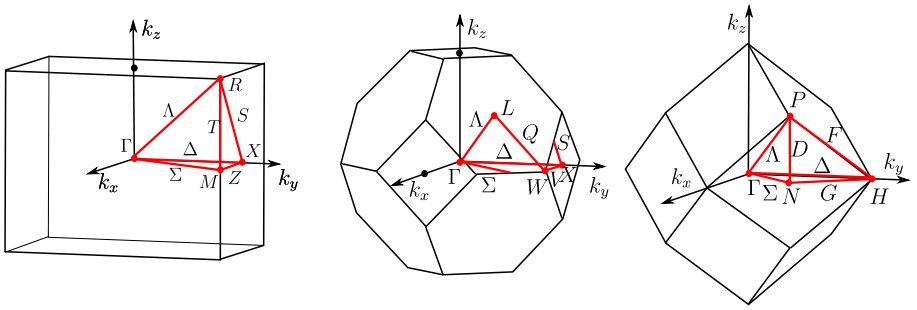

P F I

tetragonal

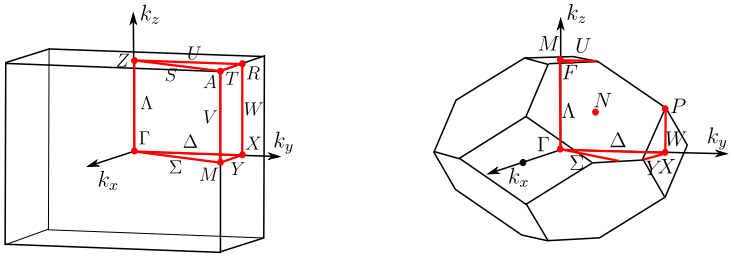

P I

Figure 5.5: Brillouin zones for cubic and tetragonal lattices.

orthorhombic

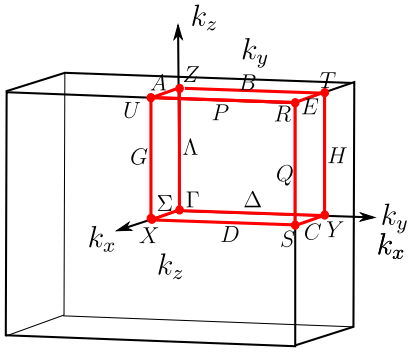

P

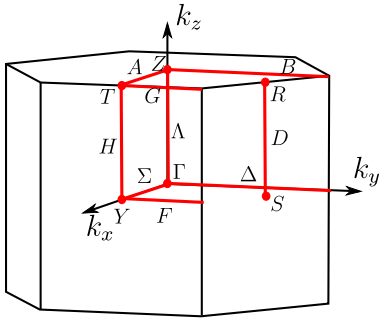

C

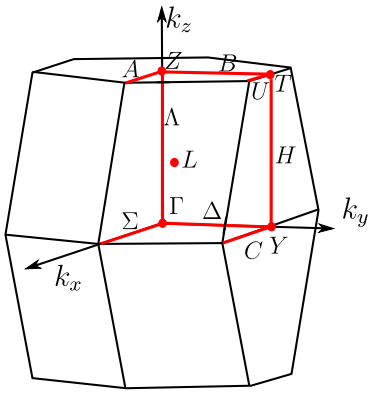

F

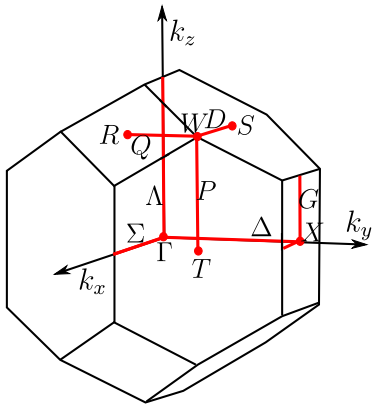

I

Figure 5.6: Brillouin zones for orthorhombic lattices.

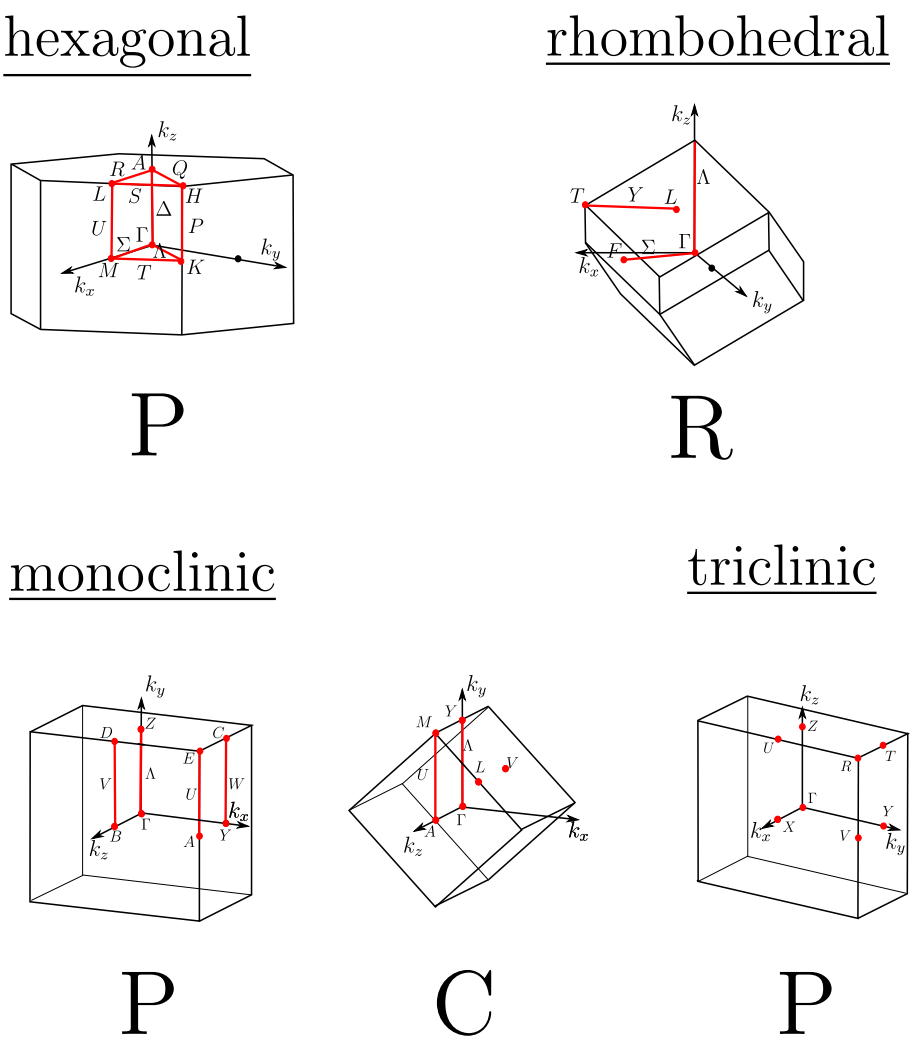

Figure 5.7: Brillouin zones for hexagonal, rhombohedral, monoclinic, and triclinic lattices.

representations of the cyclic group are given by one-dimensional representations with the characters

$$\chi_{p_i}(\{\epsilon|\boldsymbol{t}_i\}) = \exp(\frac{2\pi i p_i}{N}), \tag{5.13}$$

where p_i are integers. Using the properties of the direct product, we obtain the representations of T, which are also one-dimensional representations, with the characters

$$\chi_{\boldsymbol{k}}(\{\epsilon|\boldsymbol{t_n}\}) = \exp(i\boldsymbol{k}\cdot\boldsymbol{t_n}), \tag{5.14}$$

where

$$\boldsymbol{k} = \frac{p_1\boldsymbol{K}_1 + p_2\boldsymbol{K}_2 + p_3\boldsymbol{K}_3}{N}. \tag{5.15}$$

Thus, the representations are labeled by the three-dimensional vectors $\boldsymbol{k}$, which are so-called the crystal momentum. According to Eqs. (5.11) and (5.14), the characters do not change under the translation $\boldsymbol{k} \to \boldsymbol{k} + \boldsymbol{K_m}$, and the representation with $\boldsymbol{k}$ is the same as that with $\boldsymbol{k} + \boldsymbol{K_m}$. To avoid this duplication, we usually limit $\boldsymbol{k}$ in the Brillouin zone.

5.8 Space group and topological physics

Recently, the space group symmetry is one of the key ingredients in topological physics. Although the conventional topological physics is not directly related to the spin texture problem in this thesis, it would give some insight into the role of space group symmetries in recent physics. In addition, it may be interesting for readers to compare the problem of a spin vector field on momentum space (this thesis) with that of the Bloch wave function on it. We first briefly review the recent developments in topological physics. Then we introduce topological physics under the space group symmetries.

5.8.1 Topological condensed matter physics

The earliest example of topological quantum phenomena in condensed matter physics is the integer quantum Hall effect [72], which is realized in two-dimensional electron systems under a strong magnetic field. In this phenomenon, the Hall conductivity is quantized, and electrons flow only in the edges of the sample. Mathematically, the Hall conductivity for this phenomenon is formulated as the Chern number defined for a $U(1)$ gauge structure of the wave function on

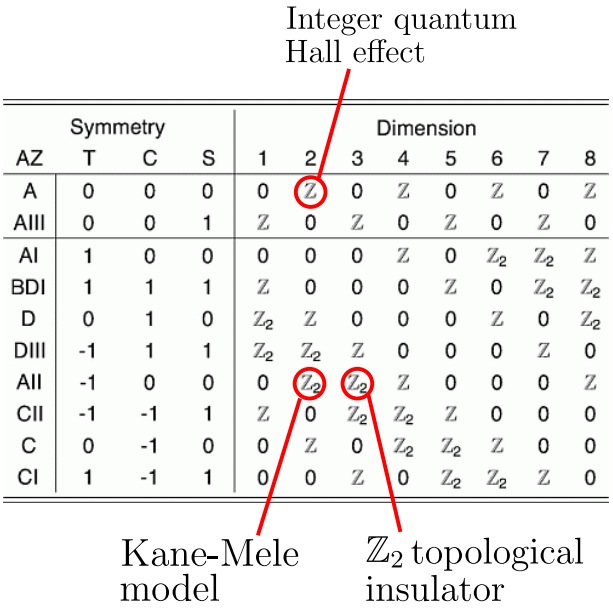

	Symmetry			Dimension							
AZ	T	C	S	1	2	3	4	5	6	7	8
A	0	0	0	0	$\mathbb{Z}$	0	$\mathbb{Z}$	0	$\mathbb{Z}$	0	$\mathbb{Z}$
AIII	0	0	1	$\mathbb{Z}$	0	$\mathbb{Z}$	0	$\mathbb{Z}$	0	$\mathbb{Z}$	0
AI	1	0	0	0	0	0	$\mathbb{Z}$	0	$\mathbb{Z}_2$	$\mathbb{Z}_2$	$\mathbb{Z}$
BDI	1	1	1	$\mathbb{Z}$	0	0	0	$\mathbb{Z}$	0	$\mathbb{Z}_2$	$\mathbb{Z}_2$
D	0	1	0	$\mathbb{Z}_2$	$\mathbb{Z}$	0	0	0	$\mathbb{Z}$	0	$\mathbb{Z}_2$
DIII	-1	1	1	$\mathbb{Z}_2$	$\mathbb{Z}_2$	$\mathbb{Z}$	0	0	0	$\mathbb{Z}$	0
AII	-1	0	0	0	$\mathbb{Z}_2$	$\mathbb{Z}_2$	$\mathbb{Z}$	0	0	0	$\mathbb{Z}$
CII	-1	-1	1	$\mathbb{Z}$	0	$\mathbb{Z}_2$	$\mathbb{Z}_2$	$\mathbb{Z}$	0	0	0
C	0	-1	0	0	$\mathbb{Z}$	0	$\mathbb{Z}_2$	$\mathbb{Z}_2$	$\mathbb{Z}$	0	0
CI	1	-1	1	0	0	$\mathbb{Z}$	0	$\mathbb{Z}_2$	$\mathbb{Z}_2$	$\mathbb{Z}$	0

Figure 5.8: Altland-Zirnbauer classification (table from Ref. [77]).

two-dimensional torus representing magnetic Brillouin zone. This is the celebrated TKNN formula [70, 71]. The Chern number detects the non-triviality of the $U(1)$ bundle on the two-dimensional torus [64]. It is well known that the non-triviality of this bundle is characterized by $\mathbb{Z}$. Interestingly, this integer (Chern number) corresponds to the number of edge states of the sample. This fact is the so-called bulk-edge correspondence [73].

Haldane generalized the quantum Hall effect to the electron systems without a net magnetic field [74]. Thanks to the absence of the magnetic field, there is a translation invariance, and we can discuss the physics in terms of momentum space. In this generalization, the Hall conductivity is formulated as the Chern number defined for a $U(1)$ gauge structure of the Bloch wave function on two-dimensional Brillouin zone, which is mathematically nothing but a two-dimensional torus. The important point here is that the gauge structure of Bloch wave functions on the Brillouin zone determines the transport of the system, while this thesis focuses on the properties of the tangent vector bundle defined on momentum space. In any case, considering the topological concepts defined on momentum space is the starting point of the recent developed topological condensed matter physics.

By changing the dimensionality and adding symmetries, we can construct the celebrated topological insulators and superconductors [5, 6]. Mathematically,

the topological classification is performed by classifying vector bundles on n-dimensional torus that satisfy the symmetry constraints. Kitaev gave the explicit way of classifying the topological phases by using the K-theory [75]. According to the K-theory classification for time-reversal, particle-hole, and chiral symmetries, topological phases of non-interacting (or mean-field) electron systems correspond to the Altland Zirnbauer (AZ) classes (Fig. 5.8) [75, 76, 77]. The integer quantum Hall effect corresponds to the class A in two dimensions. Note that the types of topological invariants are not only $\mathbb{Z}$ but also $\mathbb{Z}_2$. The Kane-Mele [78] model and three-dimensional $\mathbb{Z}_2$ topological insulator [79] are the good examples labeled by nontrivial $\mathbb{Z}_2$ indices [Fig. 5.8].

5.8.2 Topological phases protected by space group symmetries

Natural generalizations of topological insulators and superconductors to space group symmetries are called topological crystalline insulators and superconductors [80, 81, 82]. Topological crystalline materials are protected by new topological invariants related to the space group symmetries. For a non-zero crystalline topological invariant, there can exist the edge (surface) modes on boundaries that possess the corresponding crystalline symmetries even for trivial materials in the AZ classification. The typical example is the mirror Chern number [83] defined on the mirror-invariant planes in the Brillouin zone. The classification theory can be constructed by using the K-theory for several space group symmetries [84, 85, 86]. Classifying topological phases and calculating topological invariant for all space groups are still open questions.

Another interesting direction of this field is the classification theory based on the notion of atomic insulators [87, 88]. Atomic insulators are the materials that can be adiabatically connected to the isolated atoms. In this framework, the non-triviality is defined by the difference from the atomic insulators. We first investigate all possible combinations of representations at symmetric parts of Brillouin zone, which should satisfy the compatibility relations [68], for given space group symmetries and define the set $\{\mathrm{BS}\}$. Then we investigate those of representations for atomic insulators and define the set $\{\mathrm{AI}\}$. The classification for the space group is given by the quotient space

$$X_{BS} = \frac{\{\mathrm{BS}\}}{\{\mathrm{AI}\}}, \tag{5.16}$$

which is always a finite Abelian group. Although the mathematics is simpler than the conventional classification theories, the relation between this framework and the conventional topological classification theories is unclear. For instance, the

classification for the $\mathbb{Z}_2$ topological insulator is given by $\mathbb{Z}_4$ in this framework. Complete understanding of the topological classification under the space group is an important remaining issue.

The topological properties of matters are affected by the space group symmetries. Under the space group symmetries, such properties can be often determined by the information of symmetric parts of the Brillouin zone. In this thesis, those parts correspond to the singular parts of orbifolds. The topological classification theory based on the orbifold would be an interesting future work.

Chapter 6

Basics of orbifold

In this chapter, we first introduce the notion of the orbifold [89, 90], which is a simple generalization of the notion of the manifold. Then we consider the orbifolds for the space group symmetries and introduce related notions. Although these orbifolds are not defined for momentum space, they are useful for understanding the momentum space orbifolds in the later chapters. The following discussions are based on Ref. [89].

6.1 Definition and examples

In this section, we first give the definition of the orbifold and then list some famous examples in this field.

6.1.1 Rough definition

We here give a rough definition of the orbifold. The orbifold is a simple generalization of the manifold. Remember the definition of the manifold. Roughly speaking, the d-dimensional manifold is a space that locally looks like the Euclidean space $\mathbb{E}^d$ [63, 64]. This statement is the starting point for defining the orbifold.

The orbifold is locally isometric with a quotient space $\mathbb{E}^d/\Gamma$, where Γ is an isometric finite group of the Euclidean space[1]. Γ can depend on a point on the orbifold. If Γ is just $\{e\}$ for the whole region, the orbifold is reduced to the manifold. In that sense, the notion of manifold is included in the definition of the orbifold. The most important difference from the manifold is that there can be singularities in the case of the orbifold. The points whose neighborhoods are

[1]We can also cosinder the orbifold for general metric spaces other than the Euclidean space

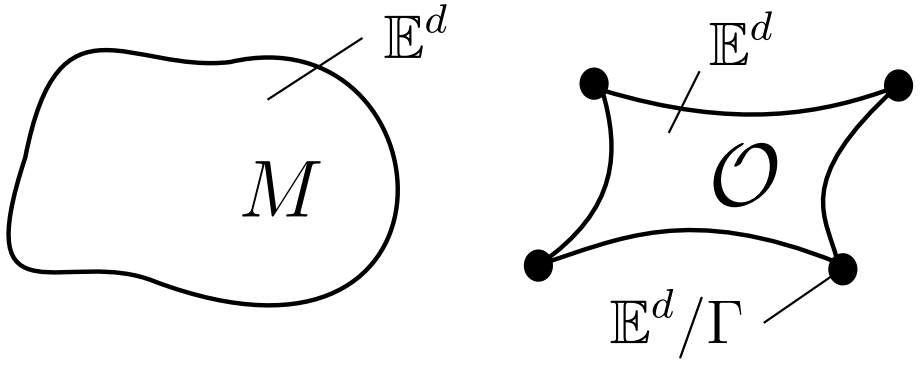

Figure 6.1: Schematic pictures of the manifold and orbifold. The orbifold can have singularities, while the manifold cannot.

characterized by $\Gamma \neq \{e\}$ are singular points. If such points are not isolated, we call them singular lines, planes, and so on. The order of singularity is defined as $|\Gamma|$. The schematic pictures of a manifold and an orbifold are shown in Fig. 6.1

When the quotient space X/G, where X is a set and G a group acting on X, is a metric space, then X/G is also called the orbit space. The orbifold locally looks like $\mathbb{E}^d/\Gamma$, which is an orbit space. The *orbifold* is named after the orbit space and manifold.

6.1.2 Formal definition

For readers who want to know the formal definition of the orbifold, we here give it. A d-dimensional metric space $\mathcal{O}$ is an orbifold with the model X if $\mathcal{O}$ is a union of open sets U_i $(i \in I)$ satisfying the following conditions:

- There are $\tilde{U}_i$ $(i \in I)$: an open set expressed as the neighborhood of a point on X, a continuous map $p_i : \tilde{U}_i \to U_i$, and a finite group G_i that consists of isometric transformations of X acting on $\tilde{U}_i$, and p_i leads to an isometry

$$\tilde{U}_i/G_i \to U_i.$$

- If $p_i(x_i) = p_j(x_j)$ for x_i on $\tilde{U}_i$ and x_j on $\tilde{U}_j$, there are an open set $\tilde{V}_i$ on $\tilde{U}_i$, an open set $\tilde{V}_j$ on $\tilde{U}_j$, and an isometry $\phi_{ij} : \tilde{V}_i \to \tilde{V}_j$ satisfying

$$p_j \circ \phi_{i,j}(x) = p_i(x)$$

  for all $x \in \tilde{V}_i$.

If we set $X = \mathbb{E}^d$, $\mathcal{O}$ is a Euclidean orbifold discussed in the rough definition.

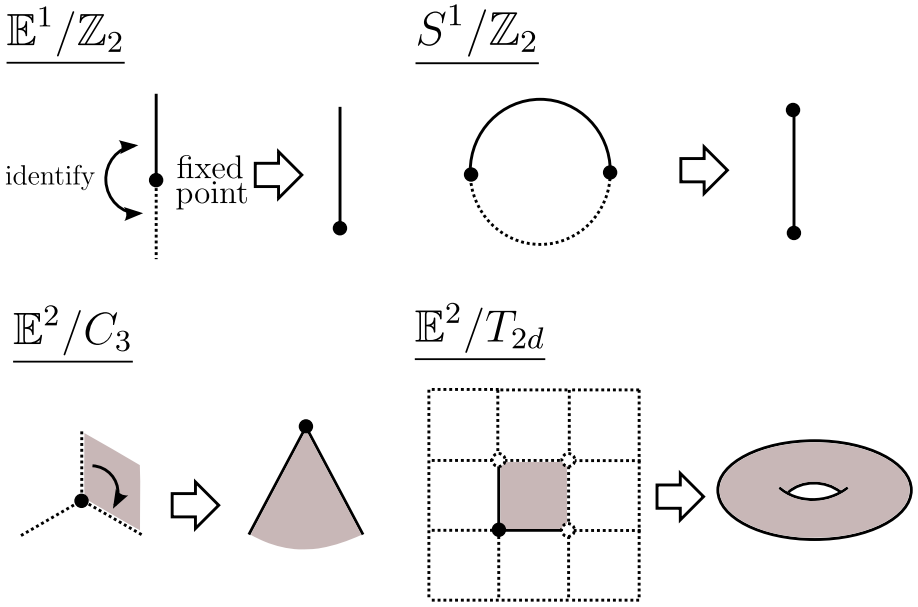

Figure 6.2: Several examples of orbifolds.

6.1.3 Examples

We here give some simple examples of the orbifold [Fig. 6.2].

$\mathbb{E}^1/\mathbb{Z}_2$
One of the simplest examples of the orbifolds is $\mathbb{E}^1/\mathbb{Z}_2$. This is just obtained by identifying x and $-x$ on a number line. Since this operation does not change $x = 0$, $x = 0$ is the fixed point. In the context of orbifolds, it is also called as a singular point with order $|\Gamma| = 2$. The neighborhoods for $x \neq 0$ are isometric with the neighborhood of a point on $\mathbb{E}^1$, while the neighborhood for $x = 0$ is isometric to the neighborhood of the origin at $\mathbb{E}^1/\mathbb{Z}_2$.

$\mathbb{S}^1/\mathbb{Z}_2$
The orbifold $\mathbb{S}^1/\mathbb{Z}_2$ is a good example for condensed matter physicists. Let us consider the one-dimensional Brillouin zone under the inversion symmetry. This orbifold corresponds to the irreducible part of the Brillouin zone. In this case, $x = 0, \pi$ are the fixed points under the inversion, and they correspond to the singular points of the orbifold. The neighborhoods for $x \neq 0, \pi$ are isometric with the neighborhood of a point on $\mathbb{E}^1$, while the neighborhoods for $x = 0, \pi$ are isometric with the neighborhood of the origin at $\mathbb{E}^1/\mathbb{Z}_2$.

$\underline{\mathbb{E}^2/C_n}$
Another typical example is $\mathbb{E}^2/C_n$, where C_n is the point group that consists of n-fold rotations defined in Chap. 5. This orbifold takes the conical structure whose singular point has the order n. The $n = 3$ case is drawn in Fig. 6.2.

$\underline{\mathbb{E}^2/T_{2d}}$
$\mathbb{E}^2/T_{2d}$ is equivalent to the torus $\mathbb{T}^2$, where T_{2d} is the two-dimensional translation group. Since there are no singular points, it is also a manifold. This is an important example in condensed matter physics. The two-dimensional Brillouin zone is obtained by identifying $\boldsymbol{k}$ and $\boldsymbol{k} + \boldsymbol{K_m}$ of the momentum space. Since $\{\boldsymbol{K_m}\}$ is a translation group in momentum space, the Brillouin zone can be regarded as $\mathbb{E}^2/T_{2d}$.

6.2 Related notions of orbifold

For convenience in later sections, we here introduce some important notions.

6.2.1 Euler characteristic versus orbifold Euler characteristic

The Euler characteristic is a topological invariant of a topological space. In the case of orbifold, there is a similar quantity: the orbifold Euler characteristic. Both of them are important in the later chapters. We here define the orbifold Euler characteristic and compute it for some examples.

The orbifold Euler characteristic can be computed by considering the cell decomposition introduced in Chap. 4. In the cell decomposition, the singular points, lines, planes,$\cdots$ should be taken as the 0-, 1-, 2-, $\cdots$ dimensional cells. Once we obtain the cell decomposition of the orbifold, we can calculate the orbifold Euler characteristic in almost the same procedure as the calculation of the Euler characteristic. The only difference is that we should assign the weight for each singular part. Suppose that the i-th cell is described by $\mathbb{E}^{d_i}/\Gamma_i$, where d_i is the dimension of the i-th cell, and Γ_i is the isometric finite group that characterizes the i-th cell. The explicit form of the orbifold Euler characteristic is given by

$$\chi^{orb}(\mathcal{O}) = \sum_i (-1)^{d_i} \frac{1}{|\Gamma_i|}, \tag{6.1}$$

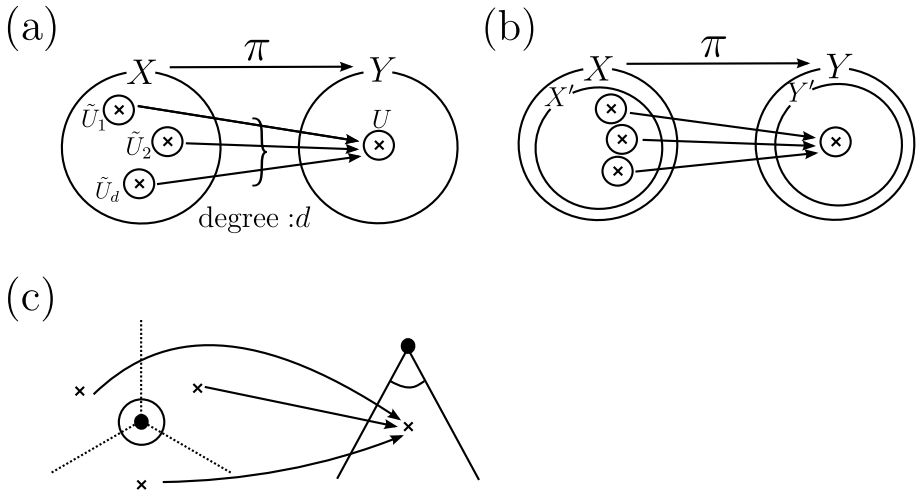

Figure 6.3: Schematic pictures of (a) covering map, (b) branched covering, and (c) a branched covering $\mathbb{E}^2 \to \mathbb{E}^2/C_3$.

where $|\Gamma_i|$ is the order of Γ_i. The sum is taken over all cells in the cell decomposition of the orbifold. If Γ_i are $\{e\}$ for all cells, then $\chi^{orb}(\mathcal{O}) = \chi(\mathcal{O})$.

As an example of the calculation, we here compute the Euler characteristic and orbifold Euler characteristic of $S^1/\mathbb{Z}_2$ shown in Fig. 6.2. The picture of $S^1/\mathbb{Z}_2$ itself is a cell decomposition of $S^1/\mathbb{Z}_2$. There are two 0-dimensional cells and one 1-dimensional cell. Thus, the Euler characteristic is

$$\chi(S^1/\mathbb{Z}_2) = (+1) \times 2 - 1 = 1. \tag{6.2}$$

Next, we consider the weight for each cell. The 0-cells are described by $\mathbb{E}^1/\mathbb{Z}_2$, while the 1-cell is described by $\mathbb{E}^1$. Thus, the orbifold Euler characteristic is

$$\begin{aligned} \chi^{orb}(S^1/\mathbb{Z}_2) &= (+1)\frac{1}{|\mathbb{Z}_2|} \times 2 + (-1) \\ &= \frac{1}{2} \times 2 - 1 = 0. \end{aligned} \tag{6.3}$$

Note that these quantities are only defined for compact orbifolds.

6.2.2 Covering map versus branched covering

Another important notion in the field of the orbifold is the branched covering. Before defining it, we first review the covering map [Fig. 6.3 (a)].

Let X and Y be metric spaces. A continuous map $\pi : X \to Y$ is a covering map if there is a neighborhood U for any point of Y satisfying the following conditions:

- The inverse mapping π^{-1} of U is expressed as

$$\pi^{-1}(U) = \bigcup_{i \in I} \tilde{U}_i,$$

  where $\tilde{U}_i$ are open sets of X that have no intersections.

- $\pi|_{\tilde{U}_i} : \tilde{U}_i \to U_i$ is an isometry.

If $\pi^{-1}(y)$ for any $y \in Y$ is composed of d points in X, π is called as a covering map with the degree d.

In the field of the orbifold, it is convenient to define the branched covering [Fig. 6.3 (b) and (c)]. Let us consider the projection map $\pi : \mathbb{E}^2 \to \mathbb{E}^2/C_n$. Except for the fixed (singular) points of the n-fold rotation, this map is a covering map with the degree n. In this case, π is not a covering map but a branched covering with the degree n. In general, a continuous map $\pi : X \to Y$ is a branched covering if $\pi' : X' \to Y'$ is a covering map, where $Y' = Y \backslash S$, $X' = \pi^{-1}(Y')$, and $S \neq Y$ is a closed set of Y. In the context of the orbifold, S is the set of all singular parts.

6.3 Orbifold and space group

The space groups can be reinterpreted in terms of the orbifold [91]. Let Γ be a discrete subgroup of the group of isometry defined in the d-dimensional Euclidean space. If the orbifold $\mathbb{E}^d/\Gamma$[2] is compact, then Γ is called as a space group. The number of such compact orbifolds is 17 in two dimensions and 230 in three dimensions, which correspond to the numbers of space groups explained in Chap. 5.

Let us see some examples. $\mathbb{E}^2/T_{2d}$ is equivalent to the two-dimensional torus, and it is compact. Thus, the two-dimensional translation group T_{2d} is a space group. $\mathbb{E}^2/C_3$ has a conical structure, and it is not compact (Fig. 6.2). Thus, C_3 is not a space group by itself. Since C_3 is a crystallographic point group, we can construct a space group by combining C_3 and T_{2d}.

We here describe two theorems about the relation between the space groups and orbifolds.

[2]We here omit proving that $\mathbb{E}^d/\Gamma$ has an orbifold structure.

Theorem 1

Let Γ be a space group. Then a continuous map $\pi : \mathbb{T}^n \to \mathbb{E}^n/\Gamma$ is a branched covering with finite degree.

We omit the proof here. By using this theorem, we can prove the following theorem.

Theorem 2

Let Γ be a space group. Then the orbifold Euler characteristic of orbifold $\mathbb{E}^n/\Gamma$ is given by

$$\chi^{orb}(\mathbb{E}^n/\Gamma) = 0.$$

Proof. According to the theorem 1, $\mathbb{T}^n \to \mathbb{E}^n/\Gamma$ is a branched covering with finite degree. Suppose that the degree is d. We first take a cell decomposition of $\mathbb{E}^n/\Gamma$. By acting Γ to the cell decomposition, we obtain a cell decomposition of the Euclidean space $\mathbb{E}^n$. Simultaneously, we also obtain the cell decomposition of the torus as the unit cell corresponding to the translation group in Γ. For non-singular parts, one m-dimensional cell in $\mathbb{E}^n/\Gamma$ corresponds to d m-dimensional cells in $\mathbb{T}^n$. For a m-dimensional singular part described by $\mathbb{E}^m/\Gamma_i$, one m-dimensional cell in $\mathbb{E}^n/\Gamma$ corresponds to $d/|\Gamma_i|$ m-dimensional cells in $\mathbb{T}^n$. By considering the definition of the orbifold Euler characteristic, we obtain

$$\chi(\mathbb{T}^n) = d\chi^{orb}(\mathbb{E}^n/\Gamma).$$

Since the Euler characteristic of n-dimensional torus is 0, we obtain

$$\chi^{orb}(\mathbb{E}^n/\Gamma) = 0.$$

□

Before ending this chapter, we give some examples of two-dimensional space group (or wallpaper group) orbifolds (Fig. 6.4).

T

This orbifold corresponds to the two-dimensional translation group T_{2d}. This orbifold is also expressed as $\mathbb{E}^2/T_{2d}$, which is equivalent to the two-dimensional torus as discussed above.

S333

This orbifold corresponds to the space group that consists of 3-fold rotations and the two-dimensional translation. A map $\pi : T \to S333$ is a branched covering

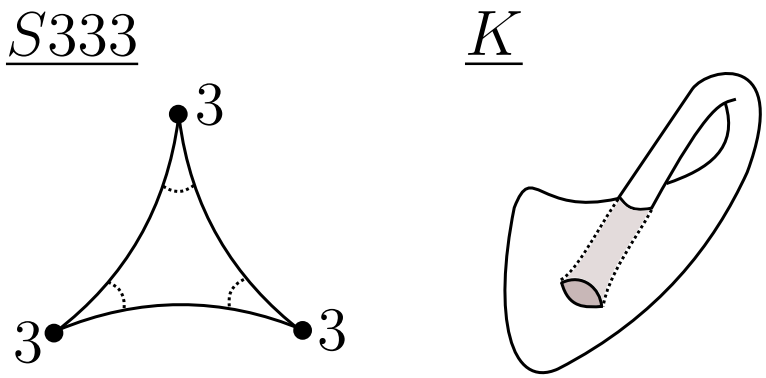

Figure 6.4: Schematic pictures of two-dimensional space group orbifolds.

with degree 3. There are three singular points with $|\Gamma_i| = 3$.

K
This orbifold corresponds to the space group that consists of the glide operation and the two-dimensional translation. This orbifold is equivalent to the Klein bottle, which is a typical example of unoriented manifolds. Since there are no singular points, a map $\pi : T \to K$ is a covering map with degree 2.

Chapter 7

Momentum space as orbifold

In Chap. 6, the space group orbifolds have been introduced in terms of symmetry operations that act on real space. For our purpose, it is more convenient to discuss the space group symmetries in terms of momentum space. We here regard the irreducible part of the momentum space under the space group symmetries as an orbifold. In this context, the problem of spin textures in momentum space can be regarded as the (pseudo-)vector field on the "momentum space orbifold". In addition to the space group symmetries, we also consider the time-reversal symmetry, which is a typical symmetry in condensed matter physics. In this chapter, we explain the basics of the momentum space orbifold.

7.1 Symmetric operations in momentum space

In this chapter, we explain how the space group and time-reversal symmetries act on the crystal momentum and electron spin, which is a pseudovector.

7.1.1 Spin as a pseudovector

Let us consider physical quantities in three dimensions. A pseudovector is a quantity that transforms like a vector under the proper rotations ($\in SO(3)$), while the sign of it is changed under the improper rotations ($\notin SO(3), \in O(3)$). For instance, the determinant of the θ-rotation around z-axis is

$$\det \begin{pmatrix} \cos\theta & -\sin\theta & 0 \\ \sin\theta & \cos\theta & 0 \\ 0 & 0 & 1 \end{pmatrix} = 1, \tag{7.1}$$

and the θ-rotation is a proper rotation. Under the θ-rotation, a pseudovector is rotated by the same matrix for the coordinate. On the other hand, the determi-

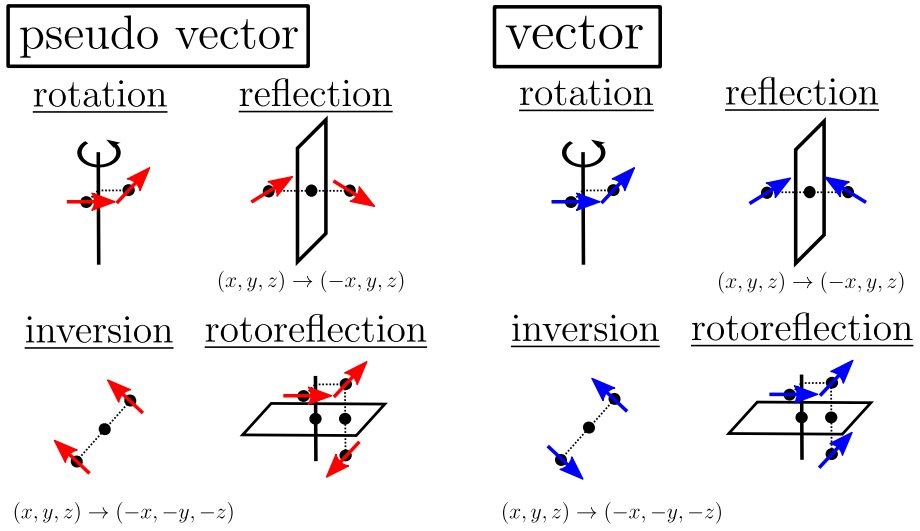

Figure 7.1: Schematic pictures of symmorphic operations for pseudovector and vector.

nant of the inversion is

$$\det \begin{pmatrix} -1 & 0 & 0 \\ 0 & -1 & 0 \\ 0 & 0 & -1 \end{pmatrix} = -1, \tag{7.2}$$

and the inversion is an improper rotation. Under the inversion, a pseudovector is not changed in the original coordinate. In general, the rotation matrix for a pseudovector can be obtained by multiplying the rotation matrix for the coordinate and

$$\begin{pmatrix} -1 & 0 & 0 \\ 0 & -1 & 0 \\ 0 & 0 & -1 \end{pmatrix}. \tag{7.3}$$

Typical examples of pseudovectors in physics are the magnetic field and angular momenta. Spin angular momentum, a typical angular momentum in condensed matter physics, behaves as a pseudovector. In Fig. 7.1, we draw schematic pictures of behaviors of a pseudovector under the symmorphic operations. The spin operator in quantum mechanics is transformed as follows:

$$U_\alpha^{-1} \hat{S}^i U_\alpha = \alpha'_{ij} \hat{S}^j, \tag{7.4}$$

where U_α is a unitary matrix that represent the α rotation of the quantum system, and α' is a rotation matrix for a pseudovector. $\alpha' = \alpha$ for proper rotations, while $\alpha' = -\alpha$ for improper rotations.

7.1.2 Space group operations for momentum and spin

We here explain how the crystal momentum and spin behave under the space group symmetries. For the crystals, we often consider a function $\phi_{\boldsymbol{k}}$, which is an irreducible representation of the translation group labeled by the crystal momentum $\boldsymbol{k}$, such as the Bloch wave function. Under the translation $\{\epsilon|\boldsymbol{t_n}\}$, $\phi_{\boldsymbol{k}}$ behaves as

$$\{\epsilon|\boldsymbol{t_n}\}\phi_{\boldsymbol{k}} = \exp(i\boldsymbol{k}\cdot\boldsymbol{t_n})\phi_{\boldsymbol{k}}. \tag{7.5}$$

In other words, this equation is the condition for $\phi_{\boldsymbol{k}}$ to be an irreducible representation of the translation group.

Let us consider the function $\{\alpha|\boldsymbol{b}\}\phi_{\boldsymbol{k}}$. This function is an irreducible representation of the translation group labeled by $\alpha\boldsymbol{k}$. This can be easily checked:

$$\begin{aligned}
\{\epsilon|\boldsymbol{t_n}\}\{\alpha|\boldsymbol{b}\}\phi_{\boldsymbol{k}} &= \{\alpha|\boldsymbol{b}\}\{\epsilon|\alpha^{-1}\boldsymbol{t_n}\}\phi_{\boldsymbol{k}} \\
&= \exp(i\boldsymbol{k}\cdot\alpha^{-1}\boldsymbol{t_n})\{\alpha|\boldsymbol{b}\}\phi_{\boldsymbol{k}} \\
&= \exp(ik_i(\alpha^{-1})_{ij}(t_{\boldsymbol{n}})_j)\{\alpha|\boldsymbol{b}\}\phi_{\boldsymbol{k}} \\
&= \exp(ik_i(\alpha)_{ji}(t_{\boldsymbol{n}})_j)\{\alpha|\boldsymbol{b}\}\phi_{\boldsymbol{k}} \\
&= \exp(i\alpha\boldsymbol{k}\cdot\boldsymbol{t_n})\{\alpha|\boldsymbol{b}\}\phi_{\boldsymbol{k}},
\end{aligned} \tag{7.6}$$

where we have used $\alpha^{-1} = \alpha^t$. Thus, the crystal momentum behaves as a vector under a rotation α. The translation part of $\{\alpha|\boldsymbol{b}\}$ does not affect the momentum.

Next, we investigate the electron spin. In the following, we assume that electron systems can be described by one-particle picture, and electron states are well expressed as the Bloch wave functions $|\boldsymbol{k}, a\rangle$. As defined in Chap. 1, the electron spin is given by

$$\boldsymbol{S}_{\boldsymbol{k},a} \equiv \langle \boldsymbol{k}, a|\hat{\boldsymbol{S}}|\boldsymbol{k}, a\rangle, \tag{7.7}$$

where $\hat{\boldsymbol{S}} = \hat{\boldsymbol{\sigma}}/2 \otimes \hat{1}$ with $\hat{\sigma^i}$ being the Pauli matrices in spin space and $\hat{1}$ the identity matrix in orbit space. Under the space group symmetry $\{\alpha|\boldsymbol{b}\}$, the spin behaves as

$$\begin{aligned}
\langle \boldsymbol{k}, a|U^{-1}_{\{\alpha|\boldsymbol{b}\}}\hat{S}^i U_{\{\alpha|\boldsymbol{b}\}}|\boldsymbol{k}, a\rangle &= \langle \boldsymbol{k}, a|U_\alpha^{-1}U_{\boldsymbol{b}}^{-1}\hat{S}^i U_{\boldsymbol{b}}U_\alpha|\boldsymbol{k}, a\rangle \\
&= \langle \boldsymbol{k}, a|U_\alpha^{-1}\hat{S}^i U_\alpha|\boldsymbol{k}, a\rangle \\
&= \alpha'_{ij}\langle \boldsymbol{k}, a|\hat{S}^i|\boldsymbol{k}, a\rangle \\
&= \alpha'_{ij}S^j_{\boldsymbol{k},a},
\end{aligned} \tag{7.8}$$

where U_x denotes the representation matrix of the symmetry operation x. In the second line, we have used the fact that the translation does not change the

spin. In the third line, we have used Eq.(7.4). We implicitly assume that there is no spin degeneracy for a band a, and $\boldsymbol{S}_{\boldsymbol{k},a}$ is well defined. In summary, the momentum and spin behave under the space group symmetry $\{\alpha|\boldsymbol{b}\}$ as

$$\begin{aligned} \boldsymbol{k} &\to \alpha\boldsymbol{k}, \\ \boldsymbol{S}_{\boldsymbol{k},a} &\to \boldsymbol{S}_{\alpha\boldsymbol{k},a} \equiv \alpha' \boldsymbol{S}_{\boldsymbol{k},a}. \end{aligned} \tag{7.9}$$

This means that non-primitive lattice translation does not affect momentum and spin directly.

7.1.3 Time-reversal symmetric operations for momentum space

In the absence of magnetic field and magnetic orders, electron systems possess the time-reversal symmetry. Under the time-reversal symmetry, momentum operator $\hat{\boldsymbol{P}}$, orbital angular momentum operator $\hat{\boldsymbol{L}}$, and spin operator $\hat{\boldsymbol{S}}$ behave as [68, 92]

$$\begin{aligned} T^{-1}\hat{\boldsymbol{P}}T &= -\hat{\boldsymbol{P}}, \\ T^{-1}\hat{\boldsymbol{L}}T &= -\hat{\boldsymbol{L}}, \\ T^{-1}\hat{\boldsymbol{S}}T &= -\hat{\boldsymbol{S}}, \end{aligned} \tag{7.10}$$

where T is the time-reversal operator expressed as an antiunitary operator ($T^\dagger = -T^{-1}$). The crystal momentum changes its sign under the time-reversal operation. This can be easily checked by using $\{\epsilon|\boldsymbol{t_n}\} = \exp(i\hat{\boldsymbol{P}}\cdot\boldsymbol{t_n})$:

$$\begin{aligned} \{\epsilon|\boldsymbol{t_n}\}T\phi_{\boldsymbol{k}} &= \exp(i\hat{\boldsymbol{P}}\cdot\boldsymbol{t_n})T\phi_{\boldsymbol{k}} \\ &= T\exp(i\hat{\boldsymbol{P}}\cdot\boldsymbol{t_n})\phi_{\boldsymbol{k}} \\ &= T\exp(i\boldsymbol{k}\cdot\boldsymbol{t_n})\phi_{\boldsymbol{k}} \\ &= \exp(-i\boldsymbol{k}\cdot\boldsymbol{t_n})T\phi_{\boldsymbol{k}}, \end{aligned} \tag{7.11}$$

where we have used Eq. (7.10) and $iT = -Ti$ [68]. Thus, $T\phi_{\boldsymbol{k}}$ is an irreducible representation of the translation group labeled by $-\boldsymbol{k}$. The electron spin also changes its sign under the time-reversal symmetry:

$$\langle \boldsymbol{k}, a|T^{-1}\hat{S}^i T|\boldsymbol{k}, a\rangle = -\langle \boldsymbol{k}, a|\hat{S}^i|\boldsymbol{k}, a\rangle, \tag{7.12}$$

where we have used Eq. (7.10).

In summary, the momentum and electron spin behave under the time-reversal symmetry T as

$$\begin{aligned} \boldsymbol{k} &\to -\boldsymbol{k}, \\ \boldsymbol{S}_{\boldsymbol{k},a} &\to \boldsymbol{S}_{-\boldsymbol{k},a} \equiv -\boldsymbol{S}_{\boldsymbol{k},a}. \end{aligned} \tag{7.13}$$

It is important to note that electron spin behaves in the same way as momentum under the time-reversal symmetry.

7.1.4 Special part in the Brillouin zone

In the Brillouin zone, specific crystal momenta are invariant under the space group operation $\{\alpha|\boldsymbol{b}\}$. Since the crystal momentum is defined modulo reciprocal vectors, the specific momentum $\boldsymbol{k}_s$ satisfies

$$\boldsymbol{k}_s \equiv \alpha\boldsymbol{k}_s \ (\text{mod } \boldsymbol{K}). \tag{7.14}$$

For the conventional definition of the Brillouin zone, $\boldsymbol{k}_s \neq \alpha\boldsymbol{k}_s$ lives on the boundary of the Brillouin zone. If a specific momentum is an isolated point, then it is called as a special point. For some space groups, there are points that are invariant under the common symmetries. A line (plane) that consists of such points is called as a special line (plane). Special parts of the Brillouin zone have conventional names such as Γ point. If a crystal momentum is only invariant under the primitive translation $\{\epsilon|\boldsymbol{t}_n\}$, it is called a general point.

For the crystal momentum $\boldsymbol{k}_s$ that is invariant under the operation $\{\alpha|\boldsymbol{b}\}$, $\{\alpha|\boldsymbol{b}\}\phi_{\boldsymbol{k}_s}$ is an irreducible representation of the translation group labeled by $\boldsymbol{k}_s$. By gathering all operations that do not change $\boldsymbol{k}_s$, we can construct a group. This is called the k-group $\mathcal{G}(\boldsymbol{k})$. In the case of symmorphic space groups, irreducible representations of the k-group can be written as [68]

$$D^{\boldsymbol{k}}(\{\alpha|\boldsymbol{b}\}) = \exp(i\boldsymbol{k}\cdot\boldsymbol{b})\Gamma(\alpha), \tag{7.15}$$

where Γ is an irreducible representation of the point group $\mathcal{G}_0(\boldsymbol{k})$ that consists of the rotation parts of $\mathcal{G}(\boldsymbol{k})$.

In addition to the special parts for space group symmetries, we can also consider the time-reversal symmetric points that satisfy

$$\boldsymbol{k}_s \equiv -\boldsymbol{k}_s \ (\text{mod } \boldsymbol{K}). \tag{7.16}$$

These points are equivalent to the inversion symmetric points. In a d-dimensional Brillouin zone, there are 2^d time-reversal points.

7.1.5 Irreducible part of the Brillouin zone

In the presence of the space group symmetry, important information is all included in a small part of the Brillouin zone. For each space group, we can define the point group that consists of rotation operations in the space group. The Brillouin zone divided by this point group is called the representation domain. If we

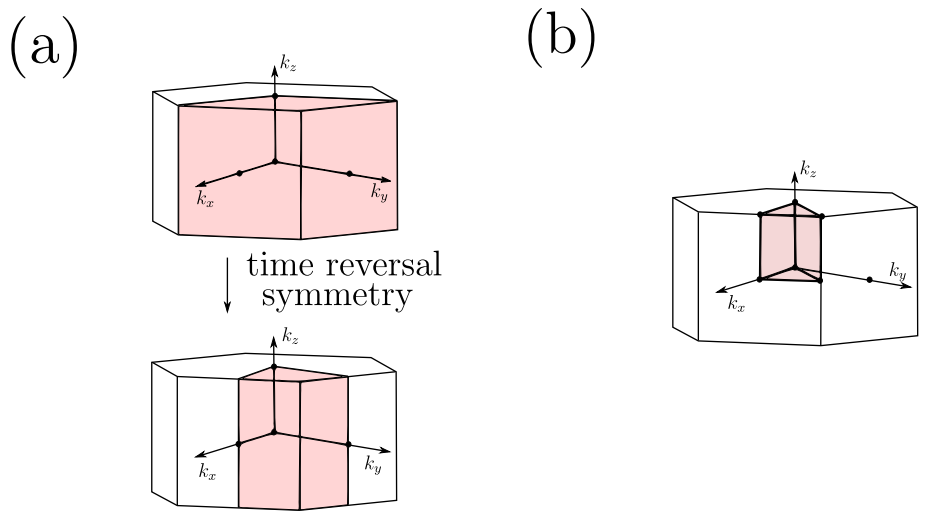

Figure 7.2: (a) Representation domain and irreducible part under the time-reversal symmetry for space group 143. (b) Basic domain for hexagonal lattice.

consider the time-reversal symmetry in addition to the space group symmetry, the irreducible part of the Brillouin zone is a half of the representation domain for inversion-broken systems. Since the crystal momentum behaves as $\boldsymbol{k} \to -\boldsymbol{k}$ under the inversion, the irreducible part of the Brillouin zone is the same as the representation domain for inversion-symmetric systems.

The basic domain is a similar notion. For each space group, there is one corresponding Brillouin zone. Each Brillouin zone corresponds to a Bravais lattice. The Brillouin zone divided by the point group of the Bravais lattice is called the basic domain. Since the symmetry of the Bravais lattice is higher than that of the space group, the basic domain is smaller than the representation domain. In Fig. 7.2, we draw the above three regions for space group No. 143 as an example.

7.2 Momentum space orbifold

Now we can cope with the problem of spin textures in momentum space under the space group symmetry in terms of the orbifold. As we discussed, momentum and electron spin are affected only by the point group part of the space group. Thus, all information of the spin texture in momentum space is included in the representation domain. If we assume the time-reversal symmetry, it is included in the irreducible part discussed above. Actually, these domains can be interpreted

as the orbifold[1] (hereafter, it is called as momentum space orbifold). In the following, we discuss the momentum space orbifold.

In the reciprocal space, there is the reciprocal lattice translation symmetry $\boldsymbol{k} \to \boldsymbol{k} + \boldsymbol{K}$. By combining this translation and the point group symmetry, we can construct a new group G_{rec}. Note that G_{rec} is not always equivalent to the original space group G. For nonsymmorphic space groups, G/T cannot be written as a point group. Also, the body-(face-)centered lattice corresponds to the face-(body-)centered reciprocal lattice. Thus, G_{rec} can be different from G even for symmorphic space groups. However, G_{rec} should have the same structure as some symmorphic space group with opposite centering type. Because this is a one-to-one correspondence, the number of types of G_{rec} is 73.

The reciprocal space $\mathbb{E}^3$ divided by G_{rec} is the orbifold $\mathbb{E}^3/G_{rec}$, which clearly describes the representation domain in the Brillouin zone. Since this orbifold is the same as some symmorphic space group orbifold, the following conditions should hold.

- $\mathbb{E}^3/G_{rec}$ is a compact orbifold.
- $\pi : BZ \to \mathbb{E}^3/G_{rec}$, where BZ is the Brillouin zone ($\mathbb{T}^3$), is a branched covering with degree $|P_{rec}|$, where P_{rec} is the point group part of G_{rec}.
- $\chi^{orb}(\mathbb{E}^3/G_{rec}) = 0$.

Since the specific momentum in the Brillouin zone is characterized by a point group, the following condition should also hold.

- The special points, lines, and planes in the Brillouin zone correspond to the singular points, lines, and planes of the orbifold, respectively.
- A neighborhood of such singular point $\boldsymbol{k}_s$ is isometric with a neighborhood of the origin of $\mathbb{E}^3/P(\boldsymbol{k}_s)$, where $P(\boldsymbol{k}_s)$ is the point group part of the k-group at $\boldsymbol{k}_s$.

Some readers might think that the only important information of an orbifold is included in the point group, and we just have to consider 32 orbifolds that correspond to 32 point groups. In general, however, this statement is incorrect. The symmorphic space groups are determined by the semidirect product (not direct product!) of the translation groups, whose number of types is 14 corresponding to the Bravais lattice, and point groups. This semidirect nature allows various

[1] In Ref. [93], the orbifold $\mathbb{T}^3/C_{nv}$ is discussed in the same context, though they do not use the properties related to the topology of orbifold itself.

types of orbifolds for the same point groups, and the number of $\mathbb{E}^3/G_{rec}$ (73) is larger than that of point groups (32).

In addition to the space group symmetry, we here consider the time-reversal symmetry. In the reciprocal space, it is convenient to define

$$\bar{G}_{rec} = G_{rec} + TG_{rec}, \tag{7.17}$$

where T is the time-reversal operation. In the presence of the inversion symmetry, the irreducible part of the Brillouin zone is the same as the representation domain. In the absence of it, on the other hand, the irreducible part is a half of the representation domain as mentioned above. In this case, we can construct a new orbifold $\mathbb{E}^3/\bar{G}_{rec}$ satisfying the following conditions.

- $\mathbb{E}^3/\bar{G}_{rec}$ is a compact orbifold.
- $\pi : BZ \to \mathbb{E}^3/\bar{G}_{rec}$, where BZ is the Brillouin zone ($\mathbb{T}^3$), is a branched covering with degree $|\bar{P}_{rec}|$, where $\bar{P}_{rec} = P_{rec} + TP_{rec}$.
- $\pi : \mathbb{E}^3/G_{rec} \to \mathbb{E}^3/\bar{G}_{rec}$ is a branched covering with degree 2.
- $\chi^{orb}(\mathbb{E}^3/\bar{G}_{rec}) = 0$.
- In addition to the special points, lines, and planes, the points, lines, and planes invariant under the time-reversal operation or the combination of the time-reversal and point group operations are also the singular points, lines, and planes of the orbifold, respectively.
- A neighborhood of such singular point $\boldsymbol{k}_s$ is isometric with a neighborhood of the origin of $\mathbb{E}^3/P'(\boldsymbol{k}_s)$, where $P'(\boldsymbol{k}_s)$ is a subgroup of $\bar{G}_{rec}$.

In the following, we consider behaviors of electron spin on the orbifold.

7.2.1 Spin texture for symmorphic space group: proper rotation

We first consider the symmorphic space groups whose elements are only proper rotations. Under proper rotations, spin behaves as a vector, and the pseudovector nature does not appear. In this case, point group operations act on momentum and electron spin in the same way. Thus, the classification of spin textures in momentum space is reduced to the classification of a vector field on the orbifold $\mathbb{E}^3/G_{rec}$.

Next, we consider the time-reversal symmetry. Under the time-reversal operation, momentum and electron spin behave in the same way [see Eq.(7.13)].

Since inversion, which is an improper rotation, is absent in this case, the classification of spin texture in momentum space is also reduced to the classification of a vector field on the orbifold $\mathbb{E}^3/\bar{G}_{rec}$.

Here we omit the discussion about behaviors of spin vector flow around the singular parts of the orbifold. In the next chapter, we will consider it.

7.2.2 Spin texture for symmorphic space group: improper rotation

In the case of symmorphic space groups that contain improper rotations, the situation is completely different. Since the sign of spin is flipped with respect to the sign of momentum under improper rotations, the identification is performed up to the sign of spin. In such cases, the classification of spin texture in momentum space cannot be reduced to the classification of a "single-valued" vector field on the $\mathbb{E}^3/G_{rec}$.

7.2.3 Spin texture for nonsymmorphic space group

The translation parts of the space group operations do not affect momentum and electron spin. If we ignore the non-primitive lattice translation, nonsymmorphic space groups are reduced to some symmorphic space groups. Thus, the classification of spin texture in momentum space of a nonsymmorphic space group is basically the same as that of corresponding symmorphic space group. However, the representation theory of a nonsymmorphic space group is not the same as that of the corresponding symmorphic space group. This difference sometimes affects the dimensionality of the representation. In such cases, there would be some difference that comes from band degeneracy due to the nonsymmorphic symmetries.

If we consider the Bloch wave functions, nonsymmorphic operations change the phase of them. This change is an important factor in the context of the topological crystalline insulators, topological Dirac (Weyl) semimetals, and so on.

7.2.4 Example: magnon spin texture in kagome lattice antiferromagnet

Although the main topic is about the three-dimensional electron systems, we here consider the magnon spin-momentum locking again. Let us consider the example in the kagome lattice antiferromagnet. Since the magnonic sysmtem

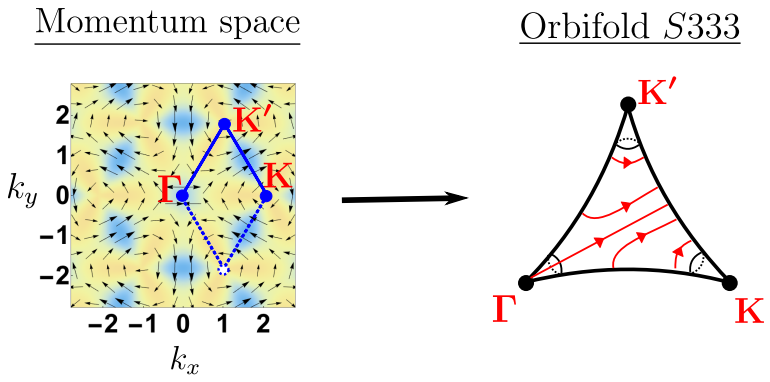

Figure 7.3: Magnon spin texture on orbfiold $S333$. The spin texture on momentum space is mapped onto a vector field (red lines) on the orbifold.

is not invariant under the time-reversal symmetry, $\boldsymbol{S}_{-\boldsymbol{k},a} \neq -\boldsymbol{S}_{\boldsymbol{k},a}$. The ground states have the three-fold rotational symmetry[2], and magnon dispersions reflect this symmetry. Magnon spin behaves as a vector under this proper rotation. In terms of the orbifold, the magnon spin texture in momentum space can be reduced to a vector field on the orbifold $S333$ (Fig. 7.3). As shown in Fig. 7.3, a magnon spin texture can be mapped to a well-defined vector field on the orbifold due to the properness of the symmetric operations. In such a case, all we have to do is classify vector fields on the orbifold that corresponds to the symmetric operations.

[2]We here ignore the reflection symmetry since it is absent if we choose another ground state. Also, there are other symmetric operations in the case of the magnets. If such symmetries are included, the number of space groups increases to 1651. We here ignore such symmetries for simplicity.

Chapter 8

Spin texture on momentum space orbifold

In this chapter, we consider spin textures on momentum space orbifolds for the specific 24 symmorphic space groups. In the cases of these space groups, a spin texture in momentum space can be mapped to a vector field on the momentum space orbifold. We first impose the conditions for electron systems. Then we discuss the behaviors of electron spin around and on the specific parts of momentum space. We also generalize the Poincaré-Hopf index theorem to spaces with singular points. Combining these topics, we present a theory of spin textures on orbifolds. By applying this theory to 24 space groups, we derive the constraints on orbifolds. These constraints would be useful to find the Weyl points and new spin monopoles with higher winding numbers.

8.1 Conditions for electron systems

In this thesis, we focus on three-dimensional electron systems under the specific symmetries. Since the magnetic materials have antiunitary symmetries other than the time-reversal symmetry, they are more complicated than non-magnetic materials. For simplicity, we consider only the non-magnetic materials and impose the time-reversal symmetry. In the presence of the time-reversal and inversion symmetries, there is always a spin degeneracy for each $\boldsymbol{k}$. Using

$$\begin{aligned} T^{-1}H_{-\boldsymbol{k}}T &= H_{\boldsymbol{k}}, \\ H_{\boldsymbol{k}} &= H_{-\boldsymbol{k}}, \end{aligned} \tag{8.1}$$

where $H_{\boldsymbol{k}}$ is the Bloch Hamiltonian, we can easily check it:

$$\begin{aligned} & T^{-1}H_{\boldsymbol{k}}[T|-\boldsymbol{k},a\rangle] = H_{-\boldsymbol{k}}|-\boldsymbol{k},a\rangle = E_{-\boldsymbol{k},a}|-\boldsymbol{k},a\rangle \\ \Leftrightarrow & H_{\boldsymbol{k}}[T|-\boldsymbol{k},a\rangle] = E_{-\boldsymbol{k},a}[T|-\boldsymbol{k},a\rangle], \qquad (8.2) \\ & H_{\boldsymbol{k}}|-\boldsymbol{k},a\rangle = H_{-\boldsymbol{k}}|-\boldsymbol{k},a\rangle = E_{-\boldsymbol{k},a}|-\boldsymbol{k},a\rangle. \qquad (8.3) \end{aligned}$$

Note that $|-\boldsymbol{k},a\rangle$ is orthogonal to $T|-\boldsymbol{k},a\rangle$ in the case of free fermion systems with spin-1/2 [68]. Thus, there should be a degeneracy at each momentum $\boldsymbol{k}$.

To define spin textures, there should not be the spin degeneracy for the whole region of the Brillouin zone. Thus, we consider the inversion-broken electron systems. Even when the systems break the inversion symmetry, there are spin degeneracies in the absence of the spin-orbit interaction, which are not protected by the symmetries. Thus, we assume the large spin-orbit interaction, which leads the experimentally observable spin splitting. Since the non-primitive lattice translation does not affect momentum and spin, we here consider the symmorphic space groups. In addition, we focus on the space groups whose elements are proper rotations for avoiding difficulty of sign flip under improper rotations discussed in Chap. 7.

In summary, we impose the following conditions.

- Three-dimensional non-magnetic (time-reversal symmetric) electron systems.
- Space groups are symmorphic.
- Elements of space groups are proper rotations.
- The inversion symmetry is broken. (This condition is included in the above condition.)
- The spin-orbit interaction is large.

The number of symmorphic space groups whose elements are proper rotations is 24. In the following sections, we investigate the topology of 24 momentum space orbifolds and classify spin textures on them.

Before ending this section, we discuss the types of symmorphic space groups. In terms of behaviors of electron spin, which is a pseudovector, the 73 symmorphic space groups are classified into three categories:

- Elements are proper rotations. (24 types)
  1, 3, 5, 16, 21, 22, 23, 75, 79, 89, 97,143,146, 149, 150, 155, 168, 177, 195, 196, 197, 207, 209, 211.

- At least one element is an improper rotation that is not the inversion. (25 types)
  6, 8, 25, 35, 38, 42, 44, 81, 82, 99, 107, 111, 115, 119, 121, 156, 157, 160, 174, 183, 187, 189, 215, 216, 217.

- One element is the inversion. (24 types)
  2, 10, 12, 47, 65, 69, 71, 83, 87, 123, 139, 147, 148, 162, 164, 166, 175, 191, 200, 202, 204, 221, 225, 229.

Here, each index, which is known as the international table number, represents one of the 230 space groups. Actually, 24 inversion-symmetric space groups can be constructed from 24 symmorphic space groups whose elements are proper rotations by adding the inversion operation. If we focus only on the momentum (not on spin), the inversion and time-reversal symmetries are equivalent each other. Thus, the topologies of 24 orbifolds for symmorphic space groups whose elements are proper rotations under the time-reversal symmetry are the same as those of corresponding symmorphic space groups with the inversion in the absence of the time-reversal symmetry.

8.2 Spin vector fields around singular parts

Since we now focus on the symmorphic space groups, singular parts in momentum space are invariant under the point group and time-reversal operations. Under the proper rotations and time-reversal operation, there are four types of singular parts in momentum space. We here discuss the behaviors of spin vector field around these singularities [Fig. 8.1].

Invariant line under point group C_n
A singular part under the n-fold rotation correspond to the n-fold rotation axis. On this axis, spin should also be invariant under the rotation. Thus, spin on the rotation axis should be parallel to the rotation axis.

Invariant point under point groups D_n, T, O
Singular parts under point group D_n, T, O are point-like. Under these symmetries, there are several rotation axes pointing different directions. On each axis, spin should be parallel to the rotation axis. However, it is impossible to satisfy such conditions for several axes simultaneously if there is no spin degeneracy. Thus, the singular point under point group D_n, T, O should be spin degenerated. Around this point, there is a monopole-like spin texture in momentum space.

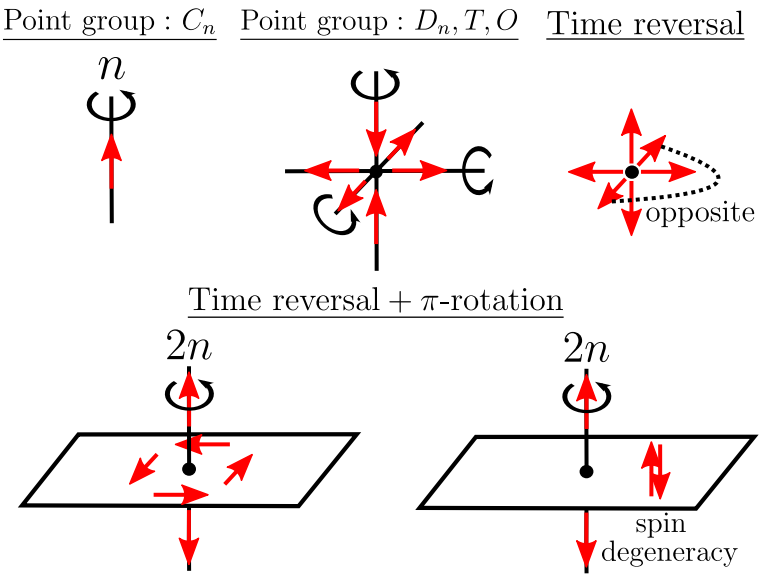

Figure 8.1: Spin vector field around singular parts of momentum space.

Time reversal invariant point

Singular parts under the time-reversal operation are called the time-reversal invariant points. Under the time-reversal operation, spin changes its sign on these points. However, positions of these points are invariant under the time-reversal operation by definition. Thus, there should be the spin degeneracy. Around the time-reversal invariant point, there is a monopole-like spin texture in momentum space. Spins on opposite sides should have opposite sign each other.

Invariant plane under time-reversal+π-rotation

By combining the time-reversal and π-rotation, we can construct a new operation. Let us consider the point group C_{2n}. This group contains the π-rotation. We can find the invariant plane under the combination of the π-rotation and time-reversal operation. This plane is connected to the rotation axis via the time-reversal point. On this plane, there are two possibilities of behaviors of spin textures. One possibility is that the spin texture is a tangent vector field on this plane. Another possibility is that spin is degenerated on whole region of this plane. However, such a spin degeneracy on planes makes the following argument more complicated. In the following, we only consider the first possibility.

8.3 Generalized Poincaré-Hopf index theorem

In Chap. 4, we described the Poincaré-Hopf index theorem, which relates the Euler characteristic and the sum of winding numbers. However, the original version of this theorem can only be applied to compact manifolds. To apply the theorem for singular spaces such as orbifolds, we should generalize this theorem. In our problem, the existence of isolated singular points means that spin is singular on these points. On the other hand, a spin vector field is nonsingular on the singular lines of orbifolds. Thus, we just generalize the Poincaré-Hopf index theorem for the space with isolated singular points. The following discussion is based on Ref. [94]

In terms of the Euler characteristic, an isolated singular point of the space corresponds to +1. This is because we always take singular points as 0-cells when we perform the cell decomposition. From this consideration, we can naturally generalize the Poincaré-Hopf index theorem. Let us focus on a vector field around a singular point of the space. We can consider singular vector fields with any winding number around the singular point of the space. To separate the singularity of the vector field and that of space itself, we introduce the radial vector field $\boldsymbol{v}_{rad}$ [Fig. 8.2].

Radial vector field

Let $\boldsymbol{v}$ be a vector field on a space with a singular point X and small spheres $S_\epsilon, S_{\epsilon'}, S_{\epsilon''}; \epsilon > \epsilon' \geq \epsilon'' > 0$ around the singular point. A radial vector field $\boldsymbol{v}_{rad}$ for $\boldsymbol{v}$ is defined by replacing the vector field around the singular points with a vector field that obeys the following conditions:

- $\boldsymbol{v}_{rad}$ on $X \backslash S_\epsilon$ is the same as $\boldsymbol{v}$.
- For any ϵ'', $\boldsymbol{v}_{rad}$ is transverse (outwards-pointing) to $S_{\epsilon''}$.
- $\boldsymbol{v}_{rad}$ between S_ϵ and $S_{\epsilon'}$ should be taken to connected both to the above regions.

Since any change of the vector field inside the small sphere S_ϵ around the singular point does not affect the vector field on $\mathrm{X} \backslash S_\epsilon$, we can consider the radial vector field instead of the original vector field. In the following, we generalize the Poincaré-Hopf index theorem for radial vector field.

We here define the Schwarz index around the singular point i of the space:

$$\mathrm{Ind}_{\mathrm{Sch}}(i) = 1 + \sum_j Q^i_j, \tag{8.4}$$

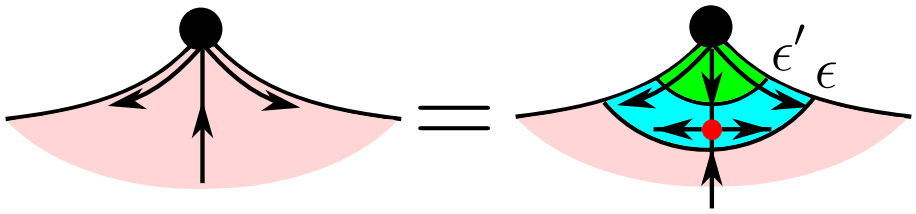

Figure 8.2: Schematic picture of a radial vector field on space with singular points.

where Q^i_j are the winding numbers of singular structures of vector field between S_ϵ and $S_{\epsilon'}$, and 1 denotes the winding number comes from the singular point of space. Using this index, we obtain the generalized Poincaré-Hopf index theorem.

Poincaré-Hopf index theorem for space with singular points

Let X be a space with singular points $\{p_i\}$ and $\boldsymbol{v}$ be a vector field with singular points $\{q_k\}$ with winding number Q_{q_k}. Then the Poincaré-Hopf index theorem is generalized as

$$\begin{aligned}\chi(X) &= \sum_{p_i} \mathrm{Ind}_{\mathrm{Sch}}(p_i) + \sum_{q_k} Q_{q_k} \\ &= \sum_{p_i}(1 + \sum_j Q^{p_i}_j) + \sum_{q_k} Q_{q_k}. \end{aligned} \tag{8.5}$$

8.4 Method

Now we can classify the spin texture in momentum space. In this section, we focus on the space group No. 168 (Schoenflies notation[1]: C^1_6) as one of the simplest examples. We give the procedure to investigate the singular structures in the spin texture on the momentum space orbifold. We also explain how we can interpret spin textures on the orbifold in terms of the Brillouin zone.

[1]In this notation, we can identify the point group of the space group. The upper subscript distinguishes different space groups with the same point group.

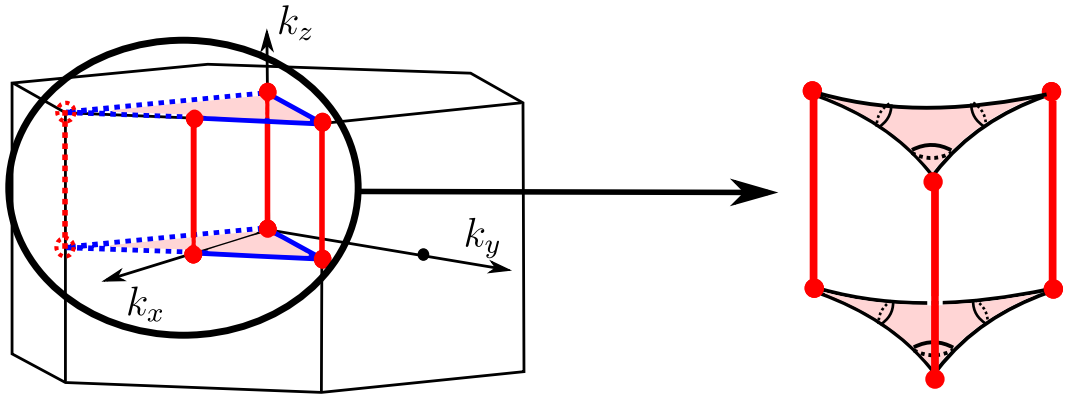

Figure 8.3: Irreducible Brillouin zone and singular parts of momentum space orbifold of space group No. 168. Red points denote the singular points with monopole spin structure. Red and blue solid lines denote the rotational axis and lines with the same symmetry as the plane, respectively. Red planes are invariant planes under the combination of the time-reversal operation and π-rotation. Dotted objects are identified with other part of the irreducible Brillouin zone.

8.4.1 Irreducible Brillouin zone and momentum space orbifold

In general, three-dimensional spaces cannot be drawn in two-dimensional objects such as this thesis. Instead, we can get the insight into the shape of an orbifold by drawing the singular parts of the orbifold, whose dimensions are lower than that of the orbifold itself. In the following, we draw the singular parts of the momentum space orbifold. Note that even the singular parts for some space groups cannot be drawn on the paper because of their unorientability.

Let us consider the Brillouin zone of the space group No. 168. The point group is C_6, and the representation domain (see the definition in Chap. 5) is 1/6 of the Brillouin zone. We also consider the time-reversal symmetry in addition to the point group, and the irreducible Brillouin zone is 1/12 of the Brillouin zone [Fig. 8.3]. There are 6 singular points, 3 singular lines, and 2 singular planes. In this case, all singular points are connected to other singularities. The symmetry of d-dimensional singular parts are lower than that of the connected $(d-1)$-dimensional singular parts.

The boundary region of the irreducible Brillouin zone is identified with other region of the Brillouin zone, which is related with the symmetry operations. Consider the identification of the blue dotted and solid lines in Fig. 8.3. Under

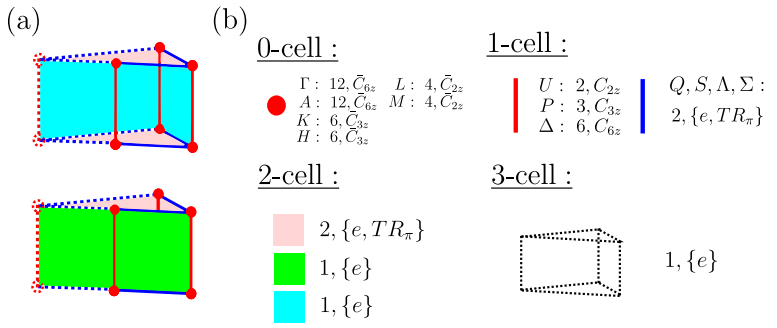

Figure 8.4: (a) Schematic pictures of identification of planes. Blue planes and green planes are related via 6-fold and 2-fold rotations, respectively. (b) List of d-cells. The name and order of each group is shown.

this identification, the invariant plane becomes a closed object (the right panel of Fig. 8.3). This is homeomorphic with the two-sphere S^2. (Imagine the surface shape of a triangle pie). There are three singular points on this plane, and they are connected to the singular lines.

8.4.2 Euler and orbifold Euler characteristics

As we explained in Chap. 6, there are two types of numbers that characterize orbifolds. One is the Euler characteristic, which is a topological invariant of the orbifold. This index appears in generalized Poincaré-Hopf index theorem for the singular space. The other one is the orbifold Euler characteristic. As we saw in Chap. 7, this index is always zero for the momentum space orbifolds defined for any space groups. Both indices can be calculated by using the cell decomposition of the orbifold.

Actually, the cell decomposition is given by the picture of the irreducible Brillouin zone shown in the left panel of Fig. 8.3. It is important to note that identifications of planes should be also considered, as shown in Fig. 8.4 (a). The blue planes are identified by the 6-fold rotation, while the green planes by the 2-fold rotation.

In general, it is not easy to obtain the correct cell decomposition, especially for more complicated Brillouin zone. In such complicated cases, the calculation of the orbifold Euler characteristic, which should be zero for the momentum space orbifold, is one of the best ways to check the validity of the cell decomposition. Let us calculate the orbifold Euler characteristic for momentum space orbifold of No. 168. The list of d-cells is shown in Fig. 8.4(b). In this case, six 0-cells

are time-reversal points. On such a point, the symmetry group is given by

$$\bar{A} = A + TA, \tag{8.6}$$

where A is the point group, and T is the time-reversal operation. Hereinafter, we use red points for describing the singular points of orbifold. There are seven 1-cells. Three of them are the singular lines of the orbifold, which are characterized by rotational groups. Hereinafter, we use red lines for describing the singular lines of orbifolds. Rest of them are parts of the singular planes as explained later. We here use blue lines for describing the lines that belong to the singular planes. There are four 2-cells. Two of them are invariant under the group

$$\{e, TR_\pi\}, \tag{8.7}$$

where R_π denotes π-rotation. Hereinafter, we use red planes for describing the singular planes of orbifold. Rest of them are planes that consist of general points. There is one 3-cell that consists of general points. By using the definition of the orbifold Euler characteristic, we obtain

$$\begin{aligned}\chi^{orb}(\mathcal{O}) =& \left(\frac{1}{12}+\frac{1}{12}+\frac{1}{6}+\frac{1}{6}+\frac{1}{4}+\frac{1}{4}\right)\\ &-\left(\frac{1}{2}+\frac{1}{3}+\frac{1}{6}+\frac{1}{2}\times 4\right)\\ &+\left(\frac{1}{2}+\frac{1}{2}+1+1\right)\\ &-1\\ =&0.\end{aligned} \tag{8.8}$$

This result implies that the cell decomposition of the momentum space orbifold shown in Fig. 8.4 is correct.

Once we get the cell decomposition of the orbifold, we can easily compute the Euler characteristic of the momentum space orbifold. By replacing the fractions in Eq. (8.8) with 1, we obtain

$$\chi(\mathcal{O}) = 6 - 7 + 4 - 1 = 2. \tag{8.9}$$

Interestingly, the Euler characteristic is finite. This means that the vector field cannot be *boring* in the context of the Poincaré-Hopf index theorem.

8.4.3 Poincaré-Hopf index theorem for parts

We now obtain the Euler characteristic of the momentum space orbifold. Naively speaking, we might be able to investigate spin textures by using the generalized

Poincaré-Hopf index theorem for the orbifold itself. However, this observation ignores the constraints for spin textures on the singular parts of the orbifold. On the singular line, electron spin should be parallel to the singular line. Also, electron spin should lie on the singular plane. Thus, the spin texture is the tangent vector field on the orbifold. In addition, the singular lines and planes are compact. Thanks to these properties, we can apply the Poincaré-Hopf index theorem for each singular line of plane.

Let us consider a part that consists of one singular line and two singular points connected to the line. The Euler characteristic of this part is

$$\chi^{1D} = 2 - 1 = 1, \tag{8.10}$$

which has already been investigated in Eq. (6.2). This part can be interpreted as the singular space with two singular points. We here assign the winding number $+1$ for these two points as we did in the explanation of the generalized Poincaré-Hopf index theorem. By applying the generalized Poincaré-Hopf index theorem for this part, we obtain

$$\begin{aligned} \chi^{1D} &= (+1) \times 2 + \sum_i Q_i \\ \Leftrightarrow \sum_i Q_i &= -1, \end{aligned} \tag{8.11}$$

where Q_i is the winding number for a spin monopole i on the line. Thus, there should be at least one spin monopole with the total winding number -1 on the line. There are three such 1-dimensional lines.

Next, we consider a part that consists of a singular plane and three singular points. The Euler characteristic of this part is

$$\chi^{2D} = 2. \tag{8.12}$$

This can be easily checked by the cell decomposition or using the fact that this part is homeomorphic with the two-sphere. By performing the similar procedure, we obtain

$$\begin{aligned} \chi^{2D} &= (+1) \times 3 + \sum_i Q_i \\ \Leftrightarrow \sum_i Q_i &= -1, \end{aligned} \tag{8.13}$$

where Q_i is the winding number for a spin monopole i on the plane. Thus, there should be at least one with total winding number -1 on anywhere of this plane. There are two such planes.

In summary, we find at least 5 spin monopoles with winding number -1 on the singular parts of the orbifold [Fig. 8.5 (a)].

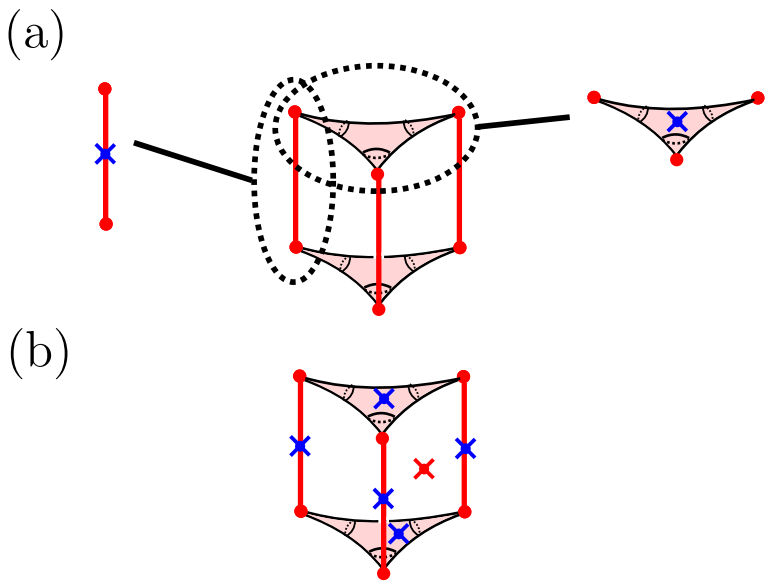

Figure 8.5: Schematic picture of the Poincaré-Hopf index theorem for (a) singular parts and (b) orbifold itself. Red and blue cross marks represent spin monopoles with winding number $+1$ and -1, respectively.

8.4.4 Poincaré-Hopf index theorem for whole region

Now we discuss the Poincaré-Hopf index theorem for the orbifold itself. We have obtained the Euler characteristic of the momentum space orbifold by using the cell decomposition [Eq. (8.9)]. We have also found that there are six singular points of orbifolds, which have spin monopoles with winding number $+1$, and five spin monopoles with winding number -1 on singular lines and planes. By using these facts and applying the Poincaré-Hopf index theorem for the orbifold itself, we find

$$\begin{aligned} \chi(\mathcal{O}) &= (+1) \times 6 + (-1) \times 5 + \sum_i Q_i \\ \Leftrightarrow \sum_i Q_i &= +1, \end{aligned} \tag{8.14}$$

where Q_i is the winding number for a spin monopole i on a general point of the orbifold. Thus, there should be at least one spin monopole with winding number $+1$ in the general region[2].

[2]In the band theory, the general region is defined as the region without any symmetry.

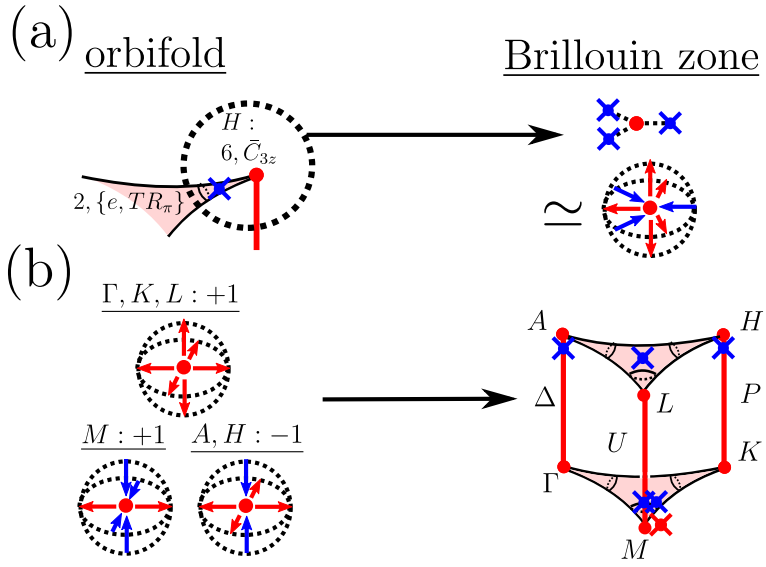

Figure 8.6: (a) Example of spin monopole with a negative high winding number. (b) Example of spin texture around the special points and the corresponding orbifold picture.

The schematic picture of the spin vector fields on the orbifold is shown in Fig. 8.5(b). Once a space group is given, we can characterize the spin texture in momentum space by drawing the picture such as Fig. 8.5(b).

Although the generalized Poincaré-Hopf index theorem can determine the total winding number, it cannot determine the position of spin monopoles. As we saw, the spin monopoles that are close to the singular point of the space (orbifold in this case) can be regarded as one spin monopole around the singular point of the space. If they are not close to it, they are distinguished from the spin monopole around the singular point. This argument means that physical interpretations of the picture [Fig. 8.5(b)] are not unique.

8.4.5 Interpretation in Brillouin zone

So far, we have classified spin textures on the momentum space orbifold for the given space group. However, what we really want to know is the spin texture in the Brillouin zone. In the following, we discuss how the picture [Fig. 8.5(b)] is interpreted in this context.

The continuous map $\pi : BZ \to \mathbb{E}^3/\bar{C}_6^1$ is a branched covering with degree 12. This means that a general point in the orbifold, whose neighborhood is isometric

with a neighborhood of $\mathbb{E}^3$, corresponds to 12 points in the Brillouin zone. On the other hand, a singular part with order n, which is a divisor of 12, correspond to $12/n$ parts[3] in the Brillouin zone. The number of spin monopoles obeys the same rule. This means that the order of the place in which spin monopoles live is an important factor to understand the spin texture in the Brillouin zone. Note that the winding number of a spin vortex is not changed under proper rotations and time-reversal operations, while it is changed under improper rotations. If the spin monopole is far from singular points of the orbifold, there are $12/n$ spin monopoles with the same winding number in the Brillouin zone. In the case of [Fig. 8.5(b)], we can predict the existence of the Weyl dispersions because spin monopoles with winding numbers ± 1 are known to correspond to the Weyl points[4].

If the spin monopole is close to a singular point and absorbed into it, the story should be changed since the order of the singular point is different from that of the spin monopole.

Let us consider the situation in Fig. 8.6 (a). A spin monopole with winding number -1 on a singular plane is absorbed into the spin monopole around a singular point H. The total winding number around H point on the orbifold is

$$Q'_H = +1 + (-1) = 0, \tag{8.15}$$

where Q' denotes the winding number defined on the orbifold. However, the winding number in the momentum space is different from Eq. (8.15). Let us move on to the momentum space description. The orders of the singular plane and point are 2 and 6, respectively. Thus, there are $12/6 = 2$ points that correspond to H point and $12/2 = 6$ points that correspond to the spin monopole. $6/2 = 3$ spin monopoles with winding number -1 are absorbed into each H point. The total winding number of the spin monopoles around the H point is given by

$$Q_H = +1 + (-1) \times \frac{6}{2} = -2. \tag{8.16}$$

In this situation, a spin monopole with a negative high winding number appears around H point. In general, we should be careful if we add spin monopoles to a spin monopole with different order of singularity in the orbifold.

[3] In band theory, this number corresponds to the number of stars of a k-vector.

[4] Strictly speaking, the existence of spin monopoles just **indicates** the existence of Weyl points. In the case of the simple Weyl semimetals that are well described by a two-band model (see Chap. 1) with the Pauli matrices in spin space, spin monopoles with winding numbers ± 1 corresponds to the Weyl points [66]. However, the sublattice and orbital degrees of freedom would be able to cause singular spin textures without band touching points. In general, whether the correspondence holds or not depends on the details of the band structure.

Although the picture [Fig. 8.5(b)] cannot distinguish whether spin monopoles are absorbed into the singular point of the orbifold, we believe that this picture is useful for topological material science. For example, it is expected to derive constraints such as the following statement: "In this space group, there should be the higher winding number spin monopole around a special point or a Weyl point at a general point." Actually, this situation is realized in some space groups, as shown later. Even though this situation is not realized, the spin texture classification on orbifolds is still useful. Suppose that we want to find a candidate of the Weyl semimetal, and there is a result about the first principles band calculation. In general, it is difficult to find spin monopoles in the whole Brillouin zone. However, we can determine the place of Weyl points by using the orbifold picture. If we want to know whether the spin monopoles exist in the region apart from the singular points, all we have to do is investigate the spin textures around the singular points. Let us consider the situation in Fig. 8.6 (b). If the spin textures around special points are given by the left panel, the corresponding orbifold picture is given by the right panel. This picture means that there is one spin vortex with the winding number -1 on the special plane.

8.4.6 Summary of the method

For a given space group, we first draw the picture of the singular parts of the orbifold by identifying the parts of irreducible Brillouin zone related via the symmetry operation. Since the picture of the irreducible Brillouin zone corresponds to a cell decomposition of the momentum space orbifold, we derive the Euler characteristic of the orbifold. In this procedure, we can check the validity of the cell decomposition by checking the orbifold Euler characteristic being zero for that cell decomposition.

Next, we assign the winding number $+1$ for each singular points of the orbifold, and apply the generalized Poincaré-Hopf index theorem for singular lines and planes. Through this procedure, we obtain the information about the spin monopoles on the singular lines and planes. After determining spin monopoles on such singular parts, we apply the generalized Poincaré-Hopf index theorem for the momentum space orbifold itself.

Once we obtain the picture such as Fig. 8.5(b), we can interpret the picture in the context of the Brillouin zone. By considering the order of singular parts carefully, we can reproduce the spin texture in the Brillouin zone. Although there are still a lot of possibilities for spin texture, it might be useful to find interesting spin texture in momentum space.

8.5 Spin texture on 24 momentum space orbifolds

In this section, we draw the singular parts of the momentum space orbifolds for the 24 space groups [Fig. 8.7-8.30]. As we discussed, the singular parts correspond to the specific parts in the Brillouin zone. In the band theory, such parts have conventional names such as Γ point[5]. We here use the notations in Refs. [95, 96, 97]. We list the order of singularity for each singular part. The numbers on right- and left-hand sides denote the order of singularity with and without the time-reversal symmetry, respectively. We also write down the Poincarè-Hopf index theorem with information of the places of spin monopoles. This information is also drawn in the orbifold picture on the right panel. The red and blue cross marks denote the $+1$ and -1 spin monopoles, respectively.

[5]Sometimes parts without any symmetries have also names.

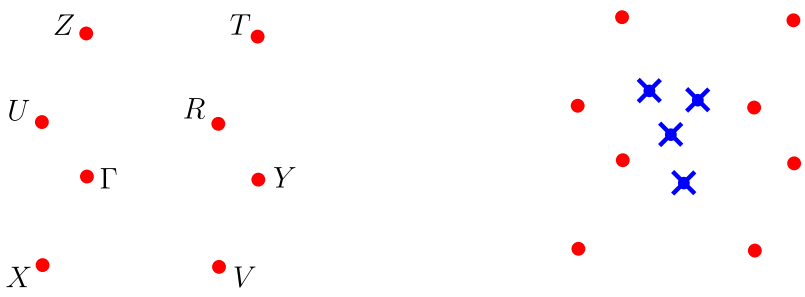

singularity			
$\Gamma:\ 1\to 2$	$T:\ 1\to 2$		
$X:\ 1\to 2$	$U:\ 1\to 2$		
$Y:\ 1\to 2$	$V:\ 1\to 2$		
$Z:\ 1\to 2$	$R:\ 1\to 2$		

index theorem	
$\chi(\mathcal{O})=4$	
$=(+1)\times 8$	$\cdots$at point
$+0$	$\cdots$on line
$+0$	$\cdots$on plane
$+(-1)\times 4$	$\cdots$general point

Figure 8.7: Space group no. 1 (C_1^1).

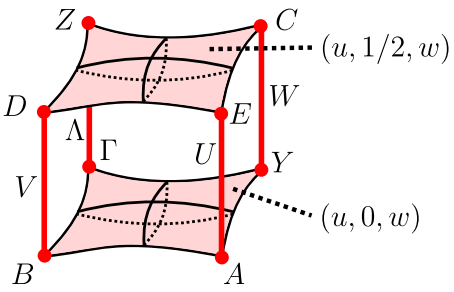

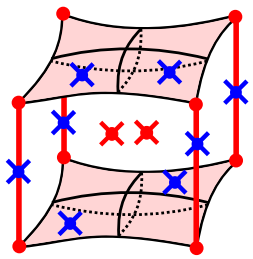

singularity		
$\Gamma:\ 2\to 4$	$D:\ 2\to 4$	$U:\ 2\to 2$
$A:\ 2\to 4$	$E:\ 2\to 4$	$V:\ 2\to 2$
$B:\ 2\to 4$	$Y:\ 2\to 4$	$\Lambda:\ 2\to 2$
$C:\ 2\to 4$	$Z:\ 2\to 4$	$W:\ 2\to 2$
$(u,1/2,w):\ 1\to 2$		
$(u,0,w):\ 1\to 2$		

index theorem	
$\chi(\mathcal{O})=2$	
$=(+1)\times 8$	$\cdots$at point
$+(-1)\times 4$	$\cdots$on line
$+(-1)\times 4$	$\cdots$on plane
$+(+1)\times 2$	$\cdots$general point

Figure 8.8: Space group no. 3 (C_2^1).

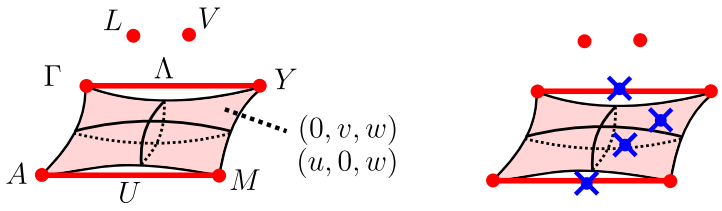

singularity					
$\Gamma:\ 2\to 4$	$L:\ 1\to 2$	$\Lambda:\ 2\to 2$			
$Y:\ 2\to 4$	$V:\ 1\to 2$	$U:\ 2\to 2$			
$M:\ 2\to 4$	$(0,v,w):\ 1\to 2$				
$A:\ 2\to 4$	$(u,0,w):\ 1\to 2$				

index theorem	
$\chi(\mathcal{O})=2$	
$=(+1)\times 6$	$\cdots$at point
$+(-1)\times 2$	$\cdots$on line
$+(-1)\times 2$	$\cdots$on plane
$+(+1)\times 0$	$\cdots$general point

Figure 8.9: Space group no. 5 (C_2^3).

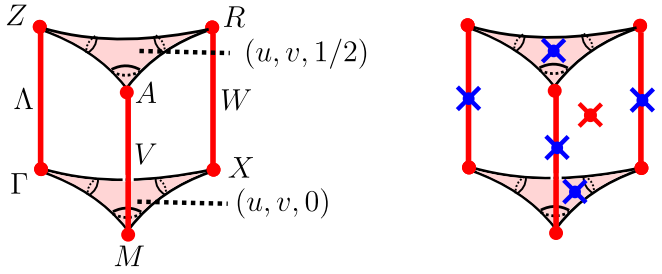

singularity					
$\Gamma:\ 4\to 8$	$A:\ 4\to 8$	$\Lambda:\ 4\to 4$			
$Z:\ 4\to 8$	$X:\ 2\to 4$	$V:\ 4\to 4$			
$M:\ 4\to 8$	$R:\ 2\to 4$	$W:\ 2\to 2$			
$(u,v,0):\ 1\to 2$	$(u,v,1/2):\ 1\to 2$				

index theorem	
$\chi(\mathcal{O})=2$	
$=(+1)\times 6$	$\cdots$at point
$+(-1)\times 3$	$\cdots$on line
$+(-1)\times 2$	$\cdots$on plane
$+(+1)$	$\cdots$general point

Figure 8.10: Space group no. 75 (C_4^1).

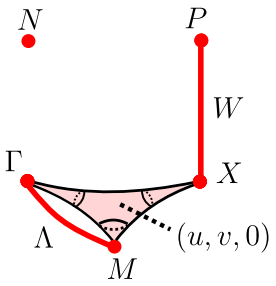

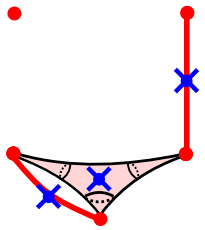

singularity

$\Gamma:$	$4 \to 8$	$P:$	$2 \to 4$
$\Lambda:$	$4 \to 4$	$M:$	$4 \to 8$
$N:$	$1 \to 2$	$W:$	$2 \to 2$
$X:$	$2 \to 4$	$(u, v, 0):$	$1 \to 2$

index theorem

$\chi(\mathcal{O}) = 2$

$= (+1) \times 5$ ⋯ at point

$+ (-1) \times 2$ ⋯ on line

$+ (-1)$ ⋯ on plane

$+ 0$ ⋯ general point

Figure 8.11: Space group no. 79 (C_4^5).

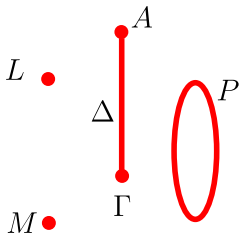

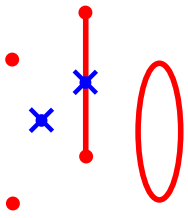

singularity

$\Gamma:$	$3 \to 6$	$\Delta:$	$3 \to 3$
$A:$	$3 \to 6$	$P:$	$3 \to 3$
$L:$	$1 \to 2$		
$M:$	$1 \to 2$		

index theorem

$\chi(\mathcal{O}) = 2$

$= (+1) \times 4$ ⋯ at point

$+ (-1)$ ⋯ on line

$+ 0$ ⋯ on plane

$+ (-1)$ ⋯ general point

Figure 8.12: Space group no. 143 (C_3^1).

singularity			
$\Gamma: 3 \to 6$	$\Lambda: 3 \to 3$		
$T: 3 \to 6$			
$L: 1 \to 2$			
$F: 1 \to 2$			

index theorem	
$\chi(\mathcal{O}) = 2$	
$= (+1) \times 4$	$\cdots$ at point
$+ (-1)$	$\cdots$ on line
$+ 0$	$\cdots$ on plane
$+ (-1)$	$\cdots$ general point

Figure 8.13: Space group no. 146 (C_3^4).

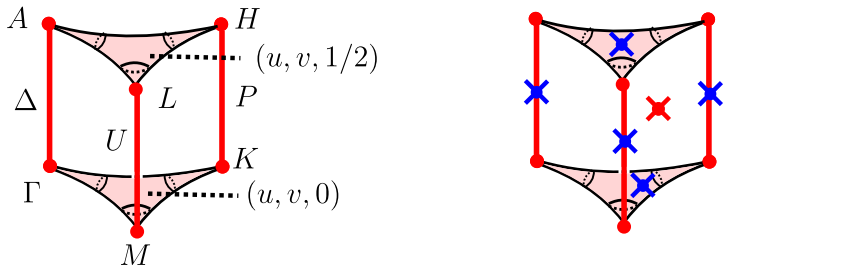

singularity			
$\Gamma: 6 \to 12$	$K: 3 \to 6$	$\Delta: 6 \to 6$	
$A: 6 \to 12$	$H: 3 \to 6$	$P: 3 \to 3$	
$L: 2 \to 4$		$U: 2 \to 2$	
$M: 2 \to 4$			
$(u, v, 0): 1 \to 2$	$(u, v, 1/2): 1 \to 2$		

index theorem	
$\chi(\mathcal{O}) = 2$	
$= (+1) \times 6$	$\cdots$ at point
$+ (-1) \times 3$	$\cdots$ on line
$+ (-1) \times 2$	$\cdots$ on plane
$+ (+1)$	$\cdots$ general point

Figure 8.14: Space group no. 168 (C_6^1).

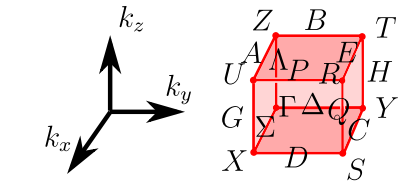

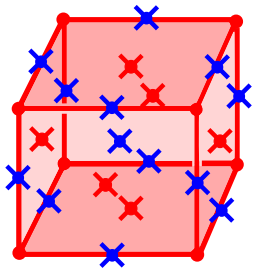

singularity

$\Gamma:$	$4 \to 8$	$A:$	$2 \to 4$	$Q:$	$2 \to 4$
$R:$	$4 \to 8$	$B:$	$2 \to 4$	$\Lambda:$	$2 \to 4$
$S:$	$4 \to 8$	$E:$	$2 \to 4$	$\Sigma:$	$2 \to 4$
$T:$	$4 \to 8$	$P:$	$2 \to 4$	$D:$	$2 \to 4$
$U:$	$4 \to 8$	$G:$	$2 \to 4$	$C:$	$2 \to 4$
$X:$	$4 \to 8$	$H:$	$2 \to 4$	$\Delta:$	$2 \to 4$
$Y:$	$4 \to 8$	$(0\&1/2, v, w):$		$1 \to 2$	
$Z:$	$4 \to 8$	$(u, 0\&1/2, w):$		$1 \to 2$	
		$(u, v, 0\&1/2):$		$1 \to 2$	

index theorem

$\chi(\mathcal{O}) = 1$
$= (+1) \times 8$ ⋯ at point
$+ (-1) \times 12$ ⋯ on line
$+ (+1) \times 6$ ⋯ on plane
$+ (-1)$ ⋯ general point

Figure 8.15: Space group no. 16 (D_2^1).

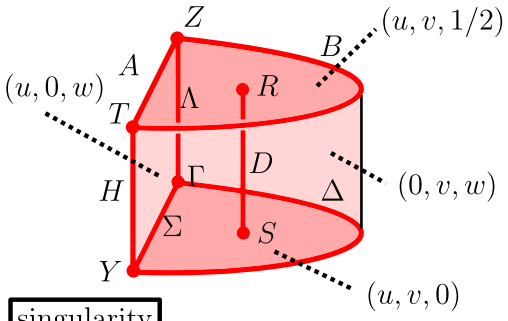

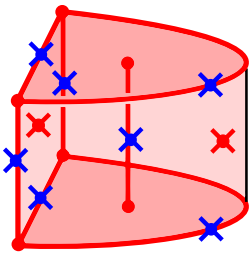

singularity

$\Gamma:$	$4 \to 8$	$A:$	$2 \to 2$	$D:$	$2 \to 2$
$T:$	$4 \to 8$	$B:$	$2 \to 4$	$H:$	$2 \to 4$
$Y:$	$4 \to 8$	$\Delta:$	$2 \to 4$	$\Lambda:$	$2 \to 4$
$Z:$	$4 \to 8$	$\Sigma:$	$2 \to 4$		
$S:$	$2 \to 4$	$(u, v, 0\&1/2):$		$1 \to 2$	
$R:$	$2 \to 4$	$(u, 0, w):$		$1 \to 2$	
		$(0, v, w):$		$1 \to 2$	

index theorem

$\chi(\mathcal{O}) = 1$
$= (+1) \times 6$ ⋯ at point
$+ (-1) \times 7$ ⋯ on line
$+ (+1) \times 2$ ⋯ on plane
$+ 0$ ⋯ general point

Figure 8.16: Space group no. 21 (D_2^6).

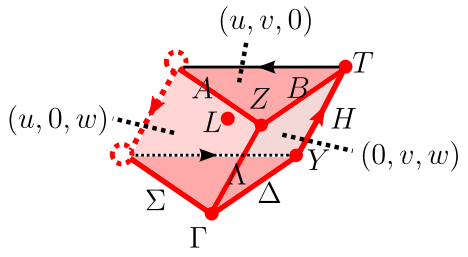

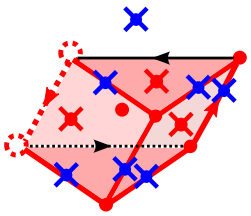

Note : unoriented

singularity					
Γ :	$4 \to 8$	H :	$2 \to 4$	Δ :	$2 \to 4$
T :	$4 \to 8$	Λ :	$2 \to 4$	A :	$2 \to 4$
Y :	$4 \to 8$	B :	$2 \to 4$	Σ :	$2 \to 4$
Z :	$4 \to 8$	$(0, v, w)$:	$1 \to 2$		
L :	$1 \to 2$	$(u, 0, w)$:	$1 \to 2$		
		$(u, v, 0)$:	$1 \to 2$		

index theorem		
$\chi(\mathcal{O})$	$=1$	
	$=(+1) \times 5$	$\cdots$at point
	$+(-1) \times 6$	$\cdots$on line
	$+(+1) \times 3$	$\cdots$on plane
	$+(-1)$	$\cdots$general point

Figure 8.17: Space group no. 22 (D_2^7).

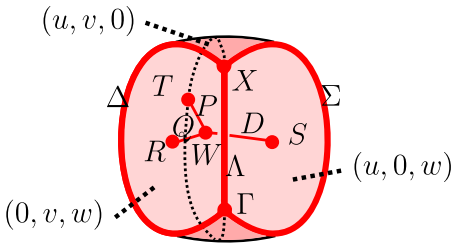

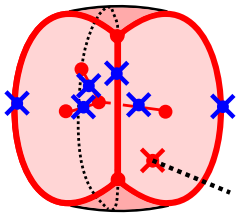

inside

singularity					
Γ :	$4 \to 8$	Λ :	$2 \to 4$	D :	$2 \to 2$
X :	$4 \to 8$	Δ :	$2 \to 4$	P :	$2 \to 2$
T :	$2 \to 4$	Σ :	$2 \to 4$	Q :	$2 \to 2$
R :	$2 \to 4$	$(0, v, w)$:	$1 \to 2$		
S :	$2 \to 4$	$(u, 0, w)$:	$1 \to 2$		
W :	$4 \to 4$	$(u, v, 0)$:	$1 \to 2$		

index theorem		
$\chi(\mathcal{O})$	$=1$	
	$=(+1) \times 6$	$\cdots$at point
	$+(-1) \times 6$	$\cdots$on line
	$+0$	$\cdots$on plane
	$+(+1)$	$\cdots$general point

Figure 8.18: Space group no. 23 (D_2^8).

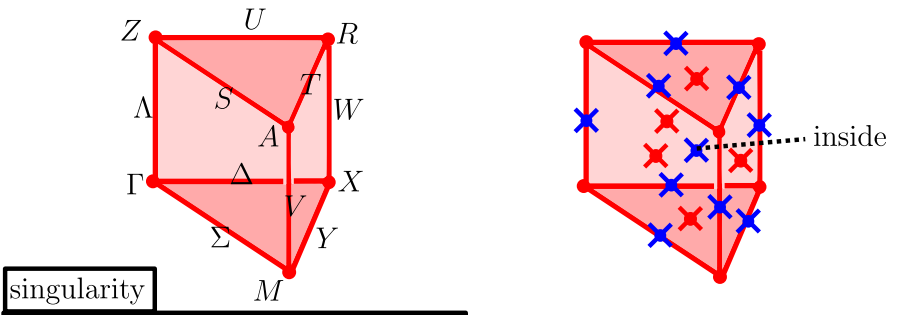

singularity					
$\Gamma:\ 8\to16$	$W:\ 2\to4$	$U:\ 2\to4$			
$A:\ 8\to16$	$S:\ 2\to4$	$Y:\ 2\to4$			
$M:\ 8\to16$	$\Sigma:\ 2\to4$	$\Lambda:\ 4\to8$			
$Z:\ 8\to16$	$\Delta:\ 2\to4$	$V:\ 4\to8$			
$R:\ 4\to8$	$T:\ 2\to4$				
$X:\ 4\to8$	$(0,v,w):\ 1\to2$	$(u,1/2,w):\ 1\to2$	$(u,u,w):\ 1\to2$	$(u,v,0\&1/2):\ 1\to2$	

index theorem	
$\chi(\mathcal{O})=1$	
$=(+1)\times6$	$\cdots$at point
$+(-1)\times9$	$\cdots$on line
$+(+1)\times5$	$\cdots$on plane
$+(-1)$	$\cdots$general point

Figure 8.19: Space group no. 89 (D_4^1).

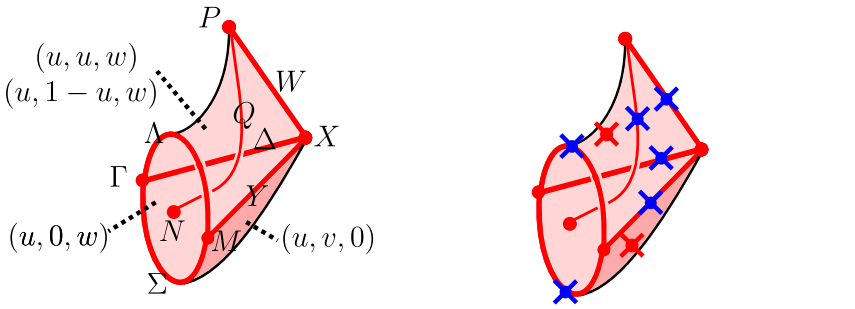

singularity					
$\Gamma:\ 8\to16$	$W:\ 2\to4$	$\Delta:\ 2\to4$			
$M:\ 8\to16$	$Q:\ 2\to2$	$Y:\ 2\to4$			
$X:\ 4\to8$	$\Sigma:\ 2\to4$	$\Lambda:\ 4\to8$			
$N:\ 2\to4$	$(u,0,w):\ 1\to2$	$(u,u,w):\ 1\to2$	$(u,v,0):\ 1\to2$	$(u,1-u,w):\ 1\to2$	
$P:\ 4\to8$					

index theorem	
$\chi(\mathcal{O})=1$	
$=(+1)\times5$	$\cdots$at point
$+(-1)\times6$	$\cdots$on line
$+(+1)\times2$	$\cdots$on plane
$+0$	$\cdots$general point

Figure 8.20: Space group no. 97 (D_4^9).

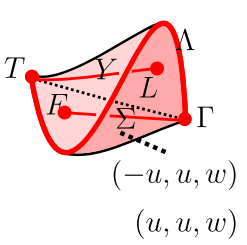

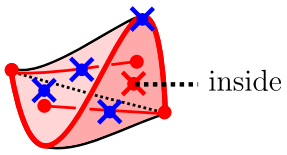

singularity			
$\Gamma:\ 6\to 12$	$\Sigma:\ 2\to 2$		
$T:\ 6\to 12$	$Y:\ 2\to 2$		
$F:\ 2\to 4$	$\Lambda:\ 3\to 6$		
$L:\ 2\to 4$	$(-u,u,w):\ 1\to 2$		
	$(u,u,w):\ 1\to 2$		

index theorem	
$\chi(\mathcal{O})=1$	
$=(+1)\times 4$	$\cdots$at point
$+(-1)\times 3$	$\cdots$on line
$+(-1)$	$\cdots$on plane
$+(+1)$	$\cdots$general point

Figure 8.21: Space group no. 155 (D_3^7).

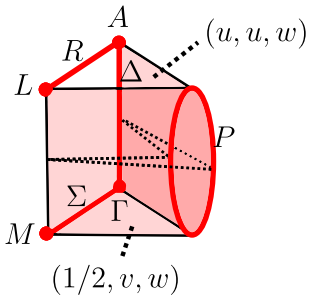

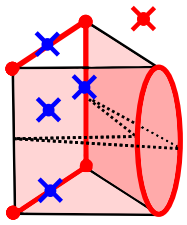

singularity			
$\Gamma:\ 6\to 12$	$R:\ 2\to 2$	$\Delta:\ 3\to 6$	
$A:\ 6\to 12$	$\Sigma:\ 2\to 2$	$P:\ 3\to 6$	
$L:\ 2\to 4$	$(u,u,w):\ 1\to 2$		
$M:\ 2\to 4$	$(1/2,v,w):\ 1\to 2$		

index theorem	
$\chi(\mathcal{O})=1$	
$=(+1)\times 4$	$\cdots$at point
$+(-1)\times 3$	$\cdots$on line
$+(-1)$	$\cdots$on plane
$+(+1)$	$\cdots$general point

Figure 8.22: Space group no. 149 (D_3^1).

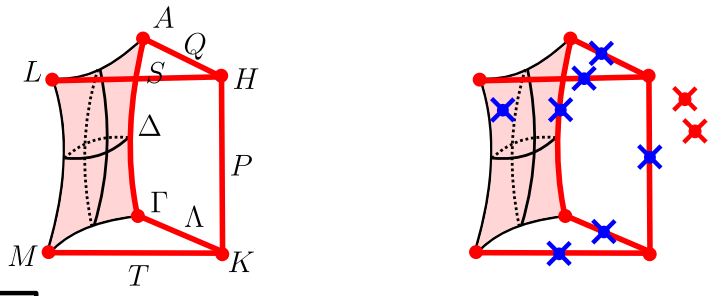

singularity

$\Gamma: 6 \to 12$	$\Lambda: 2 \to 2$	$P: 3 \to 3$
$A: 6 \to 12$	$Q: 2 \to 2$	$S: 2 \to 2$
$M: 2 \to 4$	$\Delta: 3 \to 6$	$T: 2 \to 2$
$L: 2 \to 4$		
$H: 6 \to 6$	$(u, 0, w): 1 \to 2$	
$K: 6 \to 6$		

index theorem

$$\begin{aligned}\chi(\mathcal{O}) &= 1 \\ &= (+1) \times 6 && \cdots \text{at point} \\ &\quad + (-1) \times 6 && \cdots \text{on line} \\ &\quad + (-1) && \cdots \text{on plane} \\ &\quad + (+1) \times 2 && \cdots \text{general point}\end{aligned}$$

Figure 8.23: Space group no. 150 (D_3^2).

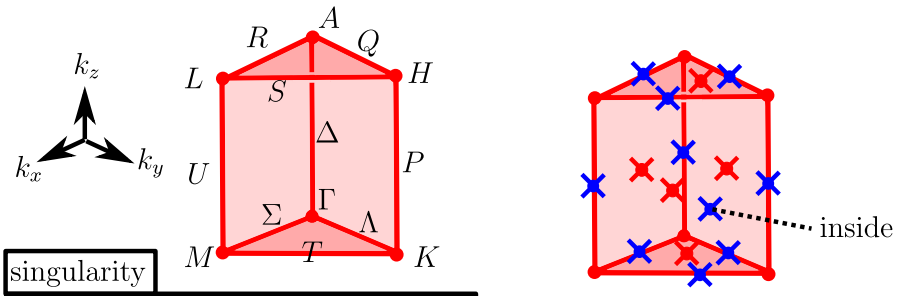

singularity

$\Gamma: 12 \to 24$	$U: 2 \to 4$	$P: 3 \to 6$
$A: 12 \to 24$	$R: 2 \to 4$	$\Delta: 6 \to 12$
$L: 4 \to 8$	$\Sigma: 2 \to 4$	$S: 2 \to 4$
$M: 4 \to 8$	$\Lambda: 2 \to 4$	$T: 2 \to 4$
$H: 6 \to 12$	$Q: 2 \to 4$	
$K: 6 \to 12$	$(1/2, v, w): 1 \to 2$	
$(u, 0, w): 1 \to 2$	$(u, u, w): 1 \to 2$	
$(u, v, 0\&1/2): 1 \to 2$		

index theorem

$$\begin{aligned}\chi(\mathcal{O}) &= 1 \\ &= (+1) \times 6 && \cdots \text{at point} \\ &\quad + (-1) \times 9 && \cdots \text{on line} \\ &\quad + (+1) \times 5 && \cdots \text{on plane} \\ &\quad + (-1) && \cdots \text{general point}\end{aligned}$$

Figure 8.24: Space group no. 177 (D_6^1).

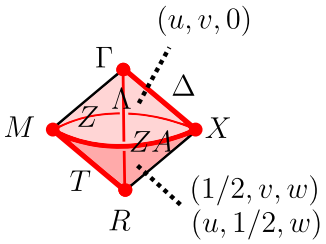

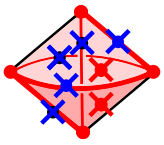

singularity	index theorem
$\Gamma:\ 12 \to 24$ $\Delta:\ 2 \to 4$ $\Lambda:\ 3 \to 3$	$\chi(\mathcal{O}) = 1$
$R:\ 12 \to 24$ $T:\ 2 \to 4$	$= (+1) \times 4$ ⋯ at point
$M:\ 4 \to 8$ $Z:\ 2 \to 4$	$+ (-1) \times 5$ ⋯ on line
$X:\ 4 \to 8$ $ZA:\ 2 \to 4$	$+ (+1) \times 2$ ⋯ on plane
$(u, v, 0):\ 1 \to 2$ $(1/2, v, w):\ 1 \to 2$	$+ 0$ ⋯ general point
$(u, 1/2, w):\ 1 \to 2$	

Figure 8.25: Space group no. 195 (T^1).

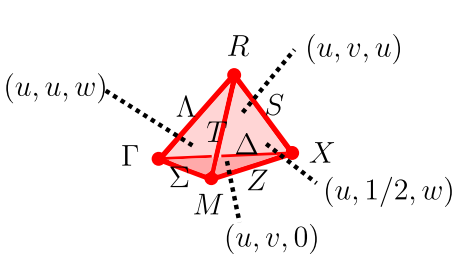

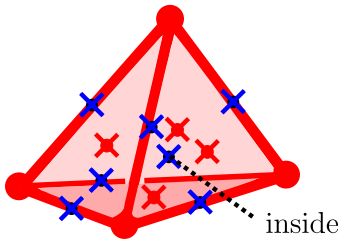

singularity	index theorem
$\Gamma:\ 24 \to 48$ $Z:\ 2 \to 4$ $\Lambda:\ 3 \to 6$	$\chi(\mathcal{O}) = 1$
$R:\ 24 \to 48$ $S:\ 2 \to 4$ $\Delta:\ 4 \to 8$	$= (+1) \times 4$ ⋯ at point
$M:\ 8 \to 16$ $\Sigma:\ 2 \to 4$ $T:\ 4 \to 8$	$+ (-1) \times 6$ ⋯ on line
$X:\ 8 \to 16$	$+ (+1) \times 4$ ⋯ on plane
$(u, v, 0):\ 1 \to 2$ $(u, 1/2, w):\ 1 \to 2$	$+ (-1)$ ⋯ general point
$(u, u, w):\ 1 \to 2$ $(u, v, u):\ 1 \to 2$	

Figure 8.26: Space group no. 207 (O^1).

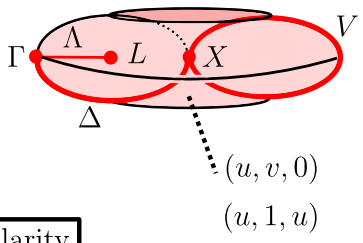

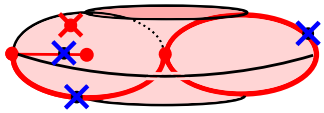

singularity			
Γ :	$12 \to 24$	Λ :	$3 \to 3$
L :	$3 \to 6$	Δ :	$2 \to 4$
X :	$4 \to 8$	V :	$2 \to 4$
$(u, v, 0)$:	$1 \to 2$		
$(u, 1, u)$:	$1 \to 2$		

index theorem		
$\chi(\mathcal{O})$	$=1$	
	$=(+1) \times 3$	$\cdots$at point
	$+(-1) \times 3$	$\cdots$on line
	$+(+1)$	$\cdots$on plane
	$+0$	$\cdots$general point

Figure 8.27: Space group no. 196 (T^2).

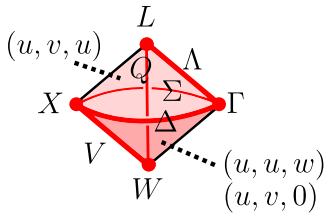

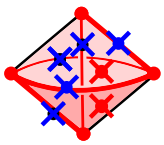

singularity					
Γ :	$24 \to 48$	V :	$2 \to 4$	Λ :	$3 \to 6$
L :	$6 \to 12$	Q :	$2 \to 2$	Δ :	$4 \to 8$
X :	$8 \to 16$	Σ :	$2 \to 4$		
W :	$4 \to 8$	(u, u, w) :	$1 \to 2$		
		(u, v, u) :	$1 \to 2$		
		$(u, v, 0)$:	$1 \to 2$		

index theorem		
$\chi(\mathcal{O})$	$=1$	
	$=(+1) \times 4$	$\cdots$at point
	$+(-1) \times 5$	$\cdots$on line
	$+(+1) \times 2$	$\cdots$on plane
	$+0$	$\cdots$general point

Figure 8.28: Space group no. 209 (O^3).

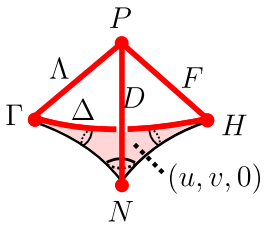

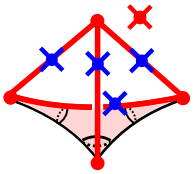

singularity			
Γ :	$12 \to 24$	D :	$2 \to 2$
H :	$12 \to 24$	Δ :	$2 \to 4$
N :	$2 \to 4$	Λ :	$3 \to 3$
P :	$12 \to 12$	F :	$3 \to 3$
$(u, v, 0)$:	$1 \to 2$		

index theorem		
$\chi(\mathcal{O})$	$=1$	
	$=(+1) \times 4$	$\cdots$ at point
	$+(-1) \times 4$	$\cdots$ on line
	$+0$	$\cdots$ on plane
	$+(+1)$	$\cdots$ general point

Figure 8.29: Space group no. 197 (T^3).

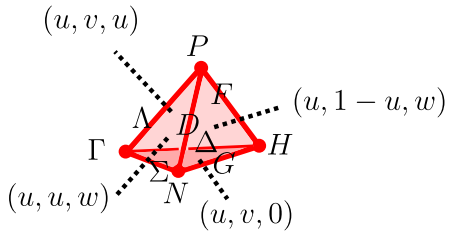

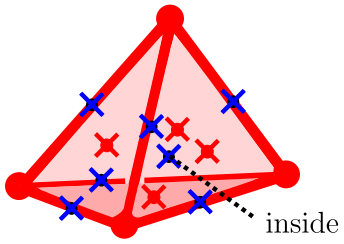

singularity					
Γ :	$24 \to 48$	G :	$2 \to 4$	Λ :	$3 \to 6$
H :	$24 \to 48$	Σ :	$2 \to 4$	Δ :	$4 \to 8$
N :	$4 \to 8$	D :	$2 \to 4$	F :	$3 \to 6$
P :	$12 \to 24$	$(u, 1-u, w)$:	$1 \to 2$		
$(u, v, 0)$:	$1 \to 2$	(u, v, u) :	$1 \to 2$		
(u, u, w) :	$1 \to 2$				

index theorem		
$\chi(\mathcal{O})$	$=1$	
	$=(+1) \times 4$	$\cdots$ at point
	$+(-1) \times 6$	$\cdots$ on line
	$+(+1) \times 4$	$\cdots$ on plane
	$+(-1)$	$\cdots$ general point

Figure 8.30: Space group no. 211 (O^5).

8.6 Rough condition and nontrivial space groups

As we discussed, the topology of the momentum space orbifold imposes strong constraints on spin textures in momentum space. Generally, we should consider such constraints carefully to decide whether the space group should always be interesting or not. However, we can state that the space groups No. 197 and 211 should always be "nontrivial" (at least in our purpose) with rough argument shown below. If there are no high-winding-number structures around the special points and no spin monopoles except for the special points, we here call it trivial.

Let us consider the Poincaré-Hopf index theorem for three-dimensional Brillouin zone (three-dimensional torus) of the space group No.197. In the case of No. 197, the numbers of elements of stars[6] for Γ, H, P, and N are $24/24 = 1$, $24/24 = 1$, $24/12 = 2$, and $24/4 = 6$, respectively. For each point, the winding numbers of the elements of the star take the same value because proper rotations do not change the winding number of spin monopoles.

Suppose that there is no spin monopole except for the special points Γ, H, P, and N. According to the Poincaré-Hopf index theorem, the following relation holds:

$$Q_\Gamma + Q_H + 2Q_P + 6Q_N = 0, \tag{8.17}$$

where Q_i ($i = \Gamma, H, P$, and N) are the winding numbers around special points. There is no $(Q_\Gamma, Q_H, Q_P, Q_N)$ satisfying that $|Q_i| = 1$ for all $i = \Gamma, H, P$, and N. Thus, there should be high-winding-number spin monopoles around the special points or spin monopoles except for the special points. For instance, $(Q_\Gamma, Q_H, Q_P, Q_N) = (-5, 1, -1, 1)$ satisfies the orbifold constraints in Fig. 8.29. Of course, this set also satisfies the weaker condition (8.17). The similar argument can be applied to the space group No. 211. $Bi_{12}GeO_{20}$ and Hg_4Pt are examples of materials labeled by No. 197 and No. 211, respectively.

Conditions such as Eq. (8.17) are weaker than those discussed in the previous sections. In the simple two-dimensional case, however, such conditions are the same as the conditions obtained by considering the topology of orbifolds. Let us again consider the magnon spin-momentum locking in the kagome lattice antiferromagnet. The momentum space orbifold is the orbifold $S333$ with three order-3 singular points Γ, K, and K', which is homeomorphic with the two-sphere. Thus, the generalized Poincaré-Hopf index theorem for this orbifold is given by

$$2 = +1 \times 3 + (-1). \tag{8.18}$$

[6] In the band theory, a star is defined as the set of points related each other by the symmetry operations.

Thus, there should be spin vortex with $Q = 1 + 3 \times (-1) = -2$ spin vortex around one singular point or a spin vortex with $Q = -1$ at a general point[7]. This conclusion can also be obtained by the Poincaré-Hopf index theorem for the Brillouin zone itself.

In the case of three-dimensional space groups, however, the singular structures are much more complicated as shown in the previous chapters. The singular points are closely related each other via the singular lines and planes. In such a situation, the Poincaré-Hopf index theorem for the Brillouin zone itself lacks the information of the connectivity between the singular points, and we should consider the topology of the orbifold to obtain the complete conditions for spin textures in momentum space.

8.7 Summary and future works

We classify the spin texture in momentum space under the three-dimensional space group and time-reversal symmetries. We define the momentum space orbifold and consider spin vector fields on it. When we focus on specific 24 space groups under the time-reversal symmetry, we find that the problem of spin textures in momentum space can be mapped to that of vector fields on the momentum space orbifold. By applying the generalized Poincaré-Hopf index theorem, which relates the topology of the singular space with a vector field on it, we express the spin textures in momentum space as the orbifold pictures. We also find that there should be high-winding number spin monopoles or the Weyl point at a point with low symmetry in the case of space groups No. 197 and 211. In the following, we list interesting future works related to the momentum space orbifold.

Spin texture in momentum space

- Exploring high-winding number spin monopoles in the above framework.
- Exploring Weyl semimetals in the above framework.
- The spin texture problem under improper rotations.
- The spin texture problem under nonsymmorphic operations.

[7]In terms of orbifolds, we can easily understand the stability of the magnon spin texture in real materials. We should generate Weyl points with the winding number -1 to get rid of the -2 spin vortex.

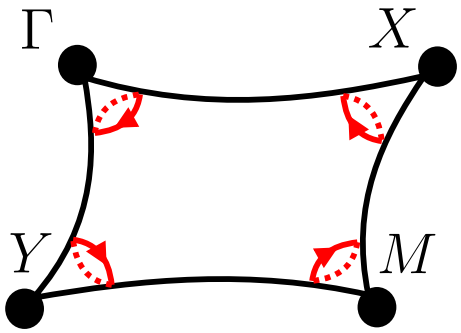

Figure 8.31: Loops on the orbifold $\mathbb{T}^2/C_2$.

Orbifold and topological classification

- Considering the Berry curvature on the momentum space orbifold.
- Understanding the topological classification in terms of the orbifold.

Before ending this thesis, we give an idea to deal with the topological classification in terms of the orbifold. In the field of the topological classification, topological invariants are defined by the momentum integral of the momentum-dependent quantity. Thus, it is difficult to judge whether a given material is topological or not at first sight. However, topological invariants can be calculated by the information at the specific points for some cases [98, 99, 100]. Ref. [98] has shown that the $\mathbb{Z}_2$ invariant for a topological insulator with the inversion symmetry is given by the product of the parity eigenvalues of occupied bands at the time-reversal (or equivalently, inversion) symmetric points. Since the mathematics of the Chern number is simpler than that of the $\mathbb{Z}_2$ invariant, we here try to reinterpret a formula for the Chern number under the two-fold rotational symmetry.

According to Ref. [100], the Chern number of a two-dimensional system with rotational symmetry can be determined modulo some integer by using the information of rotation eigenvalues at rotational symmetric points. For the two-fold rotational symmetry, the formula is given by

$$(-1)^C = \prod_{i \in occupied} \zeta_i(\Gamma)\zeta_i(X)\zeta_i(Y)\zeta_i(M), \tag{8.19}$$

where C is the Chern number, Γ, X, Y, and M are the rotational symmetric points, i denote the occupied bands, and ζ_i are the two-fold rotation eigenvalues at symmetric points. This formula enables us to judge whether the Chern number is even or odd.

The momentum space orbifold for the two-fold rotational symmetry is given by $\mathbb{T}^2/C_2$ [Fig.8.31]. On the orbifold, the identification of wave functions is introduced as

$$|\boldsymbol{k}, \alpha\rangle \sim \hat{C}_2 |\boldsymbol{k}, \alpha\rangle. \tag{8.20}$$

Since the non-Abelian Berry connection

$$[\hat{\boldsymbol{A}}_{\boldsymbol{k}}]_{\alpha\beta} \equiv -i\langle \boldsymbol{k}, \alpha | \nabla_{\boldsymbol{k}} | \boldsymbol{k}, \beta \rangle \tag{8.21}$$

behaves as a usual vector under the space group symmetry, the Berry connection is a single-valued function on the orbifold. Let us consider the Berry phase around the loop L on the orbifold, which is given by the determinant of the Wilson loop [100]

$$\det P \exp\left[i \oint_L \hat{\boldsymbol{A}}_{\boldsymbol{k}} \cdot d\boldsymbol{k} \right], \tag{8.22}$$

where P means the path ordering. If we take the infinitesimally small loops around the symmetric points $\boldsymbol{k}_{inv} = \Gamma, X, Y$, and M, the Berry phase is given by

$$\det P \exp\left[i \oint_L \hat{\boldsymbol{A}}_{\boldsymbol{k}} \cdot d\boldsymbol{k} \right] = \prod_{i \in occupied} \langle \boldsymbol{k}_{inv}, i | \hat{C}_2 | \boldsymbol{k}_{inv}, i \rangle = \prod_{i \in occupied} \zeta_i(\boldsymbol{k}_{inv}). \tag{8.23}$$

The product of the Berry phases around $\boldsymbol{k}_{inv} = \Gamma, X, Y$, and M corresponds to the flux going through the orbifold, which is a half of total flux going through the Brillouin zone. The phase for the flux is given by

$$\exp\left[i \frac{2\pi C}{2} \right] = (-1)^C. \tag{8.24}$$

Using Eqs. (8.23) and (8.24), we obtain the formula (8.19)

The above rough discussion implies that the topological classification problem can be understood in terms of the singular structure of the momentum space orbifold. As discussed in the last part of Chap. 5, the topological classification problem under the space group symmetries has not been solved completely. We expect that the notion of the momentum space orbifold would solve it and give an intuitive description of topological physics under the space group symmetries.

Summary

In this thesis, we have investigated momentum-dependent spin of magnons and electrons, both of which are important (quasi-)particles in recent spintronics and topological physics. We have generalized the notion of spin-momentum locking to the magnonic systems by defining magnon spin for one-magnon states in ordered magnets. We have found that the magnon spin-momentum locking occurs even when the Hamiltonian has spin-rotational symmetries. The key idea is that ground and one-magnon states completely break the spin rotational symmetry in the magnon spin-momentum locking. We have considered kagome lattice antiferromagnets with 120° structure, where $U(1)$ symmetry breaking occurs, and plotted the magnon spin texture in momentum space. We have found a spin texture with the winding number -2, which has not been found in realistic electron models. The plot of the magnon spin texture obtained in this calculation has motivated another interesting direction of the study of spin-momentum locking: the relationship between the spin texture and topology of momentum space. In the presence of time-reversal and space group symmetries, the information of the band theory is included in the small part of the Brillouin zone. We have introduced the notion of the orbifold in order to describe this part in terms of the topology and named it as the momentum space orbifold. By applying the Poincaré-Hopf index theorem for the momentum space orbifold, we have given constraints on the momentum space spin textures of the three-dimensional electron systems under time-reversal and specific space group symmetries. These constraints would be useful to find Weyl points and new spin monopoles with higher winding numbers in momentum space.

Acknowledgements

First I would like to thank my supervisor Masao Ogata for his continuing support and fruitful scientific discussions. I would like to thank the referees of this thesis, Prof. Hosho Katsura, Prof. Shinji Tsuneyuki, Prof. Hidenori Takagi, Prof Yoshichika Otani, and Prof. Shuichi Murakami.

I am grateful to research collaborators, Prof. Kentaro Nomura (Ref. [1]), Massoud Ramezani Masir (Ref. [2]), Prof. Allan H. MacDonald (Ref. [2]), and Prof. Masahito Ueda (the latter part of this thesis), for fruitful discussions. I am grateful to Tomonari Mizoguchi, Yusuke Kousaka, Hiroyasu Matsuura, Jun'ichi Ieda, and Shinichi Shamoto for fruitful discussions about magnon spin-momentum locking. I am grateful to Prof. Toshitake Kohno, Prof. Yasuhiro Hatsugai, Toshikaze Kariyado, and Ikuma Tateishi for fruitful discussions about mathematics and physics of orbifolds. I would like to appreciate all colleagues of Ogata group for everyday conversations, scientific discussions, and supports.

I am supported by the Japan Society for the Promotion of Science (JSPS) KAKENHI (Grant No. 16J07110). I am also supported through Program for Leading Graduate Schools (MERIT). I would like to thank the assistant supervisor Masatoshi Imada and Prof. Yohei Yamaji for discussions and advices in the MERIT program. Finally, I thank my family and friends for their great supports and encouragements.

Publication list

1. Nobuyuki Okuma,
"*Magnon Spin-Momentum Locking: Various Spin Vortices and Dirac magnons in Noncollinear Antiferromagnets*",
Phys. Rev. Lett. **119**, 107205 (2017).

2. Nobuyuki Okuma, Massoud Ramezani Masir, and Allan H. MacDonald,
"*Theory of the spin-Seebeck effect at a topological-insulator/ferromagnetic-insulator interface*",
Phys. Rev. B **95**, 165418 (2017).

3. Nobuyuki Okuma and Kentaro Nomura,
"*Microscopic derivation of magnon spin current in topological insulator/ferromagnet heterostructure*",
Phys. Rev. B **95**, 115403 (2017).

4. Nobuyuki Okuma and Masao Ogata,
"*Unconventional Spin Hall Effect and Axial Current Generation in a Dirac Semimetal*",
Phys. Rev. B **93**, 140205(R) (2016).

5. Nobuyuki Okuma and Masao Ogata,
"*Long-range Coulomb interaction effects on the surface Dirac electron system of a three-dimensional topological insulator*",
J. Phys. Soc. Jpn. **84**, 034710 (2015).

6. Nobuyuki Okuma and Masao Ogata,
"*Study of spin transport in Dirac systems*"
J. Phys. Conf. Ser. **603**, 012018 (2015).

Bibliography

[1] N. Okuma and K. Nomura, Phys. Rev. B **95**, 115403 (2017).

[2] N. Okuma, M. R. Masir, and A. H. MacDonald, Phys. Rev. B **95**, 115403 (2017).

[3] N. Okuma, Phys. Rev. Lett. **119**, 107205 (2017).

[4] S. Murakami, N. Nagaosa and S.C. Zhang, Science **301**,1348 (2003).

[5] M. Z. Hasan and C. L. Kane, Rev. Mod. Phys. **82**, 3045 (2010).

[6] X.-L. Qi and S.-C. Zhang, Rev. Mod. Phys. **83**, 1057 (2011).

[7] D. Xiao, M.-C. Chang, and Q. Niu, Rev. Mod. Phys. **82**, 1959 (2010).

[8] S. Murakami, New J. Phys. **9**, 356 (2017).

[9] A. A. Burkov and L. Balents, Phys. Rev. Lett. **107**, 127205 (2011).

[10] B. Q. Lv *et al.*, Phys. Rev. X **5**, 031013 (2015)

[11] Su-Yang Xu *et al.*, Science **349**, 613 (2015).

[12] M. Hoesch, M .Muntwiler, V. N. Petrov, M. Hengsberger, L. Patthey, M. Shi, M. Falub, T. Greber, and J. Osterwalder, Phys. Rev. B **69**, 241401(R) (2004).

[13] H. Zhang *et al.*, Nat. Phys. **5**, 438 (2009).

[14] H. B. Nielsen and M. Ninomiya, Nucl. Phys. B **185**, 1 (1981) .

[15] H. B. Nielsen and M. Ninomiya, Nucl. Phys. B **193**, 173 (1981) .

[16] V.M. Edelstein, Solid State Commun. **73**, 233 (1990).

[17] A. R. Mellnik, J. S. Lee, A. Richardella, J. L. Grab, P. J. Mintun, M. H. Fischer, A. Vaezi, A. Manchon, E.-A. Kim, N. Samarth, and D. C. Ralph, Nature **511**, 449 (2014).

[18] Y. Wang, P. Deorani, K. Banerjee, N. Koirala, M. Brahlek, S. Oh, and H. Yang, Phys. Rev. Lett. **114**, 257202 (2015).

[19] Y. Fan, P. Upadhyaya, X. Kou, M. Lang, S. Takei, Z. Wang, J. Tang, L. He, L.-T. Chang, M. Montazeri, G. Yu, W. Jiang, T. Nie, R. N. Schwartz, Y. Tserkovnyak, and K. L. Wang, Nature Mater. **13**, 699 (2014).

[20] Cui-Zu Chang, *et al.*, Science **340**, 167 (2013).

[21] E. Fradkin, *Field Theories of Condensed Matter Systems* (Cambridge University Press, Cambridge, UK, 2013).

[22] Y. Shiomi, K. Nomura, Y. Kajiwara, K. Eto, M. Novak, Kouji Segawa, Yoichi Ando, and E. Saitoh, Phys. Rev. Lett. **113**, 196601 (2014).

[23] K. Kondou, R. Yoshimi, A. Tsukazaki, Y. Fukuma, J. Matsuno, K. S. Takahashi, M. Kawasaki, Y. Tokura, and Y. Otani, Nature physics **12**, 1027 (2016).

[24] Z. Jiang, C. Z. Chang, M. Ramezani Masir, C. Tang, Y. Xu, J. S. Moodera, A. H. MacDonald, and J. Shi, Nat. Commun. **7**, 11458 (2016).

[25] S. Takei and Y. Tserkovnyak, Phys. Rev. Lett. **112**, 227201 (2014).

[26] S. Takahashi, E. Saitoh, and S. Maekawa, J. Phys. Conf. Ser. **200**, 062030 (2010).

[27] D. W. Snoke, *Solid State Physics* : *Essential Concepts* (Pearson/Addison-Wesley, San Francisco, 2009).

[28] A. V. Chumak, V. I. Vasyuchka, A. A. Serga, and B. Hillebrands, Nature Phys. **11**, 453 (2015).

[29] K. Uchida, H. Adachi, T. Ota, H. Nakayama, S. Maekawa, and E. Saitoh, Appl. Phys. Lett. **97**, 172505 (2010).

[30] Y. Ohnuma, H. Adachi, E. Saitoh, and S. Maekawa, Phys. Rev. B **87**, 014423 (2013).

[31] R. Cheng, M. W. Daniels, J.-G. Zhu, and D. Xiao, Sci. Rep. **6**, 24223 (2016).

[32] S. Fujimoto, Phys.Rev.Lett. **103**, 047203 (2009).

[33] H. Katsura, N. Nagaosa, and P. A. Lee, Phys.Rev.Lett. **104**, 066403 (2010).

[34] Y. Onose, T. Ideue, H. Katsura, Y. Shiomi, N. Nagaosa, and Y. Tokura, Science **329**, 297 (2010).

[35] S. A. Owerre, J. Phys.: Condens. Matter **29**, 03LT01 (2017).

[36] R. Shindou, R. Matsumoto, S. Murakami, and J. I. Ohe, Phys. Rev. B **87**, 174427 (2013).

[37] L. Zhang, J. Ren, J. -S. Wang, and B. Li, Phys. Rev. B **87**, 144101 (2013).

[38] R. Chisnell, J. S. Helton, D. E. Freedman, D. K. Singh, R. I. Bewley, D. G. Nocera, and Y. S. Lee, Phys. Rev. Lett. **115**, 147201 (2015).

[39] S. A. Owerre, Journal of Applied Physics **120**, 043903 (2016).

[40] F. Y. Li, Y. D. Li, Y. B. Kim, L. Balents, Y. Yu, and G. Chen, Nature Commun. **7**, 12691 (2016).

[41] J. Fransson, A. M. Black-Schaffer, and A. V. Balatsky, Phys. Rev. B **94**, 075401 (2016).

[42] A. Mook, J. Henk, and I. Mertig, Phys. Rev. B **95**, 014418 (2017).

[43] R. Cheng, S. Okamoto, and D. Xiao, Phys. Rev. Lett. **117**, 217202 (2016).

[44] V. A. Zyuzin and A. A. Kovalev, Phys. Rev. Lett. **117**, 217203 (2016).

[45] C. Kittel, *Introduction to Solid State Physics* (John Wiley & Sons, New York, 1986).

[46] P. Fazekas, *Lecture Notes on Electron Correlation and Magnetism* (World Scientific, Singapore,1999).

[47] A. Altland and B. Simons, *Condensed matter field theory* (Cambridge University Press, 2006).

[48] H. Watanabe and H. Murayama, Phys. Rev. Lett. **108**, 251602 (2012).

[49] Y. Hidaka, Phys. Rev. Lett. **110**, 091601 (2013).

[50] M. Mochizuki, Phys. Rev. Lett. **108**, 017601 (2012).

[51] H. Adachi, K. Uchida, E. Saitoh, and S. Maekawa, Rep. Prog. Phys. **76**, 036501 (2013).

[52] L. J. Cornelissen, K. J. H. Peters, G. E. W. Bauer, R. A. Duine, and B. J. van Wees, Phys. Rev. B **94**, 014412 (2016).

[53] K. Uchida, S. Takahashi, K. Harii, J. Ieda, W. Koshibae, K. Ando, S. Maekawa, and E. Saitoh, Nature **455**, 778 (2008).

[54] V. V. Kruglyak, S. O. Demokritov, and D. Grundler, J. Phys. D **43**, 264001 (2010).

[55] A. L. Chernyshev and P. A. Maksimov, Phys. Rev. Lett. **117**,187203 (2016).

[56] A. D. Maestro and M. Gingras, J. Phys. Cond. Matt. **16**, 3399 (2004).

[57] J. H. P. Colpa, Physica A **93**, 327 (1978).

[58] S. A. Owerre, Phys. Rev. B **95**, 014422 (2017).

[59] D. Grohol, K. Matan, J.-H Cho, S.-H. Lee, J. W. Lynn, D. G. Nocera and Y. S. Lee, Nat. Mater. **4**, 323 (2005).

[60] K. Matan, D. Grohol, D. G. Nocera, T. Yildirim, A. B. Harris, S. H. Lee, S. E. Nagler, and Y. S. Lee, Phys. Rev. Lett. **96**, 247201 (2006).

[61] T. Chatterji, *Neutron Scattering from Magnetic Materials* (Elsevier, Amsterdam, 2006).

[62] G. L. Squires, *Introduction to the Theory of Thermal Neutron Scattering* (Cambridge University Press: Cambridge, UK, 1978).

[63] V. Guillemin and A. Pollack, *Differential topology* (American Mathematical Society, 2010).

[64] M. Nakahara, *Geometry, Topology, and Physics* (A. Hilger, 1990).

[65] E. Witten, arXiv:1508.04715.

[66] E. Witten, arXiv:1510.07698.

[67] A. Hattori, *Topology of manifold* (Iwanami shoten, Tokyo, 2003).

[68] T. Inui, Y. Tanabe, and Y. Onodera, *Group Theory and Its Applications in Physics* (Springer, Berlin, 1990).

[69] C. J. Bradley and A. P. Cracknell, *The Mathematical Theory of Symmetry in Solids : Representation Theory for Point Groups and Space Groups* (Oxford University Press, 1972).

[70] D. J. Thouless, M. Kohmoto, M. P. Nightingale, and M. den Nijs, Phys. Rev. Lett. **49**, 405 (1982).

[71] M. Kohmoto, Ann. Phys.**160**, 343 (1985).

[72] K. V. Klitzing, G. Dorda, and M. Pepper, Phys. Rev. Lett. **45**, 494 (1980).

[73] Y. Hatsugai, Phys. Rev. Lett. **71**, 3697 (1993).

[74] F. D. M. Haldane, Phys. Rev. Lett. **61**, 2015 (1988).

[75] A. Kitaev, AIP Conf. Proc. **1134**, 22 (2009).

[76] A. Altland and M. R. Zirnbauer, Phys. Rev. B **55**, 1142 (1997).

[77] S. Ryu, A. P. Schnyder, A. Furusaki, and A. W. W. Ludwig, New J. Phys. **12**, 065010 (2010).

[78] C. L. Kane and E. J. Mele, Phys. Rev. Lett. **95**, 226801 (2005).

[79] L. Fu, C. L. Kane, and E. J. Mele, Phys. Rev. Lett. 98, 106803 (2007).

[80] L. Fu, Phys. Rev. Lett. **106**, 106802 (2011).

[81] Y. Ueno, A. Yamakage, Y. Tanaka, and M. Sato, Phys. Rev. Lett. **111**, 087002 (2013).

[82] K. Shiozaki and M. Sato, Phys. Rev. B **90**, 165114 (2014).

[83] J. C. Y. Teo, L. Fu, and C. L. Kane, Phys. Rev. B **78**, 045426 (2008).

[84] K. Shiozaki, M. Sato, and K. Gomi, Phys. Rev. B **91**, 155120 (2015).

[85] K. Shiozaki, M. Sato, and K. Gomi, Phys. Rev. B **93**, 195413 (2016).

[86] T. Morimoto and A. Furusaki, Phys. Rev. B **88**, 125129 (2013).

[87] H. C. Po, A. Vishwanath, and H. Watanabe, Nat. Commun. **8**, 50 (2017).

[88] B. Bradlyn, L. Elcoro, J. Cano, M. G. Vergniory, Z. Wang, C. Felser, M. I. Aroyo, and B. A. Bernevig, Nature **547**, 298 (2017).

[89] T. Kohno, *Crystallographic Groups* (Kyouritu shuppan, Tokyo, 2015).

[90] W. P. Thurston, *Geometry and Topology of Three-Manifolds* (Princeton lecture notes, 1979).

[91] J. H. Conway, O. Delgado Friedrichs, D. H. Huson, and W. P. Thurston, *On three-dimensional orbifolds and space groups*, Contributions to Algebra and Geometry, **42** (2), 475 (2001).

[92] S. Weinberg, *The Quantum Theory of Fields* (Cambridge University Press, 2000).

[93] A. Alexandradinata, C. Fang, M. J. Gilbert, and B. A. Bernevig, Phys. Rev. Lett. **113**, 116403 (2014).

[94] J. P. Brasselet, J. Seade , T. Suwa, *Vector fields on singular varieties*, (Lecture Notes in Math. , Vol. 1987, Springer-Verlag, Berlin, 2009).

[95] M. I. Aroyo, J. M. Perez-Mato, D. Orobengoa, E. Tasci, G. de la Flor, and A. Kirov, Bulg. Chem. Commun. **43(2)**, 183-197 (2011).

[96] M. I. Aroyo, J. M. Perez-Mato, C. Capillas, E. Kroumova, S. Ivantchev, G. Madariaga, A. Kirov and H. Wondratschek, Z. Krist. **221**, 1, 15-27 (2006).

[97] M. I. Aroyo, A. Kirov, C. Capillas, J. M. Perez-Mato and H. Wondratschek, Acta Cryst. ***A*62**, 115-128 (2006).

[98] L. Fu and C. L. Kane, Phys. Rev. B **76**, 045302 (2007).

[99] A. M. Turner, Y. Zhang, R. S. K. Mong, and A. Vishwanath, Phys. Rev. B **85**, 165120 (2012).

[100] C. Fang, M. J. Gilbert, and B. A. Bernevig, Phys. Rev. B **86**, 115112 (2012).